DYNAMICS OF MIXED BINARY MERGERS USING NUMERICAL RELATIVITY SIMULATIONS

A Dissertation
Presented to
The Academic Faculty

By

Bhavesh Khamesra

In Partial Fulfillment
of the Requirements for the Degree
Doctor of Philosophy in the
School of Physics

Georgia Institute of Technology

May 2021

DYNAMICS OF MIXED BINARY MERGERS USING NUMERICAL RELATIVITY SIMULATIONS

Thesis Committee:

Prof. David Ballantyne
Department of Physics
Georgia Institute of Technology

Prof. Laura Cadonati
Department of Physics
Georgia Institute of Technology

Prof. Deirdre Shoemaker
Department of Physics
The University of Texas at Austin

Prof. Pablo Laguna
Department of Physics
The University of Texas at Austin

Prof. John Wise
Department of Physics
Georgia Institute of Technology

Date approved: April 23, 2021

The black holes of nature are the most perfect macroscopic objects there are in the universe: the only elements in their construction are our concepts of space and time

- Subrahmanyan Chandrasekhar

Dedicated to My Family,
for always believing in me.

In loving memory of
My Grandparents and My Ba.

ACKNOWLEDGEMENTS

Ph.D. is a dream of many people and a few are fortunate to see it come true. Reaching closer to the finish line, I feel grateful and blessed to have amazing people in my life without whom this journey wouldn't be possible.

First and foremost, I want to thank my family members for their unconditional love and support, for always believing in me, encouraging me to follow my dreams, and for their immense hard work and sacrifices which allowed me to pursue this career.

I would like to express my sincere gratitude towards my advisor, my mentor and a good friend, Prof. Pablo Laguna for his immense support and guidance in the last six years. Even with the responsibilities as a chair of school of physics, Pablo's doors have always been open for his students. Be it discussing a new research problem or in need of life advice, it is always possible to rely on him. Pablo has always encouraged creative and independent thinking which provided me the necessary confidence to pursue new ideas, gave me the freedom to explore and innovate, and challenged me to push my boundaries. I have always admired his passion for research and his love for physics and will be forever grateful to take me as his student.

I would also like to thank my second advisor, Prof. Deirdre Shoemaker for her valuable guidance. Being in an extremely interactive and friendly research atmosphere, working at CRA felt like being part of a research family, a lot of which is thanks to Deirdre. From hosting great parties to making delicious vegan foods, from bringing her pets for students (especially me) to reminding Pablo our names, and for uncountable hours of helping me with research, I am immensely grateful to her. I also want to thank my undergraduate advisors and mentors Prof. Suneeta Vardarajan, Prof. Parmeswaran Ajith, Prof. Anil Gangal, Prof Jutta Kunz-Drolshagen and Prof. Prasad Subramanian without whose guidance and support, the journey to Georgia Tech wouldn't be possible.

I want to express my deep gratitude towards my committee members, Prof David Ballantyne, Prof. John Wise and Prof. Laura Cadonati for amazing courses and research interactions, helping me with various academic and research matters and for their invaluable time to review by proposal and thesis. I also want to thank Prof. Tamara Bogdanovic, Prof. Ignacio Taboda, Prof. Gongjie Li, Prof. A. Nepomuk Otte, and Dr. James Sowell. Special thanks to Miguel, Deborah, Chris, Kenny, Richard, Khai, Qiu, Bryan, Athanasios, Emily, Michael, Matt, Kate, Karan, Juan, Aycin, James, and Karelle for many memorable coffees, brainstorming sessions and research discussions, and numerous lunches, dinners, and game nights. I want to thank my collaborators and members of Einstein Toolkit and LIGO-VIRGO collaboration, in particular, Prof. Abhay Ashtekar, Dr. Roland Haas, Prof. Zachary Etienne, Dr. Erik Schnetter, Dr. James Healy, Prof. Steven Brandt and Prof. Helvi Witek. I also want to thank Pace and XSEDE team, and GT OIT team, especially Mehmet Belgin, John Wallom and Nguyen Nguyen for their constant help and support in the last five years.

Lastly, this journey would have been incomplete without acknowledging some special friends. I would like to thank my oldest friends Harshit, Anuresh, Chirayu, Akshit, Palash, Bhavya, and Rajan who I am fortunate to still have in my life. I want to thank my college group with whom I shared many travelling adventures including Aashay, Akash, Avani, Shivraj, Aditi, Haritej, Ankita, Neha, Punya, Ashok, Vikash, Deepika, Purvi, Sravani, Rohit, Iti, Dincy, Siddhartha, Poortata, Srivani, Abhijeet. I want to say special thanks to my partners in crime - Sudarshan, Shashank, Raj, Louis, Cheney, Yuxin, Danny, Alvin, Disha, Hemaa, Gayatri, Bahni, Jyoti, Prasoon, Agniva, Anish, Medha, Keertana, Swati, Melody, Zefie, Dayana, Rana, Chris, Adrien, Maryrose, Matt and Zack.

TABLE OF CONTENTS

LIST OF TABLES

LIST OF FIGURES

SUMMARY

Neutron star black hole (NSBH) mergers have captured the interest of physicists for more than 50 years. The study of these objects can provide valuable insights to understand the origins of heavy elements in the universe, the cause of short gamma ray bursts, the equation of state of neutron stars, and the quantum nature of gravity. However, they still remain the most elusive binary with no confirmed gravitational or electromagnetic detections to date. One of the primary challenges to identify an NSBH source is the high similarity in gravitational wave signatures of this system with a binary black hole and a double neutron star. Hence, we require the tools of numerical relativity to design accurate templates of gravitational waves and identify key features to differentiate between the signals of NSBH systems from other binaries. In this work, we perform relativistic hydrodynamical simulations of non-spinning neutron star black hole mergers using a new initial data method. Through an extensive comparison, we show the efficiency of our models with published works by analyzing the orbital dynamics, remnant properties, and gravitational wave signatures. We also investigate the differences between the coalescence of binary black holes and mixed binary systems as a function of initial conditions. Our results indicate that due to strong tidal disruption, low mass ratio and low compactness systems have the strongest deviation from the corresponding vacuum binary. Early disruption in these cases leads to the formation of an accretion disk and dynamical ejecta which impacts the post merger gravitational wave signal. A higher mass ratio or higher compactness system, on the other hand, barely faces any disruption leading to gravitational wave signals similar to a binary black hole. In such scenarios, any differences if exist, are found to be most prominent in higher order modes. Thus, in addition to model accuracy, the orientation of the signal would also play an important role in mixed binary detections.

CHAPTER 1

INTRODUCTION AND BACKGROUND

The emergence of gravitational wave (GW) astronomy has opened new channels to observe the universe. Since the first gravitational wave observation [1] by the Advanced Laser Interferometer Gravitational-Wave Observatories (LIGO) at Hanford and Livingston [2], the network of gravitational wave detectors has expanded to include advanced Virgo detector [3] and Kamioka Gravitational Wave detector (KAGRA) [4]. With multiple upgrades, their design sensitivities have been improved by more than 60% [5, 6] since the first observing runs which has led to confirmed detections of 50 compact binary systems [1, 7–18]. This success has massively boosted the interest of research community in gravitational wave research leading to additional proposed upgrades to the existing detectors (A+, AdV+), new planned detectors (LIGO-India), third generation observatories (Cosmic Explorer [19], Einstein Telescope [20]) and space based detectors (LISA [21]). The network of these observatories would allow us to observe gravitational waves over a larger bandwidth and higher accuracies, thus increasing our chances to find new sources and explore the hidden corners of the universe.

In addition to discovering new astrophysical objects, studies of gravitational wave signals can also provide deep insights about the population properties and formation channels of the source [22–26]. The detections of binary black hole (BBH) systems in O1, O2 and O3a observational runs place natural constraints on the lower and upper mass gap of black holes shedding light on their formation via pair instability supernova channel [27–29]. The estimated unequal masses of black holes in events GW190814 and GW190412,

and the evidence of spin misalignment in a fraction of O3a BBH events also suggest existence of alternate formation channels of the binary [25]. The detections of compact binaries can also be used to perform various precision tests on the theories of gravity [30–33], and measure the Hubble constant [34–36].

Along with 46 binary black holes and two double neutron star (DNS) detections, the third observing run also found at least two potential neutron star-black hole (NSBH) merger candidates [17, 18]. The longstanding absence of these objects in gravitational wave and electromagnetic observations has posed a new mystery in the astrophysics community and hence, the news of possible detections has brought in a lot of excitement. NSBH systems have fascinated physicists for the past several decades. The combination of extreme gravitational fields and ultradense states of matter at relativistic speeds makes them excellent laboratories to test the nature of gravity. Due to the possible lower mass gap in its components [14, 37–39] and differences in their mass distributions [40], such systems are expected to be on the higher end of mass ratios. Large imbalance in their component masses contributes to higher order multipole moments making these systems ideal candidates for the tests of the multipolar structure of gravity and no hair theorem [41–46]. Such tests would serve as strong evidence for or against alternate theories of gravity whose deviations from general relativity affect the higher order modes [47] or result in hairy black holes [48–52]. While most tests of general relativity using gravitational waves have been developed and performed with binary black holes, neutron star-black hole mergers can also provide novel testbeds to study the interactions between matter and gravity as predicted by alternate theories which would be absent in black hole binaries.

Gravitational wave signatures from mixed binary mergers can also help us to constrain the equation of state of the neutron star [53–55]. The central core of this star contains matter in ultradense states which cannot be probed through current experiments and hence, understanding the star equation of state can provide useful constraints on the theoretical

models of quantum states of matter which may exist at extreme densities [40]. Each equation of state model places a unique limit on the maximum mass of neutron star and hence, the equation of state information can also help to resolve the lower mass gap problem of stellar black holes. Numerical studies of mixed binary mergers have shown that in case of tidal disruption, the dynamics of the mixed binary can also be impacted by the equation of state model during the merger phase which leaves its imprint on the gravitational wave radiation [56–59]. In such scenarios, the amplitude of these waves can be greatly suppressed beyond a cut-off frequency for a stiff equation of state due to reduced variation in the quadrupole moment. However, for a soft equation of state, the coalescence can lead to a clean merger and ringdown signal in absence of tidal disruption. The cut-off frequency is then determined by the quasinormal frequency. Inferring the compactness from the gravitational wave cut-off frequency and masses from the inspiral part of the signal would allow us to determine the mass-radius relationship. Thus, in addition to tidal dephasing [54], cut-off frequencies can help us in constraining the equation of state [60, 61].

The disruption of a neutron star is also believed to be an ideal site for the nucleosynthesis of heavy elements. For systems with a low mass or highly spinning black hole, stellar disruption will likely generate neutron rich ejecta [62, 63] which can undergo rapid neutron capture process (r-process) [64–66] leading to the production of heavy elements. Unlike DNS, the electron fraction for NSBH is expected to be much lower ($Y_e \lesssim 0.1$) which will typically lead to a larger fraction of elements with mass number $A \gtrsim 120$ [67]. The radioactive decay of these nascent nuclei can result in a macronova or kilonova with transient electromagnetic signatures generated through alpha and beta decay and spontaneous fission processes [68, 69]. Highly magnetized accretion disks can also result in binding of poloidal field components with the black hole which can activate energy extraction from spinning black hole via Blandford-Znajek mechanism resulting in short gamma ray burst (sGRB) [70, 71]. Further, interactions of dynamical ejecta from disruption and accretion

process with interstellar media can lead to synchrotron emission [72]. The wide array of electromagnetic emissions would allow a multimessenger search of these systems which can provide extremely relevant data to investigate our current models of r-process nucleosynthesis, dynamical ejection, and study the velocity profiles of the ejecta [73, 74].

1.1. Evolution Dynamics

The evolution of a neutron star black hole binary begins in the inspiral phase during which it slowly dissipates energy and angular momentum via gravitational wave emission. The radiation reaction timescales in the early inspiral are much larger than its orbital period and hence, one can approximate a mixed binary as a system of two point particles in an adiabatic orbit. Under these approximations, post Newtonian theory provides a good description of the binary evolution [75]. From post-Newtonian calculations [76–78], the ratio of binary lifetime, T_{GW} and orbital period, T_{orb} is given by

$$\frac{T_{GW}}{T_{orb}} \approx 1.8 \left(\frac{r}{6M}\right)^{5/2} \left(\frac{M_{BH}}{6M_{\odot}}\right)^{-1} \left(\frac{M_{NS}}{1.4M_{\odot}}\right)^{-1} \left(\frac{M}{7.4M_{\odot}}\right)^{2} \tag{1.1}$$

Here, r is the orbital separation, M_{BH} is the mass of the black hole, M_{NS} is the mass of the neutron star, and $M = M_{BH} + M_{NS}$ is the total mass of the system. Quantities here are expressed in geometric units where $G = c = 1$. From equation 1.1, it can be seen that the orbital period becomes comparable to the lifetime of the binary as r approaches $6M$. At such close separations, adiabatic approximation does not hold well and finite size effects cannot be ignored. As a result, post-Newtonian model starts to fail in the late inspiral regime and one requires numerical relativity to employ the full general relativistic model.

During the late inspiral-merger phase, the constant battle between the tidal forces and star's self gravity decides the final fate of the binary. The merger of a black hole and a neutron star can fall under two scenarios [79] - first, the star gets disrupted outside the

innermost stable circular orbit (ISCO) before getting consumed by the black hole, and second the star suffers partial or no disruption after entering the ISCO and is completely swallowed by the hole. To differentiate between these two cases, Taniguchi et al. [80] analysed the quasiequilibrium states of non-spinning systems with polytropic stars and found a dependence of final state with initial configuration of the binary. By comparing the mass shedding frequency [1] with orbital frequency at ISCO, they obtained the following condition on critical mass ratio -

$$0.270\, C^{3/2} \sqrt{\frac{(1+q_c)^3}{q_c}} = 0.0680 \left[1 - \frac{0.444}{q_c^{1/4}} \left(1 - 3.54\, C^{1/3}\right)\right] \tag{1.2}$$

where, C is the compactness of the star which is defined as the ratio of mass and radius of the star, and q_c is the critical mass ratio of the system defined by the above relationship. Figure 1.1 shows the critical mass ratio as a function of compactness of the star which separates two regions of disruption. Systems with mass ratio, q $(= M_{BH}/M_{NS})$, greater than the critical value, q_c (shown by the orange color), barely suffer any disruption and are completely swallowed by the hole while systems with smaller mass ratios or low compactness of the star (region in the blue color) tend to be more likely to undergo disruption.

Things get more interesting with spinning binaries and realistic equation of state. Initial Newtonian and semi-relativistic studies investigated the tidal effects of a Kerr black hole on the structure of a fluid star [55, 81–83]. These studies mainly looked at the Euler equation in approximate relativistic models valid for systems with higher mass ratio ($q \gg 1$) and low compactness. Gravitational radiation reaction, self-gravity of star and its effects on orbital motion were ignored. The results showed strong dependence of the angular velocity of the star at ISCO on the spin of the black hole which in turn affects the tidal disruption condition. For maximally spinning black holes, the critical mass ratio was increased by a factor of 15. Similar analysis with soft and stiff equation of state models

[1] Frequency at which tidal forces are comparable to the self gravity of the star.

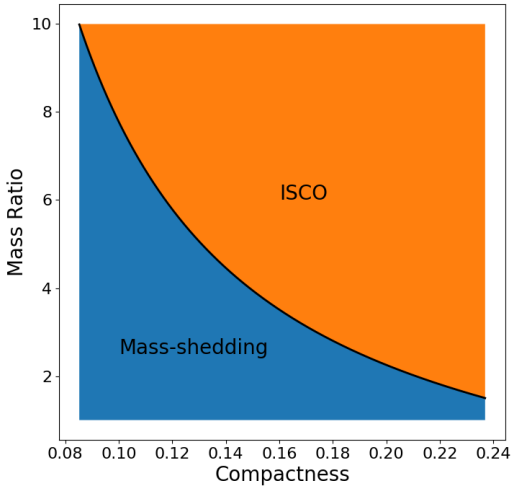

FIGURE 1.1: Critical curve based on the Newtonian relationship between mass ratio and compactness for non-spinning NSBH [78, 80]. Blue region denotes the initial conditions which would lead to mass shedding (and possible disruption) while orange region corresponds to non-disrupting cases.

showed the dependence of the maximum black hole mass inducing mass shedding on the equation of state models [83, 84].

Quasiequilibrium studies are thus the ideal tools to predict the effects of initial conditions on the final state of the mixed binary. However, as static snapshots, these studies fail to explain how changes in the initial configuration affect the binary evolution which leads to the final state. Such methods cannot model the underlying astrophysical processes or gravitational wave templates. Hence, to understand the relationship between initial data and merger dynamics, we require general relativistic hydrodynamical (GRHD) evolutions of these static sequences.

Initial simulations of neutron star black hole mergers were performed for non-spinning binary systems with polytropic star models [85–89]. These works focused on understanding the effect of variations in mass ratio and stellar compactness on the mixed binary dynamics and remnant formations. For configurations below critical mass ratio curve, tidal

forces deformed the neutron star structure leading to a cusp formation which initiates the process of mass shedding [85, 86]. Before the star reaches ISCO, most of its inner core material is removed by the black hole and the star is tidally disrupted. The absorption of stellar core increases the remnant black hole mass to more than 84% of the total mass, as found in most simulated configurations [78, 90]. As the inner material continues to accrete on the black hole, the angular momentum is transported to the leftover material of the star which expands outwards forming a circular arm. The differential rotation in the gravitationally bound material leads to the formation of axisymmetric disk. The mass and size of the disk heavily depends on the mass ratio and compactness of the binary [85]. For configurations closer to the critical mass ratio, the disk mass is extremely low as most of the material is absorbed by the black hole before the star is disrupted. For higher mass ratio systems (or higher compactness cases), the star barely suffers any disruption until reaching ISCO beyond which all of the stellar material shares a common fate. Shibata et al.[85] and Etienne et al. [86] showed that non-spinning mixed binaries with mass ratio $q \gtrsim 4$ and realistic neutron star size ($10 - 15$ km) would have almost negligible leftover material with masses less than $10^{-2} M_{\odot}$.

Numerical studies on spinning systems revealed more interesting features of NSBH coalescence. In post-Newtonian theory, the coupling of spins with orbital angular momentum generates a repulsive force which can decrease the decay rate of orbital separation in aligned spins configurations [91–93]. Inverse effects are predicted for anti-aligned cases. For spinning black holes, spin-orbit coupling also affects the binding energy of the system reducing the orbital radius of ISCO [78]. As a result, it needs to dissipate energy for longer duration in order to reach ISCO distance. These combined effects would result in longer evolution timescales for spinning binaries (with aligned spins) which in turn would affect the tidal disruption condition and remnant properties. Various group [58, 59, 94–100] have studied the effects of black hole spin on the tidal disruption for wide range of parameter space including mass ratio, equation of state and eccentricity. Systems with low

mass ratios and high black hole spins ($a > 0.75$) were found to generate strong dynamical ejections and massive accretion disks due to early disruption of the star far outside the ISCO [58]. For such scenarios, Foucart et al. [96, 98] showed that the mass of the disk can reach as large as $\sim 36\%$ of stellar mass. For more massive black holes with smaller spins ($a \lesssim 0.75, q \gtrsim 5$), tidal disruption still occurs but only close to ISCO which creates matter ejecta in the vicinity of the black hole. As a result, the mass of accretion disks is smaller in this case and depends on the black hole spin [58, 59]. Lastly, for systems with negative spins, neutron stars do not suffer any disruption and are almost entirely engulfed by the black hole [58]. Thus, the presence of high spins can significantly increase the critical mass ratio. Black hole spin also plays a crucial role in relativistic jet formation as revealed by recent studies [99]. Initial studies with three different spin configurations showed the formation of a jet only for black holes with aligned spin ($a = 0.5$). The nonspinning system lacked strong magnetic pressure gradients, while the system with antialigned spin ($a = 0$) barely had any disk material left.

In addition to spin magnitude, the orientation of black hole spin can also affect the merger dynamics. Studies of precessing configurations with polytropic stars have shown that for a given mass ratio and spin of the black hole, the mass of the accretion disk has a negative correlation with the inclination angles (i.e. the angle between black hole spin and orbital angular momentum) and any interesting effects are observed only for angles $\gtrsim 40^\circ$ [96, 97]. These results can be understood from the post-Newtonian theory according to which the repulsive force from spin orbit coupling depends on the inner product of black hole's spin and orbital angular momentum. As the inclination angle increases, the repulsive force becomes weaker and system behaves similar to non-spinning NSBH, thus leading to early disruption and low accretion disk mass. More realistic models with nuclear theory based equations of state [59, 98] also found variations in the velocity profile of the ejecta, geometry of the accretion disk and tidal tails in comparison with polytropic models. As the system evolved to post merger phase, the inclination angles of the disk and

the black hole spin decrease to moderate values with respect to the total angular momentum of the system [59, 96].

Apart from the mass ratio and black hole spin, a weak relationship of disruption process and remnant properties also exist with the equation of state. Dependence on the equation of state is reflected by two measures - first the stellar radius, and second the density profile. Initial works on mixed binaries relied on gamma law models of the star with polytropic and piecewise polytropic equations of state. For these systems, [56–59] showed that larger radii stars or stars with uniform density profiles are more susceptible to tidal disruptions compared to more compact configurations or stars with smaller adiabatic index (leading to more concentrated density regions at stellar center). In such models, the disk mass showed an inverse relationship with compactness irrespective of the BH spin orientation [59]. Further, disk morphology, maximum density and ejecta velocity also showed a weak dependence on the equation of state. More recent studies [72] have now developed capabilities to model neutron stars using realistic equations of state which allows the study of temperature and composition of matter.

1.2. Gravitational Wave Detection Studies

Numerical studies of the NSBH mergers have shown that the impact of the initial configuration also extends to gravitational wave signatures in the late inspiral-merger-ringdown (IMR) phase. For non-spinning systems, the neutron star tends to mimic the black hole behavior for non-disruptive scenarios. The absorption of neutron star material in this case excites the fundamental quasinormal mode of the black hole resulting in ringdown signal. The dominant (2,2) mode of gravitational wave strain was found to be in good agreement with BBH based gravitational wave templates like Taylor-T4 [85]. However, in case of tidal disruption, the amplitude of gravitational signal is highly suppressed close to the merger

which results in strong deviations from BBH based templates due to the lack the tidal deformation information in the latter. The disruption process is also followed by continuous accretion on the black hole surface. This constant perturbation of black hole doesn't allow it to settle into Kerr state which affects the postmerger signal. The presence of initial black hole spin further modifies the signal template due to strong tidal effects [58, 59, 94–97]. The spin orbit coupling decelerates the orbital decay rate increasing the number of gravitational wave cycles in the inspiral regime. The slower decay of orbital separation decreases the energy carried away in the gravitational waves, which leads to longer signal duration. The black hole's spin also increases the possibility of tidal disruption scenarios, which again affects the ringdown signals even for high mass ratio systems.

Changes in morphology of the signal are more evident in the Fourier space. Gravitational wave spectrum of a binary black hole shows a gradual increase in the late inspiral region until the quasinormal (QNM) frequency beyond which steep decay of the signal amplitude is observed. The cut-off frequency in such cases is approximately given by the QNM frequency. Spectrum of non-disruptive NSBH mergers shows similar behavior as BBH signal with cut-off frequency roughly same as the QNM frequency [85, 86]. However, in case of tidal disruption, amplitude damps exponentially during the late inspiral regime before reaching the merger phase [78, 85]. The cut-off frequency in such scenarios is smaller than the QNM frequency and is strongly dependent on the compactness and equation of state of neutron star [57, 58]. Kyutoku et al. performed systematic studies of NSBH mergers to understand the relationship between cut-off frequency, compactness and equation of state. For mass ratio $q = 2$ and $q = 3$, the dependence between cut off frequency and equation of state was only found for compactness $C \lesssim 0.19$ and $C \lesssim 0.16$ beyond which cut-off frequency was same as the QNM frequency [57]. For spinning systems, Kyutoku et al. [57] showed existence of another intermediate state where amplitude of gravitational waves sinks above cut off frequency, however, it does not achieve exponential decay until reaching the QNM frequency. The cut off frequency in such scenarios

is typically smaller than 2 kHz [58].

The above discussion highlights the complex morphology and variations in the gravitational wave signal of NSBH system. These signals clearly have unique features which depends on the initial configuration of the binary. Accurate modelling to account for these features is quite important to detect and distinguish between NSBH and other compact binary systems as well as accurately estimate the parameters of the source binary. Various analytical models of gravitational wave signals try to capture these variations by including tidal dephasing and amplitude corrections due to tidal deformations [101, 102]. However, such methods rely on numerical waveforms to correctly tune the model parameters. Further, most of these models only account for a subset of the parameter space and include only a few of the relevant higher order modes which can be extremely relevant for mixed binaries (as shall be seen later in this work). Hence, to improve the analytical approximant and develop more accurate waveform templates, we require numerical relativity simulations of mixed binary system.

1.3. SIMULATING NSBH MERGERS

To model a dynamical spacetime like compact binary, numerical relativity codes rely on ADM formalism [103] which recasts Einstein's equations as Cauchy initial value problem. Under this approach, it is possible to express Einstein's equations as a system of constraint and evolution equations which describe the changes in metric and extrinsic curvature of a spatial hypersurface as a function of time [104]. One of the major challenges with this method is to find optimal initial conditions which can satisfy the constraint equations and mimic realistic astrophysical scenarios. Two well-established methods to tackle the initial data problems in numerical relativity are the conformal traceless transverse (CTT) approach [105] and the conformal thin-sandwich (CTS) approach [106, 107] which allow a clean separation of freely specifiable variables and constraint variables using conformal

decomposition [108, 109]. CTT approach achieves this separation by expressing the extrinsic curvature of spatial slice in its transverse and longitudinal components and by mapping the physical metric to some conformal metric using a scaling factor. Constraint equations are then solved for the scaling factor and longitudinal components of curvature for a given choice of other variables. Gauge variables are not included as part of this formulation and need to be selected independently. Due to conformal flatness of Schwarzschild metric, this approach is easily extendable to single or multiple static black holes. Bowen and York [110] used this approach to develop analytical solutions of momentum constraint for boosted and spinning black holes and Ansorg et al. [111] designed a spectral solver to tackle Hamiltonian constraint. To deal with the boundaries, they used asymptotic flatness condition for $r \to \infty$ and puncture approach [112] which allows integration of Hamiltonian constraint on the entire domain (including inside the horizon) thus averting the need for internal boundary conditions. This method is widely popular for BBH initial data but has also been used for neutron star black hole systems [113].

Although CTT provides a simple system of equations, it lacks the description of time evolution of the system due to ambiguity in gauge choice. CTS provides an alternative solution by specifying the initial data on two slices by formulating the problem in terms of the metric and its time derivatives. In addition, gauge variables are also included as part of the initial data formulation [114]. Though more complex in nature, this formulation is extremely useful for situations where finding optimal gauge conditions is nontrivial. CTS initial data is widely popular in simulating matter binaries [115–133] and is predominantly used by most groups. However, it relies on excision technique to model the black holes which requires additional boundary conditions inside the horizon [2]. Excision complicates the topology of numerical domain and may require special coordinate system and gauge choices [114] thus making it difficult to apply. Further, using excised initial data

[2] We note that puncture based approach for CTS has been explored but not fully developed [134]

for spacetime evolutions with BSSNOK [135–137] or Z4c formalism [138–142] requires additional boundary conditions for superluminal gauge modes which can cross black hole horizons [114]. To tackle these issues, few groups replace the excised region with some junk data inside the black hole which may not satisfy the constraints. But, this solution requires constant monitoring of constraint violation near the horizon.

To tackle these challenges of CTS approach, Clark et al. [143] developed a new initial data method using CTT approach for compact binaries with matter. Under the assumption of spherically symmetric sources, the method extends Bowen-York solutions of the momentum constraints to compact objects with matter. These solutions can then be leveraged to solve the Hamiltonian constraint using the spectral solver designed by Ansorg. Such a method has several advantages. It leverages puncture approach to model black hole interiors thus avoiding additional hassle to deal with complicated grid domains and boundary conditions to deal with superluminal gauge modes. This makes it ideal solution for puncture based codes such as Maya and Einstein Toolkit [144] which utilize BSSNOK formalism [135–137] for spacetime evolution. It should be noted that although there exist initial data methods to study both BBH and DNS in LORENE library which is supported in Einstein Toolkit, NSBH solutions are more complex and currently not supported in Einstein Toolkit.

The puncture approach also permits the study of black hole interiors which has recently gained a lot of attention due to many interesting features [145–149]. Extension of Bowen-York solutions allows a natural introduction of boost and spins to neutron stars in the initial data while satisfying the constraint equations which can be challenging with CTS based methods. Given the boosted or spinning neutron star metric is not conformally flat, such a solution would be expected to be only an approximate initial data. However, this is a common approximation even in CTS methods and hence, the two methods would be expected to be comparable.

In this work, we would like to study neutron star black hole mergers using numerical relativity simulations. The goals of this work are the following

1. Develop the modelling capabilities for NSBH mergers using method proposed in [143] for puncture based softwares.

2. Test the efficiency of initial data method and identify any sources of systematic errors.

3. Investigate the dependence of NSBH merger dynamics with initial data.

4. Identify key features which can help to distinguish between NSBH and BBH signals, if any differences exist.

In this work, we focus our attention on non-spinning neutron star black hole mergers and study the dynamics, properties and gravitational wave signatures of these objects using the initial data approach developed in reference [143]. In chapter 2, we dive into the initial data method and numerical infrastructure used for this study. We provide a detailed discussion of the framework and design of this method, and advantages and some of the current problems. This is followed by a brief summary of spacetime and hydrodynamic evolution codes, computation of gravitational wave templates and measuring the characteristics and properties of the system. Chapter 3 focuses on study of neutron star black hole mergers for varying mass ratios. We present the results of convergence test and violations in constraint equations. This is followed by a detailed comparison of binary dynamics, remnant properties and gravitational wave signatures between BBH and NSBH systems. We also compare our simulations results with already published works and find comparable results. At the end of this chapter, we discuss some of the main sources of systematic errors observed in our simulation and their impact on our results. Chapter 4 further investigates the systematic errors from conformal flatness assumption and develops a new method to account for its impact on the black hole masses and spins. In chapter 5, we

continue our investigation of neutron star black hole mergers for varying compactness of neutron stars. We analyse the effect of compactness on the merger dynamics and source properties and compare these systems and their gravitational wave signatures with BBH case. We finally conclude this work with a brief summary and discussion of a few ongoing and future research projects which would be interesting to investigate.

CHAPTER 2

NUMERICAL RELATIVITY SIMULATION INFRASTRUCTURE

Einstein's equations [150] describes the nature of spacetime and hence, its solutions are extremely desirable to understand various astrophysical scenarios. However, the general solutions of these equations cannot be obtained using traditional methods and only a few analytical solutions exist under special symmetry conditions (refer [151] for a detailed survey). Numerical relativity presents an alternate way to solve these equations for truly dynamical systems. However, modeling a dynamical system using numerical simulations requires the development of robust computational infrastructure and mathematical formalism to tackle partial differential equations which has been a long standing challenge in this field (check [152] for a historical review). Although significant progress has been made in recent years to resolve various problems such as solving initial data problems for a variety of systems, designing suitable mathematical frameworks for stable spacetime and hydrodynamical evolution, finding1 optimal gauge conditions and avoiding gauge artifacts, many of these depend on the choice of system and still remain hot topics of research.

In this chapter, we briefly review the initial data problem for compact binaries with matter and then dive into our current methods and tools used in this work for performing numerical simulations of neutron star black hole binaries. Section 2.2 and 2.3 details the "3+1" formalism and initial data problem for mixed binaries. This is followed by a description of the recent method developed by [143], its implementation, advantages and

problems with this method. 2.4 covers the "BSSN" formalism for spacetime evolution, relevant gauge and boundary conditions, 2.5 summarizes the "Whisky" code for solving hydrodynamics equations and 2.6 describes the relevant quasilocal properties of the system. The last section 2.7 talks about computing the gravitational waves signatures and radiated quantities. For this chapter we will use the standard text of Baumgarte and Shapiro [104] as our main reference.

2.1. NOTATION

For convenience, we will adopt the notations from [104] with minor changes. Let us briefly review the notation used -

- *Indices* - Latin indices from $a, b....h$ denote spacetime index from $0, ...3$ while those from $i, j...p$ describe only spatial index $1, 2, 3$. Repeated index implies Einstein's summation convention.

- *Tensors* - Metric dependent tensors in four dimensions are assigned a superscript $^{(4)}$ to distinguish them from their counterparts in three dimensional hypersurface. Tensors in conformal space will be denoted by tilde. Covariant derivatives on a four dimensional manifold are denoted by ∇ while on a three dimensional spatial hypersurfaces by D.

- *Metric* - The signature of metric is assumed to be $(-, +, +, +)$.

- *Units* - We assume geometric units throughout this work except occasional shift to polytropic units in chapter 3which will be clearly stated in the respective sections. Thus, $G = c = 1$.

2.2. ADM FORMULATION

The theory of relativity defines spacetime as a four-dimensional manifold $\mathfrak{M}$ with metric $\mathbf{g}$. For any two nearby events, the invariant interval is given by

$$ds^2 = g_{ab}\, dx^a\, dx^b \tag{2.1}$$

According to the general theory of relativity, the presence of matter and energy can induce intrinsic curvature in the spacetime which is manifested as the force of gravity. This curvature in turn governs the dynamics of matter as described by Einstein's field equations as

$${}^{(4)}G_{ab} \equiv {}^{(4)}\ R_{ab} - \frac{1}{2}\, g_{ab}\, {}^{(4)}R + \Lambda\, g_{ab} = 8\pi\, T_{ab} \tag{2.2}$$

where ${}^{(4)}R_{ab}$ is the Ricci tensor, ${}^{(4)}R = {}^{(4)}R^a_a$ is the Ricci scalar, Λ is cosmological constant and T_{ab} is the energy momentum tensor. The flow of matter is also constrained by the continuity equation

$$\nabla_a T^{ab} = 0 \tag{2.3}$$

Equations 2.2 are a set of ten coupled partial differential equations relating the geometry of spacetime with its matter content. Under the assumptions of stationary and static conditions, it is possible to obtain the analytic solutions of these equations [151]. However, most of the astrophysical systems, such as compact binary mergers, are highly dynamical in nature and hence, cannot be modeled analytically.

A common method to numerically solve these equations utilizes the "3+1 approach. Consider the foliation of spacetime into three dimensional spatial surfaces, Σ which do not intersect at any point. These surfaces can also be thought as level surfaces of some scalar function t. One can then define the normals to these slices as

$$n^a = -\alpha g^{ab} \nabla_b t \tag{2.4}$$

where α is the lapse function which measures the difference in proper time between two slices. Mathematically, it can be expressed as

$$\alpha = (-g^{ab}\nabla_a t \nabla_b t)^{-1/2} \tag{2.5}$$

The choice of negative sign ensures that normal points in the positive time direction. With the normal vectors, we can now construct the induced metric γ_{ab} on the spatial surface Σ:

$$\gamma_{ab} = g_{ab} + n_a n_b \tag{2.6}$$

While induced metric can be used to completely describe the internal structure of the spatial slice such as distance, Gaussian curvature etc., one needs to look at the extrinsic curvature in order to understand how each slice is embedded into the spacetime itself. Mathematically, extrinsic curvature describes the rate of deformation of the spatial surface in the direction of normal vector:

$$K_{ab} = -\gamma_a^c \gamma_b^d \nabla_c n_d \tag{2.7}$$

Thus, with the notions of induced metric and extrinsic curvature, one can get complete information about each leaf of the foliation. The last missing piece of the puzzle is the connection between these leaves, which can be given by the direction of time. One can think of choosing the direction of normals as the direction of time function (which connects any two slices), however, the normal vector is not dual to the gradient of time, i.e.

$$n^a \Omega_a = -\alpha g^{ab}\nabla_a t \nabla_b t = \alpha^{-1} \tag{2.8}$$

One can alternatively define the time vector as $t^a = \alpha n^a + \beta^a$, where β^a is a spatial shift vector, which measures the shift in the spatial coordinates within a slice w.r.t. normal vector. It can be easily shown that t^a is dual to the gradient of time and hence, would

provide the right direction to move from one spatial slice to the other.

Having developed the basic notions to describe the foliation of spacetime, the next question is how can we compute these quantities for each leaf of the foliation? As Einstein's equations describe the dynamics of spacetime metric, the simplest method is to project these equations on the spatial slices. After some calculations, one can obtain the ADM (Arnowitt-Deser-Misner) equations which consist of four constraint equations from the time component of Einstein's equations and twelve evolution equations describing the spatial metric and extrinsic curvature as functions of time.

Hamiltonian Constraint:

$$R + K^2 - K_{ij}K^{ij} = 16\pi\rho_H \tag{2.9}$$

Momentum Constraint:

$$D_j(K^{ij} - \gamma^{ij}K) = 8\pi S^i \tag{2.10}$$

Evolution Equation - Spatial Metric:

$$\partial_t \gamma_{ij} = -2\alpha K_{ij} + 2D_{(i}\beta_{j)} \tag{2.11}$$

Evolution Equation - Extrinsic Curvature:

$$\begin{aligned}\partial_t K_{ij} = &\alpha\left(R_{ij} - 2K_{ik}K^k_j + KK_{ij}\right) - D_iD_j\alpha - 8\pi\alpha\left(S_{ij} - \frac{1}{2}\gamma_{ij}(S - \rho_H)\right) \\ &+ \beta^k\partial_k K_{ij} + K_{ik}\partial_j\beta^k + K_{kj}\partial_i\beta^k\end{aligned} \tag{2.12}$$

Here, $\rho_H = n_a n_b T^{ab}$ is the Hamiltonian energy density as observed by a normal observer, $S^i = -\gamma^{ij}n^b T_{jb}$ is the momentum density and $S_{ij} = \gamma_{ia}\gamma_{jb}T^{ab}$ is the stress tensor on the spatial slice. S is the trace of the stress tensor projected on the hypersurface. Notice that ADM equations do not provide any information or constraints about the choice of gauge.

2.3. INITIAL DATA

In order to solve the ADM equations, one requires the configuration of the system at some initial time. One of the primary challenges in modeling compact binary mergers is finding the optimal initial data, which provides a realistic representation of gravitational fields of the system and also satisfies the constraint equations 2.9, 2.10. This can be seen by analysing the degrees of freedom. The intrinsic metric γ_{ij} and extrinsic curvature K_{ij} of any spatial slice Σ each have 6 components. Four of these can be determined using constraint equations 2.9, 2.10 while coordinate selection fixes the other four components. The remaining components are completely unknown, providing four degrees of freedom in choosing the initial data.

In this section, we present a brief review of a recent new method developed in [143], [153] to formulate initial data for compact binary mergers. This method utilizes the conformal transformations to separate the dynamical degrees of freedom and extends Bowen York approach to find the analytical solutions to Momentum Constraints. In this work, we adopt this method to study mixed binary mergers. In the next subsection we first provide a brief overview of conformal transverse traceless (CTT) approach [105] and conformal thin sandwich (CTS) approach. This is followed by a description of initial data from [143, 153], algorithm and implementation, its advantages and flaws.

2.3.1. CONFORMAL TRANSVERSE TRACELESS (CTT) APPROACH

CTT approach focuses on separating the transverse and longitudinal degrees of freedom by expressing metric and curvature in conformal space. One starts with the following transformation of the spatial metric

$$\gamma_{ij} = \psi^4 \tilde{\gamma}_{ij} \tag{2.13}$$

Here, ψ represents the conformal factor, and $\tilde{\gamma}_{ij}$ represents the conformal metric. The degrees of freedom is distributed with one in ψ and five in $\tilde{\gamma}_{ij}$. Due to presence of scaling factor ψ, the determinant of $\tilde{\gamma}_{ij}$ can be set to one which yields $\gamma = \psi^{12}$. In a similar fashion, the transformation of extrinsic curvature is given by

$$K_{ij} = A_{ij} + \frac{1}{3}\gamma_{ij}K \tag{2.14}$$

$$A_{ij} = \psi^{-2}\tilde{A}_{ij} \tag{2.15}$$

Here, K is the trace of extrinsic curvature while A_{ij} is the traceless part. Applying Lifschitz decomposition (tensor analog of Helmholtz theorem), the conformal traceless part can be expressed in terms of transverse and longitudinal components as

$$\tilde{A}^{ij} = \tilde{A}^{ij}_{TT} + \tilde{A}^{ij}_{L} \tag{2.16}$$

$$\tilde{D}_j\tilde{A}^{ij}_{TT} = 0 \tag{2.17}$$

$$\tilde{A}^{ij}_{L} = 2\tilde{D}^{(i}\mathcal{W}^{j)} - \frac{2}{3}\tilde{\gamma}^{ij}\,\tilde{D}_k\mathcal{W}^k \equiv \left(\tilde{L}\mathcal{W}\right)^{ij} \tag{2.18}$$

With these transformations, the Hamiltonian constraint takes the form

$$8\tilde{D}^2\psi - \psi\tilde{R} - \frac{2}{3}\psi^5K^2 + \psi^{-7}\tilde{A}_{ij}\tilde{A}^{ij} = -16\pi\psi^5\rho_H \tag{2.19}$$

and the momentum constraints are given as

$$(\tilde{\nabla}_L\,\mathcal{W})^i - \frac{2}{3}\psi^6\,\tilde{\gamma}^{ij}\,\tilde{D}_j\,K = 8\pi\,\psi^{10}\,S^i \tag{2.20}$$

Here, $\tilde{\nabla}$ is the vector Laplacian and $(\tilde{\nabla}_L\mathcal{W})^i = \tilde{D}^2\mathcal{W}^i + \frac{1}{3}\tilde{D}^i(\tilde{D}_j\mathcal{W}^j) + \tilde{R}^i_j\mathcal{W}^j$. For given $\tilde{\gamma}_{ij}$, K and $\tilde{A}^{ij}_{TT}$ and matter terms, we can solve the constraint equations to determine ψ and $\mathcal{W}^i$. Using these solutions, it is possible to reconstruct the metric and curvature in physical space which yields the initial data on some spatial slice Σ.

2.3.2. CONFORMAL THIN SANDWICH (CTS) APPROACH

Using the CTT approach provides a clear way to determine the metric and curvature of a single hypersurface. However, one still lacks the connection between coordinates from two neighbouring slices, which adds to the complications of the initial data. While this gauge freedom can be exploited in different ways, finding an optimal gauge condition is a complex problem. CTS approach resolves this issue by specifying the metric γ_{ij} and its time derivative u_{ij} on the initial slice Σ defined as

$$u_{ij} \equiv \gamma^{1/3} \partial_t \left(\gamma^{-1/3} \gamma_{ij} \right) \tag{2.21}$$

Performing a conformal transformation, the time derivative of conformal metric is defined as

$$\tilde{u}_{ij} \equiv \partial_t \tilde{\gamma}_{ij} \tag{2.22}$$

$$\tilde{\gamma}^{ij} \tilde{u}_{ij} \equiv 0 \tag{2.23}$$

where $\gamma_{ij} = \psi^4 \tilde{\gamma}_{ij}$ and the last relation ensures that $\tilde{\gamma} = constant$. The conformal traceless extrinsic curvature can be expressed as

$$\tilde{A}_{ij} = \frac{\psi^6}{2\alpha} \left((\tilde{L}\beta)^{ij} - \tilde{u}^{ij} \right) \tag{2.24}$$

Using these transformations, the momentum and Hamiltonian constraint equations can then be written as

$$\left(\tilde{\Delta}_L \beta\right)^i - (\tilde{L}\beta)^{ij} \tilde{D}_j \ln(\tilde{\alpha}) = \tilde{\alpha} \tilde{D}_j \left(\tilde{\alpha}^{-1} \tilde{u}^{ij} \right) + \frac{4}{3} \tilde{\alpha} \psi^6 \tilde{D}^i K + 16\pi \tilde{\alpha} \psi^{10} S^i \tag{2.25}$$

$$\tilde{D}^2\psi - \frac{1}{8}\psi\tilde{R} - \frac{1}{12}\psi^5 K^2 + \frac{1}{8}\psi^{-7}\tilde{A}_{ij}\tilde{A}^{ij} = -2\pi\psi^5\rho \tag{2.26}$$

Here $\tilde{\alpha} = \psi^6\alpha$ is densitized lapse. For given choice of $\tilde{\gamma}_{ij}, \tilde{u}_{ij}, K$ and $\tilde{\alpha}$, we can solve the constraint equations to determine ψ, β^i which completes the initial data.

2.3.3. BOWEN YORK TYPE INITIAL DATA

Using CTT approach, Bowen and York [110] first obtained analytical solutions for momentum constraint for binary black hole system. Their method was recently extended by [143] to any compact binary system. Here, we present a brief review of this method. We start with the assumption that matter can be modeled with perfect fluid energy momentum tensor which is given by

$$T_{ab} = (\rho + p)u_a u_b + p g_{ab} \tag{2.27}$$

Here, ρ is the total energy density, p is pressure, u^a is four velocity of fluid elements. We can define the specific enthalpy as $h = 1 + \epsilon + \frac{p}{\rho_o}$ where ρ_o is rest mass density and ϵ is specific internal energy density. For this case, the Hamiltonian and momentum densities can be written as

$$\rho_H = (\rho + p)\, W^2 - p \tag{2.28}$$

$$S^i = (\rho + p)\, W\, u^i \tag{2.29}$$

Here $W = -n^a u_a$ represents the Lorentz factor relating the coordinate transformations between fluid and normal observers at an instant of time. As the spacetime is dynamical, one can only define local inertial frames in this case. Since the LHS of equations 2.19, 2.20 exists in conformal space, we apply the following transformations for the matter terms -

$$\tilde{\rho}_H = \rho_H \psi^8 \tag{2.30}$$

$$\tilde{S}^i = S^i \psi^{10} \tag{2.31}$$

In addition, we can also assume $\tilde{\rho} = \rho\psi^8$, $\tilde{p} = p\psi^8$ and $\tilde{u}^i = u^i\psi^2$. Under these assumptions, the Hamiltonian and momentum density continue to obey relations 2.28 in conformal space as well. As the four velocity of fluid elements remain timelike, $u_a u^a = -1$. Combining this relation with the definition of Lorentz factor, we get

$$W^2 = \tilde{W}^2 = \frac{1}{2}\left(1 + \sqrt{1 + \frac{4\tilde{\gamma}_{ij}\tilde{S}^i\tilde{S}^j}{(\tilde{\rho}+\tilde{p})^2}}\right) \tag{2.32}$$

Using the above transformations, we can simplify the constraint equations. As seen in subsection 2.3.1, CTT carries additional free parameters in the form of conformal metric, the trace of curvature and its transverse components. To fix these, Clark et al. made the standard assumptions of conformal flatness ($\tilde{\gamma}_{ij} = \eta_{ij}$), maximal slicing ($K = 0$) and vanishing transverse curvature components ($\tilde{A}^{ij}_{TT} = 0$). Applying these assumption to equations 2.19 and 2.20, the constraints transform as

$$8\tilde{D}^2\psi + \psi^{-7}\tilde{A}_{ij}\tilde{A}^{ij} = -16\pi\psi^{-3}\tilde{\rho}_H \tag{2.33}$$

$$(\tilde{\nabla}_L \mathcal{W})^i = 8\pi\tilde{S}^i \tag{2.34}$$

Following Bowen's approach [154], to obtain the analytical solutions of the Momentum constraint, let's assume source terms of the form

$$\tilde{S}^i = P^i\sigma(r) \tag{2.35}$$

$$\tilde{S}^i = \epsilon J^j x^k \kappa(r) \tag{2.36}$$

Here, $\sigma(r)$ and $\kappa(r)$ are radial functions for the source with $r < R_s$, the radius of the source in isolation. Setting $\int_0^{R_s} 4\pi\sigma r^2 dr = 1$ and $\frac{8\pi}{3}\int_0^{R_s} \kappa r^4 dr = 1$, P^i and J^i can be identified as the ADM linear and angular momentum under the assumption that $\psi \to 1$ as $r \to \infty$ in both physical and conformal space. To find the source functions for objects with linear

momentum, we substitute the expressions for the conformal momentum density in the above equations -

$$\tilde{S}^i = (\tilde{\rho} + \tilde{p}) W \tilde{u}^i = P^i \sigma \tag{2.37}$$

Similarly, for sources with angular momentum

$$\tilde{S}^i = (\tilde{\rho} + \tilde{p}) W \tilde{u}^i = \epsilon_{ijk} J^j x^k \kappa \tag{2.38}$$

Here, source function $\sigma(r) = (\tilde{\rho} + \tilde{p})/\mathcal{K}$ and $\kappa(r) = (\tilde{\rho} + \tilde{p})/\mathcal{N}$ where $\mathcal{K}, \mathcal{N}$ are normalization constant determined from integrability conditions of σ and κ described above. Using these, we can now solve the momentum constraint for $\mathcal{W}^i$. Substituting the solutions in 2.16, the conformal extrinsic curvature is given by

$$\tilde{A}^{ij} = \frac{3Q}{2r^2}\left[2P^{(i}l^{j)} - (\eta^{ij} - l^i l^j)P_k l^k\right] + \frac{3C}{2r^4}\left[2P^{(i}l^{j)} - (\eta^{ij} - 5l^i l^j)P_k l^k\right] \tag{2.39}$$

$$\tilde{A}^{ij} = \frac{6}{r^3} l^{(i} \epsilon^{j)kl} J_k l_l N \tag{2.40}$$

It can be easily seen that the above solution reduces to Bowen-York solution in absence of source terms. Here, $l^i = x^i/r$ is unit directional vector, $Q = \int_0^r 4\pi\sigma\, r'^2\, dr'$, $C = \int_0^r \frac{2}{3}\pi\sigma\, r'^4\, dr'$ and $N = \frac{8\pi}{3}\int_0^r r'^4\, \kappa\, dr'$. To solve the Hamiltonian constraint, we can directly use the analytical solutions for conformal extrinsic curvature with conformal Hamiltonian density in equation 2.33. This brings equation 2.33 into the following form -

$$\tilde{D}^2\psi + \zeta(\psi) = 0 \tag{2.41}$$

where $\zeta(\psi)$ is some function of ψ. Ansorg et al. [111] developed an spectral approach to solve equations of this form which can be directly applied in this case. Solution for conformal factor thus completes the system. The spatial and matter variables on the hypersurface

Σ can be obtained by translating conformal variables to physical space using the solution of ψ.

2.3.4. Algorithm and Code Structure

Let's take a brief look at various steps to construct the initial data using this method. For a more detailed implementation, look at chapters 5 and 6 of [153] -

1. Select the initial configuration which is determined by the system type, desired separation D_{NR} of the binary, desired (target) masses $M^{(1)}, M^{(2)}$ and spins, $\vec{S}^{(1)}, \vec{S}^{(2)}$ of each object at the initial time of evolution. The total mass of the system is $M = M^{(1)} + M^{(2)}$ and mass ratio is given by $q = M^{(1)}/M^{(2)}$.

2. To obtain the initial momenta of the binary, consider a system of two point masses with total mass M now scaled to 1, mass ratio q and spin vectors $\vec{S}^{(1)}, \vec{S}^{(2)}$ at a large separations $D_{PN} >> D_{NR}$. Employing point particle assumption at such large distances, evolve the system using post Newtonian (PN) theory till the desired separation D_{NR} is achieved. Integrating highest order PN equations of motion yields the linear and angular momenta with small eccentricities. In presence of precessing spins, use $\vec{S}^{(1)}, \vec{S}^{(2)}$ as the initial guess of spins at D_{PN} and iteratively update the initial guess (for example, by using gradient descent or Newton's method) until the desired orientation of spin vectors at D_{NR} is achieved.

3. At the separation D_{NR}, identify the component masses with Christodoulou mass if black hole and with ADM mass if star. Note the correction here for black hole. (In original reference, the component mass was related with irreducible mass of the black hole instead of ADM mass.)

4. To obtain the initial data, use 2.39 for Momentum constraint and modified TwoPunctures code [111] for Hamiltonian constraint solutions. For this, one requires base

model for each object to compute the relevant source functions and other parameters. For binaries with stars, we can adopt a spherically symmetric model of star (such as TOV model) with central density ρ_c which yields its ADM mass $\mathcal{M}_A^{(i)}$ and rest mass $\mathcal{M}_o^{(i)}$ in isolation. To model the black hole, use the puncture approach [112] with puncture mass $\mathcal{M}_p^{(i)}$. Here, i is the object index.

5. Using the base model, compute the conformal quantities and solution for momentum constraint. For binaries with star, the source functions σ, κ can be calculated from equations 2.37, 2.38 in which the linear and angular momenta can be obtained from PN solutions. The total traceless conformal extrinsic curvature is $\tilde{A}_1^{ij} + \tilde{A}_2^{ij}$. In addition, also compute the conformal Hamiltonian density $\tilde{\rho}_H = (\tilde{\rho} + \tilde{p})Wu^i$.

6. Solve the Hamiltonian constraint for conformal factor using the method illustrated in [111]. Compute the ADM variables γ_{ij}, K_{ij} using conformal relations. For gauge conditions, we adopt the same condition as in binary black hole where $\alpha = \psi^{-2}$ and initial shift to 0.

7. To compute the hydro variables, invert the conformal transformations of momentum and Hamiltonian density using equations 2.30, 2.31. Using relations $W = \tilde{W}$ and $u^i u_i = -1$, solve for pressure and compute rest mass density using equation of state. Four velocity can then be determined from momentum density equation 2.29.

8. Compute the new Christodoulou mass $\hat{\mathcal{M}}_h^{(i)}$ if black hole, and rest mass $\hat{\mathcal{M}}_o^{(i)}$ if star. For black hole, it is possible to define a local concept of mass measured at the asymptotically flat regions of the puncture which resemble the ADM mass of an isolated black hole [111, Equation 83]. For neutron stars, the situation is more complex as such measurements are not possible. There exist two definitions for mass of isolated

neutron stars - the rest mass

$$\mathcal{M}_o = \int_\Sigma \rho_0 \sqrt{\gamma} \alpha u^t dV \tag{2.42}$$

and the ADM mass

$$\mathcal{M}_A = -\frac{1}{2\pi} \int_{\partial\Sigma_\infty} \tilde{\nabla}^i \psi dS_i \tag{2.43}$$

In order to keep consistency with BBH, we define the new mass of star as $\hat{\mathcal{M}}_S^{(i)} = \xi \hat{\mathcal{M}}_o^{(i)}$ where $\xi = \mathcal{M}_A^{(i)} / \mathcal{M}_o^{(i)}$. Here, $\mathcal{M}_A^{(i)}$ ($\mathcal{M}_o^{(i)}$) represents the ADM (rest) mass of star in isolation while $\hat{\mathcal{M}}_o^{(i)}$ represents the rest mass of star (when part of the binary).

9. Recompute the new mass ratio $\hat{q}$ and total mass $\hat{M}$ in terms of $\hat{\mathcal{M}}_h^{(i)}$ and/or $\hat{\mathcal{M}}_S^{(i)}$. If the total mass and mass ratio vary from desired values by more than given tolerance, modify the puncture mass and central density using secant algorithm. Repeat from step 5.

2.3.5. Code Modification and Initial Data Pipeline -

To implement the above method, Michael Clark developed an initial data library using the available infrastructure of Maya code, which handled different steps in initial data construction. Let's look at various pieces (called thorns) of this library -

1. Post Newtonian Calculation - The computation of linear and angular momenta of the binary in Step 2 is achieved using PNevo code developed by James Healey.

2. BowenID - This thorn sets up the initial model of the star and black hole and computes solution for momentum constrains and conformal Hamiltonian density (Step 4 and 5).

3. TwoPuncturesSolver - A modified version of TwoPunctures, it solves the Hamiltonian constraint for conformal factor ψ using the spectral method using solutions of

$\tilde{A}_{ij}$ and $\tilde{\rho}_H$ from BowenID. It then interpolates ψ from spectral to Cartesian grid and computes the ADM variables $\gamma_{ij}, K_{ij}, \alpha, \beta^i$. (Step 6)

4. PrimitiveSolver - Using the ADM variables computed in TwoPuncturesSolver and hydro variables of TOV from BowenID, it reconstructs the hydro variables using inverse conformal transformation (Step 7).

5. Broyden - This thorn iteratively computes the initial data using BowenID, TwoPuncturesSolver and PrimitiveSolver and alters the central density of star and puncture mass of black hole until the desired configurations are achieved (Step 8).

The above library provides all the necessary tools to generate the initial data for a mixed binary system. The code works almost flawlessly and is extremely fast in computing the initial data for desired configuration. However, there are a few problems with this infrastructure. The architecture and design of the original code is quite complex and lacks modularity. In particular, the equation of state is hard coded to a polytropic model which restricts including any additional physics. The base model construction of the isolated compact objects, and computation of the source functions in BowenID is performed in a nested structure of dependent classes which makes adding any new model difficult due to the inbuilt assumptions of each class. The present code also inherits from Whisky (hydro evolution code) which generates dependencies between the two thorns rendering it non-usable with other GRMHD codes. The Broyden method itself does not guarantee convergence and can fail for a certain guess of puncture mass and central density of stars. Lastly, the constructed parameter file from this method is non-optimized, which increases the computational cost of evolution significantly. This is a major issue for mixed binary systems whose simulations require additional refinement levels and higher resolutions than a BBH or DNS simulation due to the differences in the size and type of objects. These issues combined with the lack of documentation of these codes make the simulations of mixed binaries extremely challenging for any new user.

To simplify these problems, we modified the current infrastructure and heavily automated the process of initial data generation. As a first step, we rewrote the BowenID code into two different thorns - SourceProfile and MomentumConstraintSolver, which decouples the source modeling from the computations of source functions, extrinsic curvature and Hamiltonian density. The source profile simplifies the class structure into a base class which describes a common property for each source object and a model class for each type of object (like black hole and TOV). The assumption of a polytropic equation of state is completely replaced by computing pressure and density using user-defined equation of state models. At present, polytropic and piecewise polytropic models are supported but can be easily extended to tabulated realistic equation of state models. Decoupling BowenID also gives us more flexibility to modify the conformal transformations or initial data method without affecting the source construction. We note that this work was done in parallel with the current simulations and hence has not been used for simulations presented in this work but has been tested separately.

To generalize the code to publicly available GRMHD codes, we removed the dependencies from Whisky Hydrobase code and generalized it to Einstein Toolkit [144]. Such a change makes it compatible with most other open source codes like GRHydro [155] and IllinoisGRMHD [156] which use the hydrodynamics architecture of Einstein toolkit. This required some upgrades primarily in PrimitiveSolver and Broyden. As a test, we performed a few simulations with IllinoisGRMHD and ran comparisons with our hydro code. To handle the failures of Broyden method and ensure its convergence, we introduced an additional step in initial data construction method. As a quasi-Newtonian method, the convergence of Broyden depends strongly on the function and derivative values at the starting point. As the current approach lacks a way to specify the initial guess for central density for Broyden method, we compute the central density of a static TOV with desired target mass using iterative scheme which is then used as the initial guess for Broyden Solver. This minor change not only ensures convergence but also reduces the number of

solver iterations thus decreasing the computation time for initial data. It also ensures that the constructed initial data models a TOV star which lies on the stable branch of mass-density curve [135] .

A common issue with numerical relativity simulations is choosing the parameters for each thorn. For someone interested in astrophysics rather than code development, using NR software as a black box can be extremely difficult due to the sheer number of modules (thorns) and the corresponding sets of parameters required in a single simulation. The lack of documentation adds to the challenges making it harder to perform new simulations. Although the default settings works well for most of the parameters, one still needs to select the relevant thorns, desired outputs and adjust the grid structure and boundaries, set the trackers, initial data and evolution methods, and calibrate the relevant quasilocal properties and gravitational waves thorns. Ill-conceived parameters can lead to non-convergence, low resolution, long simulation timescales or systematic errors, which can make it harder to trust the results. Hence, to minimize the user burden and improve the computational speed, we constructed separate scripts which can allow users to build an optimized simulation configuration (parameter file) based on the choice of desired system configuration. Lastly, to simplify the initial data construction for any new user, we created an automation pipeline to generate an optimized initial configuration of the simulation by integrating the libraries of Maya, optimization scripts and initial data modules with a Python-based front end. At present, the design of the pipeline is kept extremely simple with maximized automation while ensuring the modularity and user control.

2.3.6. Advantages and Problems -

Bowen-York type method [143] provides an easy and clean approach to solve the initial data problem for any compact binary system. Extension of analytical Bowen-York solutions makes this method extremely fast and efficient to compute the initial data for a variety of compact binaries including high mass ratio, spinning and eccentric systems.

The current design of the pipeline has been highly automatized making it extremely user friendly while keeping the backend codes modular which allows advance users to easily modify the pipeline. The code architecture utilizes Cactus framework [157] and hence, can be easily adapted to other NR softwares and is compatible with other GRMHD codes. Lastly, the code is convergent and works in principle for any desired configuration unless restricted by the stellar or BH models. This has usually been a known issue with other publicly available codes such as Lorene [133] which are not guaranteed to be convergent.

As with any mathematical model, the inherent assumptions made in this approach make it imperfect and can introduce systematic errors. Let us discuss the scope and limitations of this model -

- Source type - To solve the momentum constraint, we assume the source functions σ and κ to have only radial dependence. As the conformal transformations preserve angles, we inherently assume that source have spherical symmetry in the beginning. This is not entirely true in general when two objects are placed close to each other. For example, in case of mixed binary, star close to the black hole will suffer deformations due to tidal forces, excluding which results in density oscillations. Similar problems arise from artificially boosting a star. These issues are further discussed in the next chapter.

- Equation of State - The conformal transformations of ρ and p inherently assume that the pressure is a linear function of the density which places additional constraints on the equation of state models. Unfortunately most equation of state models are non-linear and hence, extending this approach to other equation of state models result in violation of at least one such transformations. Fortunately, such violations do not affect the solution significantly for our current equation of state which can be measured by the constraint equations. However, this needs to be checked for every equation of state model before extending the model.

- Conformal Flatness - The simple assumption of using flat metric as an initial guess for conformal metric results in a burst of spurious radiation which can alter the masses and spins of the binary. These changes from initial configuration can lead to variations in the gravitational wave signatures [158].

- Gauge Conditions - A common problems with CTT method is finding the optimal gauge which leads to smooth evolutions without any gauge artifacts. While various possible gauge conditions have been proposed for binary black holes [104], their direct applications to other systems like NSBH binary result in additional side effects like center of mass offsets. We go into more detail of center of mass offset in the next chapter.

2.4. SPACETIME EVOLUTION - BSSN FORMALISM

With initial data in hand, it is now possible to evolve the spatial hypersurface as a function of time to understand the dynamics of binaries. However, ADM equations 2.11, 2.12 in their present form are weakly hyperbolic and not well posed [135–137]. In other words, the solutions of ADM equations can grow exponentially with time which may cause problems with numerical evolutions of the system . One of the primary cause of this is the presence of mixed derivatives in Ricci tensor in addition to Laplace like operator of form $\gamma^{kl}\partial_k\partial_l\gamma_{ij}$ which weakens the hyperbolicity of evolution equations. BSSN formalism [104] provides an alternative method to solve this problem by treating the connection tensors as new variables. Such a change allows the elimination of the mixed double derivative terms making the system strongly hyperbolic. In addition, it also exploits the CTT approach to isolate the longitudinal (non-radiative) degrees of freedom from transverse (radiative) components by keeping the evolutions of the conformal factor and trace of curvature independent from the metric and curvature.

We will now focus on BSSN-Chi formulation of this approach [159, 160] which is primarily used for this work. We start by constructing a new map from physical to conformal space. Under this transformation, the conformal metric is given by $\hat{\gamma}_{ij} = \chi\gamma_{ij}$ [1] where $\chi = \gamma^{-1/3} = \exp(-4\phi)$ is a C^4 class function at the puncture. Here again we assume $\hat{\gamma} = 1$ (in Cartesian coordinates). The traceless extrinsic curvature in conformal space takes the following form: $\hat{A}_{ij} = \chi\left(K_{ij} - \gamma_{ij}K/3\right)$. Notice that this transformation differs from one employed in the initial data. In terms of these new variables, the ADM equations can be written as:

$$\partial_t\hat{\gamma}_{ij} = -2\alpha\hat{A}_{ij} + \mathcal{L}_\beta\hat{\gamma}_{ij} \tag{2.44}$$

$$\partial_t\hat{A}_{ij} = \chi\left(-D_iD_j\alpha + \alpha R_{ij}\right)^{TF} + \alpha\left(K\hat{A}_{ij} - 2\hat{A}_{ik}\hat{A}^k_j\right) + \mathcal{L}_\beta\hat{A}_{ij} - 8\pi\alpha\left(\chi S_{ij} - \frac{1}{3}\hat{\gamma}_{ij}S\right) \tag{2.45}$$

$$\partial_t\chi = \frac{2}{3}\chi\left(\alpha K - \partial_i\beta^i\right) + \beta^i\partial_i\chi \tag{2.46}$$

$$\partial_tK = -D^iD_i\alpha + \alpha\left(\hat{A}_{ij}\hat{A}^{ij} + \frac{1}{3}K^2\right) + \beta^i\partial_iK + 4\pi\alpha(\rho + S) \tag{2.47}$$

Here, TF refers to the trace-free part of the tensor and $\mathcal{L}_\beta$ is the Lie derivative operator along shift vector β^a. The trace-free Ricci tensor is given by $R^{TF}_{ij} = R_{ij} - \gamma_{ij}R/3$. Ricci tensor can be split into two parts $R_{ij} = \hat{R}_{ij} + R^\phi_{ij}$ which isolates terms with ϕ dependence given as -

$$R^\phi_{ij} = -2\hat{D}_i\hat{D}_j\phi - 2\hat{\gamma}_{ij}\hat{D}^k\hat{D}_k\phi + 4\hat{D}_i\phi\hat{D}_j\phi - 4\hat{\gamma}_{ij}\hat{D}^k\phi\hat{D}_k\phi \tag{2.48}$$

$$\hat{R}_{ij} = -\frac{1}{2}\hat{\gamma}^{lm}\partial_l\partial_m\hat{\gamma}_{ij} + \hat{\gamma}_{k(i}\partial_{j)}\hat{\Gamma}^k + \hat{\Gamma}^k\hat{\Gamma}_{(ij)k} + \hat{\gamma}^{lm}\left(2\hat{\Gamma}^k_{l(i}\hat{\Gamma}_{j)km} + \hat{\Gamma}^k_{im}\hat{\Gamma}_{klj}\right) \tag{2.49}$$

The covariant derivatives D_i are in physical space while $\hat{D}_i$ are defined in conformal space with respect to $\hat{\gamma}_{ij}$. The connection terms in conformal space takes the form of $\hat{\Gamma}^i = \hat{\gamma}^{jk}\hat{\Gamma}^i_{jk} =$

[1] We replace tilde with hat to distinguish between conformal transformations used in initial data and evolution equations

$-\partial_j \hat{\gamma}^{ij}$. The corresponding evolution equations for these new variables are -

$$\begin{aligned}\partial_t \hat{\Gamma}^i =& \hat{\gamma}^{jk}\partial_j\partial_k\beta^i + \frac{1}{3}\hat{\gamma}^{ij}\partial_j\partial_k\beta^k + \beta^j\partial_j\hat{\Gamma}^i - \hat{\Gamma}^j\partial_j\beta^i + \frac{2}{3}\hat{\Gamma}^i\partial_j\beta^j \\ & - 2\hat{A}^{ij}\partial_j\alpha + 2\alpha\left(\hat{\Gamma}^i_{jk}\hat{A}^{jk} + 6\hat{A}^{ij}\partial_j\phi - \frac{2}{3}\hat{\gamma}^{ij}\partial_j K\right) - 16\pi\alpha\hat{\gamma}^{ij}S_j \end{aligned} \tag{2.50}$$

The Lie derivatives for conformal metric and extrinsic curvature are -

$$\mathcal{L}_\beta\hat{\gamma}_{ij} = \beta^k\partial_k\hat{\gamma}_{ij} + \hat{\gamma}_{ik}\partial_j\beta^k + \hat{\gamma}_{jk}\partial_i\beta^k - \frac{2}{3}\hat{\gamma}_{ij}\partial_k\beta^k \tag{2.51}$$

$$\mathcal{L}_\beta\hat{A}_{ij} = \beta^k\partial_k\hat{A}_{ij} + \hat{A}_{ik}\partial_j\beta^k + \hat{A}_{jk}\partial_i\beta^k - \frac{2}{3}\hat{A}_{ij}\partial_k\beta^k \tag{2.52}$$

In addition to the above equation, one can also exploit the gauge freedom to relate the coordinates between adjacent time-slices. We adopt "1+log" slicing condition for lapse and Γ-driver condition to determine the shift vector, given as [160, 161]

$$\partial_t\alpha = \beta^i\partial_i\alpha - 2\alpha K \tag{2.53}$$

$$\partial_t\beta^i = \beta^j\partial_j\beta^i + \frac{3}{4}B^i \tag{2.54}$$

$$\partial_t B^i = \beta^j\partial_j B^i + \partial_t\hat{\Gamma}^i - \beta^j\partial_j\hat{\Gamma}^i - 2B^i \tag{2.55}$$

These gauge conditions have many desirable properties. The "1+log" condition is a special case of maximal slicing condition defined by $K = \partial_t K = 0$. Divergence of normal vectors vanishes in this gauge ($\nabla_a n^a = -K = 0$) and hence, normal observers do not contract to a point which avoids formation of coordinate singularities. Gamma driver condition is an extension of Gamma-freezing condition, which is a simpler version of the minimal distortion gauge. These gauge conditions focus on eliminating the fluctuations in the conformal metric due to coordinates by minimizing its time variation, i.e., $\partial_j\tilde{u}^{ij} = 0$ where u^{ij} is the time derivative of the metric as defined in CTS method.

Boundary conditions - We adopt the standard Sommerfield radiative boundary conditions

[160], [162] which assumes that all field variables propagate as outgoing spherical waves near the boundaries whose behavior is given by -

$$\Lambda = \Lambda_\infty + \frac{1}{r}\Theta(r - vt) \tag{2.56}$$

Here, Λ are the field variables or their components and Λ_∞ corresponds to their asymptotic values. Θ is a radial perturbation propagating at speed v. The above equations form a complete system in the absence of matter. However, in the presence of matter, we also need to solve the hydrodynamics equations to correctly determine the energy and momentum densities and stress energy tensors at any point of time. Let's look at these in the next section

2.5. HYDRODYAMICS

In addition to solving Einstein's equation, the presence of matter also requires that the continuity equation and the conservation of matter current remain satisfied. In covariant form, these equations are given by -

$$\nabla_\mu T^{\mu\nu} = 0 \tag{2.57}$$

$$\nabla_\mu J^\mu = 0 \tag{2.58}$$

Our numerical hydrodynamics is based on the public version of Whisky code designed by the researchers at AEI and collaborators [163]. Whisky adopts Valencia formulation to express these equations in flux-conservative form in terms of conservative variables

defined as

$$D \equiv \sqrt{\gamma}\rho_o W \tag{2.59}$$

$$S_i \equiv \sqrt{\gamma}\alpha T_i^0 \tag{2.60}$$

$$\tau \equiv \sqrt{\gamma}\alpha^2 T^{00} - D \tag{2.61}$$

Here, $\alpha^2 T^{00}$ is just the Hamiltonian density ρ_H. In terms of these variables, equation 2.57 and 2.58 can be expressed as

$$\partial_t \mathbb{Q} + \partial_j \mathbb{F}^j = \mathbb{S} \tag{2.62}$$

where

$$\mathbb{Q} = \begin{bmatrix} D \\ S_i \\ \tau \end{bmatrix} \tag{2.63}$$

The flux vectors $\mathbb{F}$ are

$$\mathbb{F} = \begin{bmatrix} \gamma^{1/2} D v^i \\ \gamma^{1/2} \alpha T_j^i \\ \gamma^{1/2} \left(\alpha^2 T^{0i} - D v^i \right) \end{bmatrix} \tag{2.64}$$

where $v^i = u^i/u^t$ is the three velocity of fluid particles in the frame of the coordinate observer. Lastly, the source vectors $\mathbb{S}$ are given as

$$\mathbb{S} = \begin{bmatrix} 0 \\ \frac{1}{2}\alpha\gamma^{1/2} T^{ab} \partial_j g_{ab} \\ \alpha\gamma^{1/2} \left(T^{a0} \partial_a \alpha - {}^{(4)}\Gamma^0_{ab} T^{ab} \alpha \right) \end{bmatrix} \tag{2.65}$$

As the flow of fluid is affected by the geometry of spatial slices which are dynamically changing, these equations need to be solved iteratively along with BSSN equations. This is achieved by the method of lines which transforms the partial differential equation as an ordinary differential equation in time by integrating over space. To solve the resulting equations at any timestep t_i, the code first reconstructs the conservative variables from primitive variables (ρ_o, ϵ, v^i) and the source quantities $\mathbb{S}$. The computation of flux vector $\mathbb{F}$ requires solving the Riemann problem at each cell boundary where the center of each cell is a grid point. It is then possible to integrate equation 2.62 over time to obtain the conservative variables in the next time step which can be used to reconstruct primitive variables. While Whisky provides various methods for reconstruction, we adopt Piecewise Parabolic method [164] for our work based on the results in [163]. For solving Riemann problem, we use Marquina flux formula [165]. In present form, our code (including initial data and hydro code) only supports gamma law which primarily restrict our study to this equation of state. We note that more advanced hydrodynamics evolution codes have become publicly available with support for larger family of equation of states [155], [156].

2.6. Quasilocal Measurements

While the solutions of spacetime and hydrodynamical variables tell us about the changing geometry of spatial hypersurface and matter flow with time, they do not provide direct answers about the astrophysics of the system. But, these solutions are sufficient to construct the physical variables of interest. Here, we provide information about various tools used to track the properties of the system.

Tracking Black Hole and Neutron stars - To use the moving box mesh refinement method, we need to provide a tracker to follow each of the grid centers as the system evolves with time. We choose the grid centers to be at the center of each compact object (center of mass for a

star and puncture location for a black hole). The black holes are traced using equation 2.46 evaluated at the puncture which yields $\partial_t x^i_p = -\beta^i(x^i_p)$ [159]. For neutron stars, we track the center of mass of the star using VolumeIntegrals_GRMHD thorn [144] and separately with MinSearch thorn which searches for maximum density within a sphere of radius R.

Mass of Compact Objects - One of the quantities of interest are the masses of individual objects. For black holes, we use Apparent Horizon Finder thorn developed by Thornburg [166] which searches for marginally outer trapped surfaces (MOTS). The irreducible mass can then be determined from surface area $\mathcal{A}$ of the MOTS as $\sqrt{\mathcal{A}/16\pi}$. For neutron stars, we again use VolumeIntegrals thorn which integrates over density of a given spherical region to provide the rest mass of the stars. One of the limitations of this method is that the integration requires the assumption of the star being enclosed in a sphere which does not hold true close to its disruption as matter flows out of the region.

Rest Mass Outside the Horizon - To compute the rest mass outside the horizon, we use `VolumeIntegrals` thorn which integrates the rest mass density outside a sphere of radius r. As the sphere's radius cannot be changed during the evolution, we assume remnant black hole radius is less than $1.5M$. This mass also contains the mass of artificial atmosphere. Hence, the true mass outside the horizon is computed by removing the initial mass of the atmosphere at any point of time $\mathcal{M}_r(t) - \mathcal{M}_{atm}$ where $\mathcal{M}_r(t)$ is the rest mass outside the horizon at any time t and $\mathcal{M}_{atm}$ is the mass of artificial atmosphere at the initial time given by $\mathcal{M}_{atm} = \mathcal{M}_r(t=0) - \mathcal{M}_*$.

This is an approximate methods based on the assumption that the radius of the final black hole horizon can be treated as roughly constant during the merger and ringdown, the mass of artificial atmosphere does not change by a large proportion, the horizon size is constrained to be less than $1.5M$ and any matter within region of $1.5M$ outside the horizon does not contribute significantly to the accretion disk mass. As will be seen in the

follow up chapters, these methods yield good results for accretion disk mass for low mass ratios in comparison with previously published works though there are systematic effects at higher mass ratios due to the above assumptions. A more ideal way would use the surface of horizon from Apparent Horizon Finder as the region of integration to determine the matter content inside and outside the black hole. Further, to compute the mass of accretion disk and dynamical ejecta, we can follow the approach of [167, 168] to distinguish between the bound material and ejecta and use it to calculate mass of the accretion disk and ejecta.

Quasilocal Measures - Black hole in the perturbed state can carry additional moments of mass and spin. Schnetter et.al [144] developed QuasiLocalMeasures thorn which provides the functionality to measure these moments using the isolated and dynamical horizon formalism [145, 169]. These will be useful to understand how the horizon structure differs between binary black hole and neutron star black hole systems close to the merger.

2.7. GRAVITATIONAL RADIATION

One of the primary goals of numerical relativity is to model the gravitational wave signatures from different sources. In the wavezone, the spacetime can be treated as perturbations of Minkowski background and the metric can be written as $g_{ab} = \eta_{ab} + h_{ab}$ where h_{ab} are gravitational perturbations. Under the assumption of weak perturbations $|h| << 1$, Einstein's equations reduce to the wave equations given by

$$\nabla^c \nabla_c \hat{h}_{ab} = 0 \tag{2.66}$$

where

$$\hat{h}_{ab} \equiv h_{ab} - \eta_{ab} h^c_c / 2$$

Here, we have adopted Lorentz gauge condition $\partial_a \hat{h}^{ab} = 0$ and transverse traceless (TT) conditions $\hat{h}_{a0} = 0, \hat{h}^a_a = 0$ to fix the coordinate choice. This leaves us with two independent components of h_{ab} which in TT gauge can be written as $h^{TT}_{ij} = h_+ e^+_{ij} + h_\times e^\times_{ij}$ where $\mathbf{e}^+$ and $\mathbf{e}^\times$ are polarization tensors which in TT gauge take the form

$$\mathbf{e}^+ = \begin{pmatrix} 1 & 0 \\ 0 & -1 \end{pmatrix}, \qquad \mathbf{e}^\times = \begin{pmatrix} 0 & 1 \\ 1 & 0 \end{pmatrix} \tag{2.67}$$

To compute the gravitational wave strain, we adopt Newman-Penrose formalism [104]. In this method, Weyl curvature tensor can be expressed in form of five complex scalars by contracting it with suitably chosen null tetrad [170, 171] . Of particular interest among these is Ψ_4 defined as

$$\Psi_4 = -{}^{(4)}C_{abcd} k^a \bar{m}^b k^c \bar{m}^d \tag{2.68}$$

Here, C_{abcd} is the Weyl tensor, k^a and l^a are ingoing and outgoing null vector and $\bar{m}^a$ is a unit norm complex conjugate constructed from two spatial vectors orthogonal to null vectors k^a and l^a. In the radiation zone, as the spatial metric is asymptotically flat, hence under linear approximation and TT gauge, Riemann tensor is related with gravitational wave strain defined as $h = h_+ + \imath\, h_\times$. Exploiting this relationship, it can be shown that

$$\Psi_4 = \ddot{h}_+ - \imath \ddot{h}_\times \tag{2.69}$$

To compute Ψ_4, we use the WEYLSCAL4 module from Einstein Toolkit [162, 172] which evaluates this quantity at every gridpoint. To separate this gridfunction in different modes, Ψ_4 is projected on the spherical detector and expressed in terms of spin-weighted spherical harmonic basis functions as

$$\Psi_4 = \sum_l \sum_{m=-l}^{l} \Psi_4^{l\,m}\ {}^{-2}Y_{l\,m}(\theta, \phi) \tag{2.70}$$

For this, we use Maya thorn Ylm_Decomp which is analogous to Multipole thorn from Einstein Toolkit. With Ψ_4 in hand, it is possible to compute the strain h with simple time integration. However, this approach has shown to cause artificial non-linear drift of the waveform as shown by [173]. This is primarily due to integration of high frequency noise which does not average out to zero appearing as low frequency modes. An alternate approach would be to perform the integration in frequency domain using Fourier transforms. Though this works better than time integration, it still suffers from Gibbs phenomenon and spectral leakage due to finite length of the waveform [2]. To tackle this issue, we follow the Fixed Fourier Integration (FFI) method developed by Reisswig et.al. This method follows the Fourier integration method where each integration introduces a factor of $1/\omega$ in the signal. To tackle unphysical low frequency modes for artificial noise, it constraints the frequency factors in the denominator to have a minimum expected value for each gravitational wave mode.

2.7.1. RADIATED QUANTITIES

As the binary coalesces, a significant amount of energy and momentum is lost to the gravitational waves. From the conservation of ADM energy and momentum, measuring these quantities can provide us more details about the black hole kicks, mass of accretion disk, and spin of the final black hole. [174] came up with different methods to measure these quantities using Ψ_4 and gravitational wave strain h. Here, we adopt the following formula

[2] Due to presence of junk radiation, the initial part of Ψ_4 is contaminated and hence, needs to be removed. This abrupt start of the waveform can lead to Gibb's phenomenon. Though one can smooth out the waveform with windowing functions, the non-integral number cycles would lead to spectral leakage as signal will leak to the entire bandwidth.

for measuring these parameters -

$$\frac{dE}{dt} = \lim_{r\to\infty} \frac{r^2}{16\pi} \oint |\dot{h}|^2 \, d\Omega \tag{2.71}$$

$$\frac{dP_i}{dt} = \lim_{r\to\infty} \frac{r^2}{16\pi} \oint \ell_i \, |\dot{h}|^2 \, d\Omega \tag{2.72}$$

$$\frac{dJ_i}{dt} = -\lim_{r\to\infty} \frac{r^2}{16\pi} Re \left(\oint \hat{J}_i \, h \, \partial_t h^* \, d\Omega \right) \tag{2.73}$$

Here, ℓ^i is the direction vector, $\hat{J}_i$ are the angular momentum operators given by

$$\hat{J}_x = -\sin\phi \, \partial_\theta - \cos\phi \left(\cot\theta \, \partial_\phi - \iota \, s \csc\theta \right) \tag{2.74}$$

$$\hat{J}_y = \cos\phi \, \partial_\theta - \sin\phi \left(\cot\theta \, \partial_\phi - \iota \, s \csc\theta \right) \tag{2.75}$$

$$\hat{J}_z = \partial_\phi \tag{2.76}$$

Here, s is the spin weight which takes value 2 for h and -2 for h^*.

CHAPTER 3

MIXED BINARY SIMULATIONS - MASS RATIO COMPARISON

The coalescence of a neutron star black hole system has a strong dependence on the initial data. As discussed in chapter 1, two of the key parameters which can determine the fate of the neutron star are the mass ratio of the binary and the compactness of the neutron star. Depending on the initial mass ratio and stellar compactness, mixed binary systems can have a range of remnant states from a tidally disrupted star forming an accretion disk to a quiet isolated black hole. In the latter case, the system lacks a detectable electromagnetic signature which makes it harder to distinguish it from a black hole binary. This raises the questions - what is the difference between a binary black hole and a neutron star black hole signatures? For which NSBH mergers can we expect electromagnetic signals versus only gravitational waves? Are the current and future detectors capable to distinguish between a vacuum binary and a mixed binary?

In this work, we focus our attention on some of these questions using the tools of numerical relativity. Using the initial data formalism described in section 2.2, we present an independent study of mixed binary mergers to understand the differences between their dynamics and radiation signatures from a comparable black hole binary system. This chapter explores the effects of varying mass ratios on mixed binary mergers followed by a study on the compactness of the neutron star in the followup chapter. We also perform preliminary tests of our current simulations and perform comparisons with some of the well studied configurations in the works of [85] (including errata), [86], and [94] to showcase the efficiency of our results. Primary reason to choose these works is due to the similarity

in the equation of state models. We note that the NR codes are independent and differ in the initial data, spacetime and hydrodynamical evolution methods. Hereafter, these are referred as ST-P1, ES-P1, and ES-P2.

In the next sections, we will discuss the simulation setup, convergence results, and merger dynamics. Section 3.1 provides a description of the initial configuration for the three cases with a brief summary of numerical infrastructure and grid setup used in the simulations. This is followed by a resolution study and convergence test in section 3.2. We then explore the dynamics of the mixed binary and the effects of mass ratio on the source and remnant properties, gravitational wave signatures and radiated quantities in section 3.3. We will also discuss the differences between these systems and binary black holes with similar mass ratios.

Units - In this work, we will primarily use the geometrical units in which the speed of light, c, and Newton's gravitational constant, G, are set to 1. All dimensional quantities are expressed in terms of total mass M but we also provide measures in terms of physical units where necessary. As an exception to this rule, we will make a temporary shift to polytropic units in section 3.1 for ease of comparison with other works.

Reference and Contribution - This chapter is author's original work performed in collaboration with Dr. Miguel Gracia and Prof. Pablo Laguna. The work was recently submitted to CQG [175] with some updates.

3.1. Initial Parameters and Numerical Setup -

Initial Configuration - We consider three different configurations of mixed binaries with mass ratio 2, 3 and 5, where the mass ratio q is defined as the ratio of ADM masses of the black hole and neutron star in isolation. This is primarily inspired from a binary black hole

system. The total mass of the system is chosen to be $(1+q) \times \mathcal{M}_S$ where $\mathcal{M}_S = 1.35 M_\odot$ is the desired mass of the neutron star when part of the binary. To construct the initial data, we find the central density ρ_c of an isolated TOV star whose ADM mass $\mathcal{M}_A = \mathcal{M}_S$ and compactness of $C = \mathcal{M}_A / R_S = 0.145$ where R_S is the Schwarzschild radius of the star. The neutron star is modeled with polytropic equation of state with $\Gamma = 2$ while polytropic constant $K = 51.38/(1+q)^2 \ M^2$ (or 93.65 $M_\odot^2$). The black hole has a desired mass of $\mathcal{M}_h = q\,\mathcal{M}_S$ and is non-spinning for all the three cases. The binary separation is chosen to be $9M$ where M is the total mass of each system. Assuming the dynamics can be well described using post-Newtonian (PN) theory at such large separations, we compute the linear momentum for each object by solving 3.5 PN equations of motion. Using ρ_g and $\mathcal{M}_h$ as the initial guesses of TOV central density and puncture mass, we construct the initial data using the method described in chapter 2. Table 3.1 provides further details about the initial configurations for each case at the completion of Broyden iterations. For ease of comparison, we have presented the variables in polytropic units (denoted by $\bar{}$) as followed in other works. Note that our configurations closely mimic models $M20.145$, $M30.145$, and $M50.145$ in ST-P1 (check table I), models B and $A1$ in ES-P1, and models A and D in ES-P2.

Numerical Methods - Using this setup, we can now apply the initial data approach described in reference [143] (see section 2.2 for details) to find the solution for spatial metric and curvature, gauge and hydrodynamical variables. The system is evolved with `MAYA` code [143, 176, 177], a local version of Einstein Toolkit [144, 162, 172], using BSSN-Chi formulation [135, 136, 178] with IV order finite differencing stencil. We use "1+log"slicing with gamma driver shift condition to determine the gauge functions [159, 160]. The constraints are not solved separately but its violations are constantly monitored. The hydrodynamical variables are evolved using Whisky public code [163, 179, 180]. For this work, we use Marquina Riemann solver [181] and Piecewise Parabolic reconstruction method (PPM) [182].

TABLE 3.1: Initial configuration of mixed binary in polytropic units. q refers to the mass ratio, C is the compactness of isolated TOV, $\bar{D}$ is the initial separation, $\bar{\mathcal{M}}_h$ is Christodoulou Mass of black hole, $\bar{\mathcal{M}}_A$ is the ADM mass of isolated TOV, $\bar{\mathcal{M}}_o$ is the rest mass of isolated TOV, $\bar{\rho}_{max}$ refers to the central density of the star in binary at the initial time and $M\Omega$ is the initial orbital frequency (from PN).

Parameters	**Model 1**	**Model 2**	**Model 3**
Name	$q2$	$q3$	$q5$
q	2	3	5
C	0.1529	0.1536	0.1543
$\bar{D}$	3.766	5.022	7.533
$\bar{\mathcal{M}}_h$	0.279	0.4185	0.697
$\bar{\mathcal{M}}_A$	0.1436	0.1439	0.1543
$\bar{\mathcal{M}}_o$	0.1549	0.1553	0.1557
$\bar{\rho}_{max}$	0.1381	0.1391	0.1401
$M\Omega_0$	0.0319	0.0318	0.0318

In order to find the black hole, we track the puncture location [159] and also independently search the horizon using `Apparent Horizon Finder` thorn developed by Thornburg et al. [166]. The star is tracked using two separate methods - first by using `MinSearch` thorn of `MAYA` which finds the maximum of central density and second using the `VolumeIntegrals` thorn developed by Etienne et al. [144] which follows the center of mass of the star. The remnant black hole properties including mass, spins and multipole moments are computed using `QuasiLocalMeasures` thorn by Schnetter et al. [144, 162]. The rest mass of matter is calculated using `VolumeIntegrals` thorn. The gravitational wave strain is computed using Ψ_4 which is measured with WEYLSCAL4 module [144] followed by FFI method illustrated in [173]. To compute the radiated quantities, we follow the method developed in [174] by integrating Ψ_4.

Grid Structure - We use the moving box mesh refinement approach with cell centered Cartesian grid structure using `Carpet` adaptive mesh refinement driver [183]. Black hole

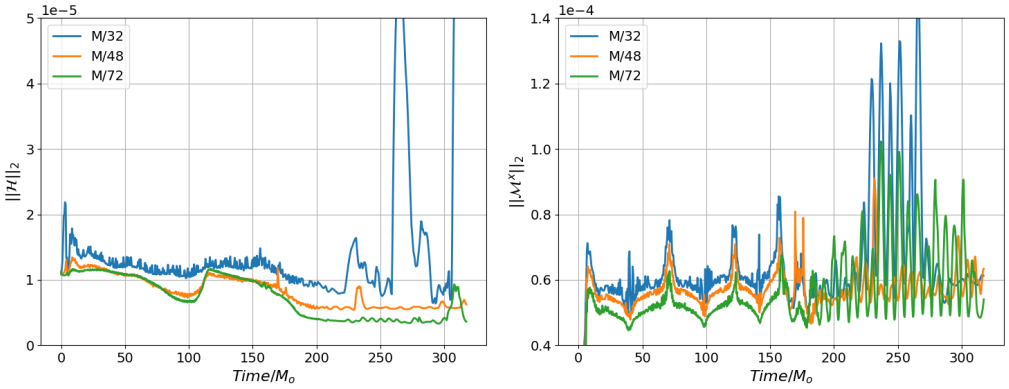

FIGURE 3.1: 2-norm of Hamiltonian and Momentum Constraints for mass ratio 2 NSBH with separation of 7M. Blue, orange and green denote three different resolution runs with 64^3 (low), 96^3 (medium) and 144^3 (high) points on finest refinement level.

and neutron stars are placed on x axis at a separation of $9M$ s.t. center of mass location coincides with the origin. Two grid centers are chosen as the location of puncture and center of neutron star (denoted by $\mathcal{O}_{BH}$, $\mathcal{O}_{NS}$). For mass ratio $q \leq 3$ ($q > 3$), the star is covered with 7 (8) refinement levels each centered at $\mathcal{O}_{NS}$. The smallest box has the side length of $L_f^{NS} = 2.4 * R_{NS}$ which is slightly larger than the stellar diameter to account for radial oscillations. The grid spacing is chosen s.t. stellar radius is covered by 50 points which translates to $\delta x = 225m$ in SI units. For every subsequent level, the length is increased by a factor of two except the last third grid levels where the length is increased by a factor of four to ensure proper grid resolution at detectors. The grid spacing is uniformly increased by a factor of two. The same grid structure is also retained for black hole with one or two additional finer levels s.t. the black hole diameter is covered by at least 50 points. Lastly, we add another grid center at the origin with the outermost refinement box which remains fixed for all three cases. Exploiting the reflection symmetry about x-y plane helps in reducing the number of grid points, which drastically cuts the computation time by a factor of two.

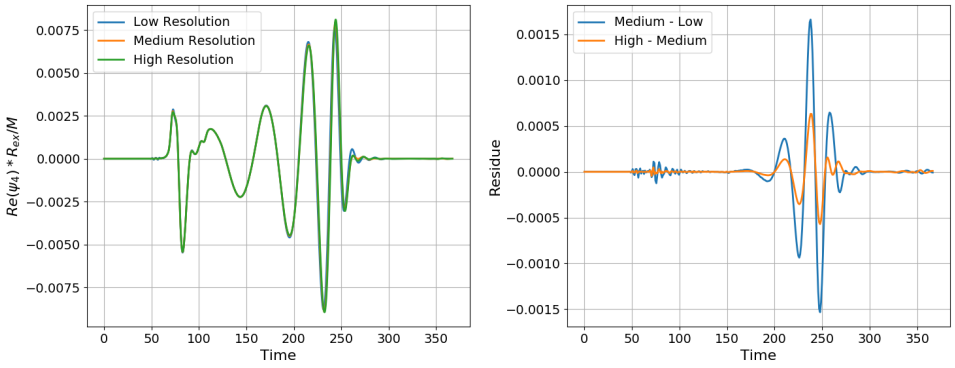

FIGURE 3.2: Convergence test with $Re\left(\Psi_4^{22}\right)$. Panel on the right shows the residues between low ($M/32$), medium ($M/48$) and high ($M/72$) resolution.

3.2. CONVERGENCE STUDY -

Discretization of differential equations results in truncation errors due to approximation of derivatives using finite difference methods. The accuracy of the resulting solution depends on the order of the stencil and the resolution of the grid structure. For any grid-dependent numerical solution $\tilde{f}$ obtained with k order of accuracy [184],

$$\tilde{f} = f + C_0(\delta x)^k + \mathcal{O}\left((\delta x)^{k+1}\right) \tag{3.1}$$

Here, f is the true solution of the continuum equations and C_0 is some constant. For most common grid functions the true solution is not known apriori, and hence to determine k, we can choose three different resolutions δx_l, $\delta x_m = \delta x_l/\theta$, and $\delta x_h = \delta x_l/\theta^2$ in equation 3.1 where θ is a resolution factor. Solving for k we have,

$$k = \log_\theta\left(\frac{\tilde{f}_l - \tilde{f}_m}{\tilde{f}_m - \tilde{f}_h}\right) \tag{3.2}$$

To test the convergence with our new infrastructure, we perform mass ratio $q = 2$ simulations at a separation of $7M$ and compare Ψ_4 and constraint violations. For the lowest

resolution run ($M/32$), we select $\delta x_l \sim 1.2 * R_{NS}/36$ on the smallest refinement level on the star while δx_m ($M/48$) and δx_h ($M/72$) are chosen with scaling factor of $\theta = 1.5$. Additional refinement levels are added for the black hole due to its smaller size. The grid structure is setup as previously described and the same numerical methods are used for the evolution. Figure 3.1 shows the behavior of 2-norm of Hamiltonian and momentum constraints for three resolutions. The constraints are well behaved through the entire evolution and improve with higher resolution. The increase in constraint violation post merger occurs inside the black hole near the puncture and will not affect the dynamics outside the horizon, which can be seen from the constraint heat maps in the x-y plane. Since the constraints are not solved during evolution, the extremely small violations in the constraints serve as a good check on the consistency of our solution. Figure 3.2 shows the convergence of the real part of Ψ_4^{22} for the three cases. The results for the three simulations overlap quite well with each other with residues decreasing with resolution. Using the equation 3.2, we find that the convergence factor for Ψ_4^{22} is $k \approx 2.37$.

3.3. RESULTS -

3.3.1. ORBITAL DYNAMICS

From the work of Schnetter et al. [145], it has been known that black holes tend to behave similar to isolated horizons throughout the inspiral regime. The strong self gravitational fields of these objects make them immune to tidal distortions [185]. In contrast, the effects of these forces can be dominating on a neutron star which in certain cases can result in its complete disruption. Thus, there exist fundamental differences between a mixed binary and binary black hole merger which can be studied using numerical relativity simulations.

Figure 3.3 shows the evolution of the orbital separation for NSBH and BBH binaries. The longer merger times of higher mass ratio binary systems in this figure can be explained from the post-Newtonian theory. For compact binary systems, the luminosity and rate of

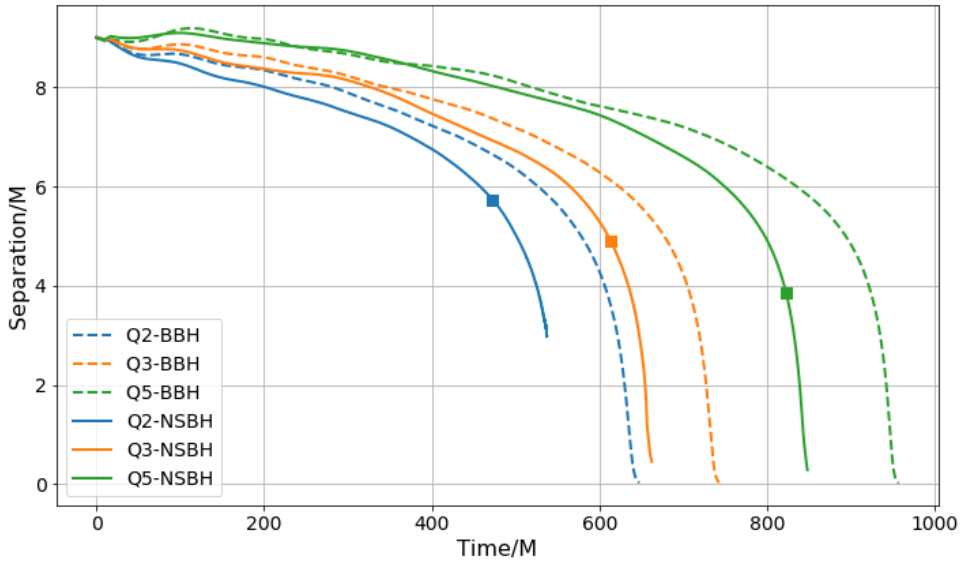

FIGURE 3.3: Orbital Separation Evolution for NSBH and BBH systems. The solid and dotted lines represent NSBH and BBH systems while colors specify the mass ratio. Boxes represent the tidal radius.

change of radiated angular momentum of gravitational radiation depends on the mass ratio of the binary as $q^2/(1+q)^4$ for fixed separation [104]. As a result, higher mass ratio systems dissipate energy and angular momenta at a slower rate. Comparing the separation curves of NSBH with BBH systems, we find larger deviations in orbital separation for $q = 2$ case from early inspiral. As mass ratio increases, NSBH resembles closer to the vacuum binary case. This is also easily visible from the number of orbits and merger time in the table 3.2. One can intuitively understand this by looking at the tidal radius [104, Eq. 17.19]) and the ISCO radius -

$$r_{tid} \simeq 2.4 q^{1/3} R_S \tag{3.3}$$

$$r_{ISCO} = 6\, M_h \tag{3.4}$$

For mass ratio $q = 2$ case, the tidal radius is around $6.6M$ (or $\sim 39km$) which is

TABLE 3.2: Merger Statistics Comparison - Here q is the mass ratio, System represents type of compact binary, N is number of orbits, e is eccentricity, T_{Merger} is the time of merger (retarded time corresponding to peak of Ψ_4), Δ_{Merger} is black hole offset from origin at T_{Merger}, and v^f_{BH} is the coordinate velocity of the remnant black hole at T_{Merger}.

q	System	N	$e \times 10^{-3}$	T_{Merger}	Δ_{Merger}	v^f_{BH}
2	BBH	5.67	6.3	648	0.027	0.006
2	NSBH	3.84	6.8	537	0.746	0.082
3	BBH	6.11	5.5	743	0.058	0.006
3	NSBH	5.05	8.3	662	0.782	0.031
5	BBH	7.32	10.5	957	0.037	0.002
5	NSBH	6.33	9	848	1.03	0.024

larger than the ISCO radius of $4M$ (or $24km$). As a result, mass shedding occurs at significantly early duration after $440M$ of evolution. At this point, tidal forces completely overpower the star's gravity which marks the beginning of its disruption phase ($\sim 96M$ before merger) as shown in panel (a) of Figure 3.4. This is indicated by the change of velocity field direction within the star. The star loses its structure deforming into a spiral arm around the black hole which extends to $10M$ from the origin (panel (b)). About 90% of the material falls into the black hole within first $100M$ while the remaining material continues to expand outwards slowly morphing into an accretion disk. About 500M after the merger, the accretion disk continues to evolve to final densities $10^{-4}\, M^{-2}$ ($10^{12}\mathrm{g/cm}^3$). The situation is completely different in a BBH case where tidal forces have no visible impact on the secondary black hole, as a result of which the binary continues to evolve for a longer duration which explains the differences between the orbital trajectories and the merger times of the two systems.

The dynamics of mass ratio 3 follows a very similar path as mass ratio 2, however, the disruption occurs very close to ISCO in this case as shown in figure 3.5. As a result, more than 95% of the star is consumed by the black hole at the merger, leaving lower density material for the disk formation. Due to the larger gravitational field of the black hole and

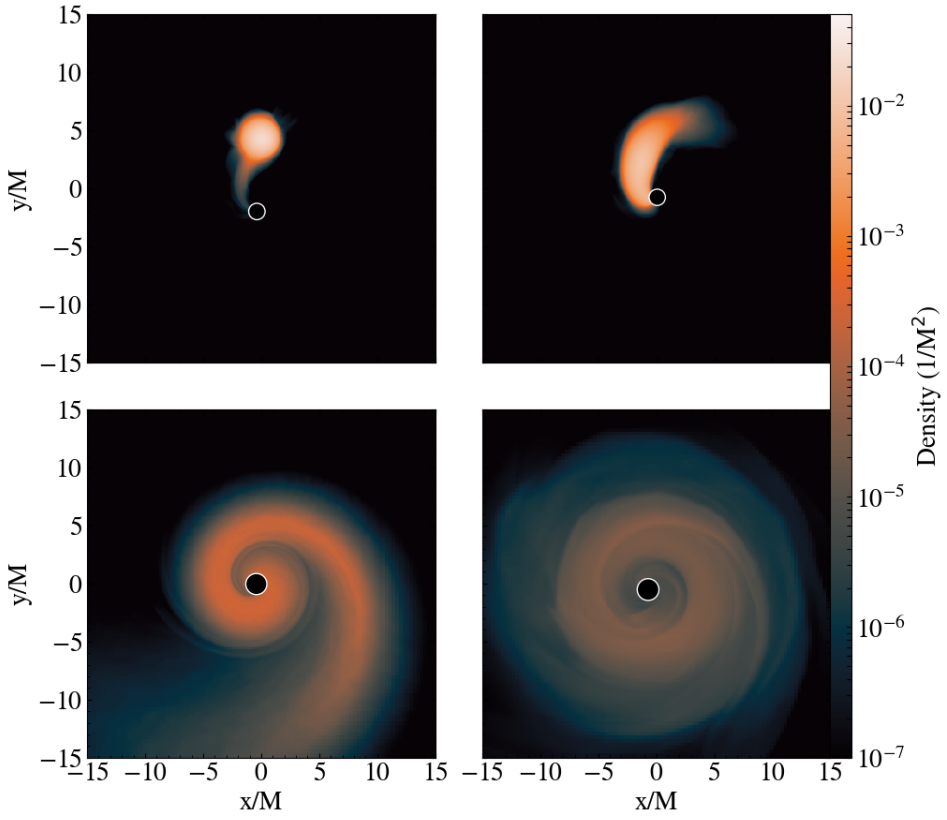

FIGURE 3.4: Contour plots of rest mass density for $q = 2$. Black hole is represented by black circle with white boundary. The initial central density of star is close to $0.14/M^2$ ($9.1 \times 10^{14} g/cm^3$). From top left, panel (1) shows the beginning of mass dissipation about 96 M before the merger. Panel (2) shows the stellar disruption at the time of merger. Panel (3) represents the circularization stage of matter around the black hole about 100M after the merger and panel (4) shows the final state of accretion disk 500M after the merger.

reduced angular momentum transport, most of the matter is gravitationally bound and is quickly accreted on the black hole leaving a tenuous accretion disk behind with densities $\sim 10^{-6} M^{-2} (10^{10} g/cm^3)$.

The merger of mass ratio 5 system is in complete contrast to the above scenarios. With the increase in BH mass, ISCO orbit grows at much higher rate in comparison to the tidal radius. For a compactness of $C \sim 0.15$, r_{ISCO} exceeds r_{tid} for $q \gtrsim 4.3$. Thus, for mass ratio 5

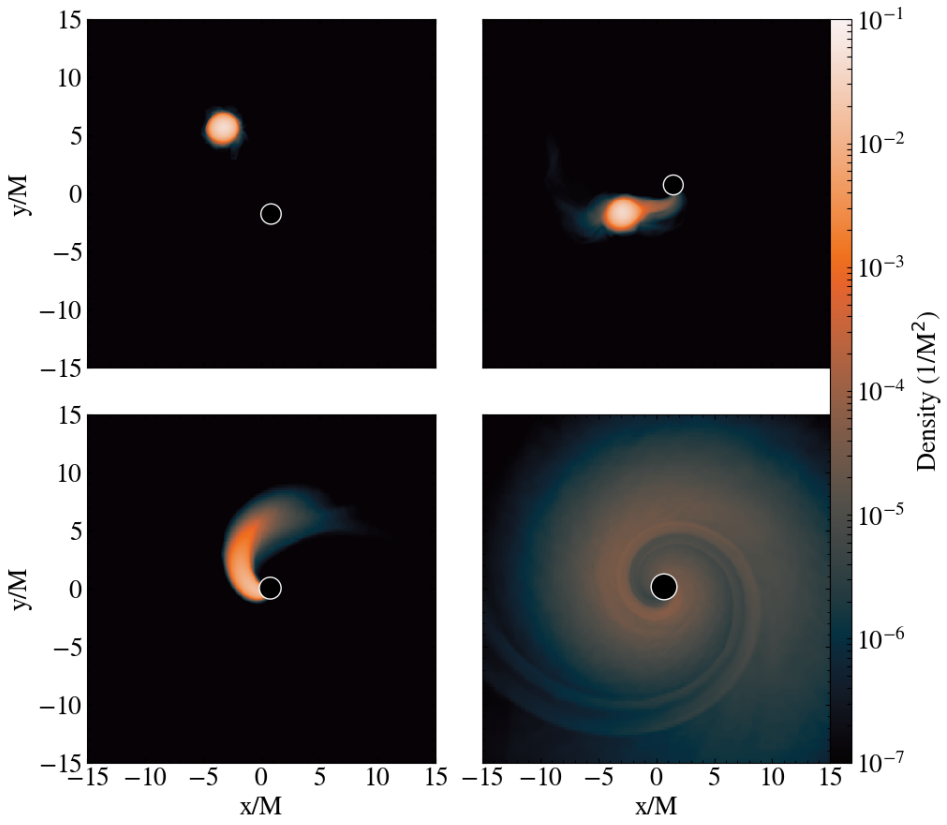

FIGURE 3.5: Contour plots of rest mass density for $q = 3$. Panel (1) shows the tail formation at 78M before the merger which leads to partial disruption of star as shown in the panel (2) at the time of merger. Panel (3) shows the circularization phase 30M after the merger. Panel (4) depicts a low density accretion disk 500M after merger.

case, star remains almost intact by the time it reaches ISCO radius of $\sim 5M$ ($\sim 60km$). As a result, the beginning of disruption occurs only $45M$ prior to the merger as can be seen in panel 1 of figure 3.6. Before the star can be completely disrupted, 99% of the stellar core has already fallen into the black hole within the first $20M$ of the merger which is followed by a rapid accretion of almost all the remaining material within $100M$ after the merger. This leaves a vacuum-like remnant state with extremely low atmospheric densities without any electromagnetic signature, which makes it almost indistinguishable from a BBH. Similar

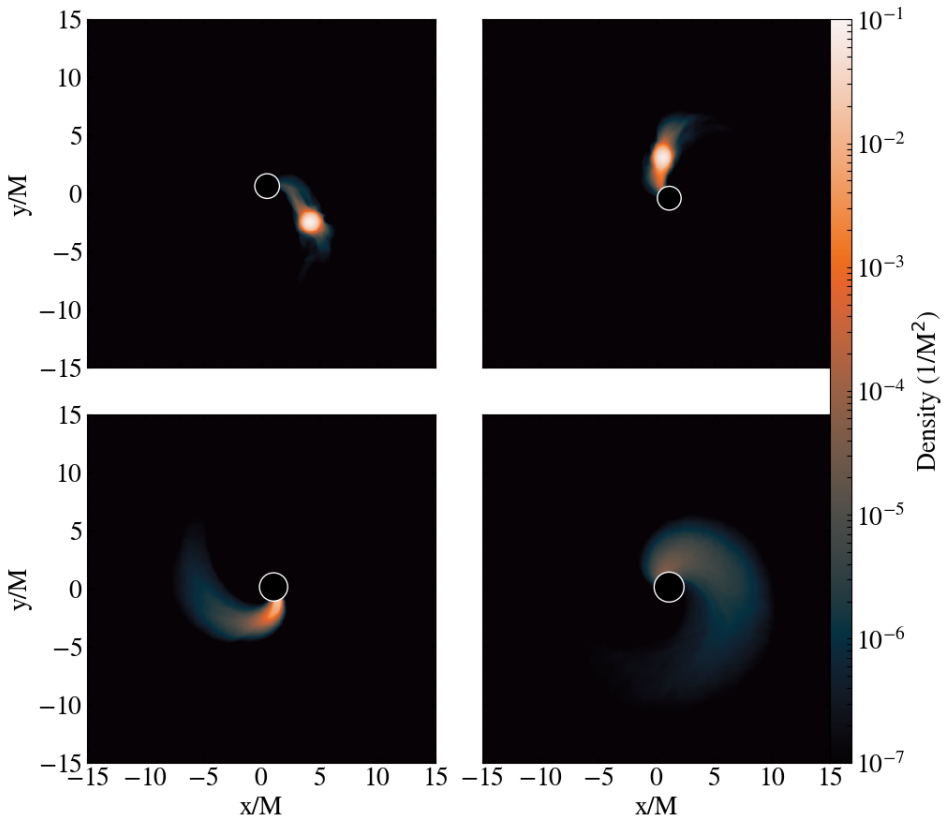

FIGURE 3.6: Rest mass density contour plots for $q = 5$. Labeling scheme remain same as 3.4. Panel (1) shows the stellar structure 45M before merger while Panel (2) corresponds to merger. Most of the stellar material is already fallen into star with a very weak tail like structure. This leftover material is quickly absorbed by the black hole within 50M after the merger (panel 3) and hardly any material is left roughly 500M after the simulation (panel 4).

results were also reported in ST-P1, ES-P1, and ES-P2.

3.3.2. QUASILOCAL QUANTITIES

Stellar Mass - For all the three mass ratios, the stellar mass remains fairly stable throughout the inspiral. Fluctuations in the central density (discussed further in section 3.3.4) introduce small variations in the stellar mass with errors of about 1% with respect to the the initial value. During the inspiral regime, small amounts of material with densities

TABLE 3.3: Quasilocal Properties Comarison - Here q is the mass ratio, System Type represents type of compact binary, $M_I^{(R)}$ is irreducible mass of remnant black hole, $M_h^{(R)}$ is horizon mass of remnant, $M_{r>r_{BH}}$ is the rest mass of matter outside BH, $a^{(R)}$ is the dimensionless spin of the remnant, and τ_{22} and $f_{22}^{\rm qnm}$ are the damping time scale and quasinormal frequencies for (2,2) mode based on the accuracy of linear fits.

q	**System**	$M_I^{(R)}$	$M_h^{(R)}$	$M_{r>r_{AH}}/M_0$	$a^{(R)}$	τ_{22}	$f_{22}^{\rm qnm}$
2	BBH	0.9073	0.9598		0.617	11.6244	0.0831
2	NSBH	0.8984	0.9658	0.0192	0.683	9.4548	0.0883
3	BBH	0.9319	0.9712		0.5405	11.4404	0.0779
3	NSBH	0.9308	0.974	0.0113	0.563	11.3218	0.0783
5	BBH	0.9598	0.9823		0.4166	11.2875	0.0719
5	NSBH	0.9603	0.9834	0.0024	0.4203	11.0844	0.0715

$\rho < 10^{-5}\rho_{max}^{NS}$ dissipates into the atmosphere some of which gets absorbed by the black hole while remaining ejecta escapes the system. The mass of the dynamical ejecta is found to be almost negligible ($10^{-4}M$) during this period. As the star reaches closer to the black hole, the star's self gravity becomes weaker in comparison to the tidal force of the black hole which marks the beginning of its disruption phase.

BH Mass and Spins - The growth of black hole mass and spin is directly related to the extent of stellar disruption in a mixed binary system. The left panels of figure 3.7 show a comparison of the irreducible mass and spin of the black hole in NSBH cases, while panels on the right show their rates. Dashed lines represent the remnant black hole mass and spin in corresponding BBH cases. For $q = 2$, the black hole has an extended period of growth till the end of the simulation, reaching the peak growth rate after the "merger" [1]. This is in sharp contrast to the BBH case where the remnant black hole mass and spin increase

[1] In a vacuum binary, the merger is marked by a sudden appearance of common horizon of the remnant encapsulating the initial binary as marginally outer trapped surfaces. The appearance of this surface is followed by peak of Ψ_4 in the retarded time domain. In contrast, the merger time in mixed binary systems is not well defined. Here, the stellar material is absorbed by the black hole continuously over a course of time. As a result, in this work, we define the "merger" time in mixed binary as the retarded time corresponding to the peak of $(2,2)$ mode of Ψ_4.

almost instantaneously and the maximum growth rate appears before the peak of Ψ_4 in retarded time. The smaller mass and spins in the NSBH case at the time of merger is due to the presence of an additional dissipation channel in form of matter outflow which also carries away energy and angular momentum from the system along with gravitational waves. However, unlike gravitational waves, most of the matter remains bound to the black hole and falls back leading to an increase in its mass and spin. The dissipation in matter channel decreases with lower degree of tidal disruption leading to a more BBH like behavior in NSBH systmes. This is reflected in the mass ratio 3 NSBH case where the mass and spin growth rates peak before the merger. However, the black hole continues to grow for a long period due to matter accretion. The growth of the black hole is highly accelerated for mass ratio 5 mimicking close to BBH case as seen in figure 3.7. The final BH absorbs 99% of stellar material within just 20 M of evolution time and the mass and spin become almost constant.

Table 3.3 compares the mass of the final black hole between BBH and NSBH cases for different mass ratios. It can be seen that for non-spinning mixed binaries, the black hole mass is significantly closer to the BBH case with less than 1% difference in the final values. Comparison with SH-P1 and ES-P1 shows agreement in the results with errors of $\sim 0.5\%$. The net change in black hole mass is smaller than the rest mass of the star, similar to the BBH case (with secondary black hole). This additional energy from the neutron star dissipates into the radiated gravitational waves, accretion disk, and dynamical ejecta. In contrast to mass, the spin of the remnant hole is significantly higher in mixed binaries compared to BBH cases, with differences ranging from $1\% - 10\%$. Due to the disruption of the star, the radiated angular momentum in gravitational waves is significantly reduced and is distributed between the accretion disk and remnant black hole. In addition, the infalling material from the accretion disk further enhances the black hole spin in disruption scenarios. Again, our results for spins are in good agreement with reference studies of Shibata et al. and Etienne et al. within errors of $< 0.5\%$.

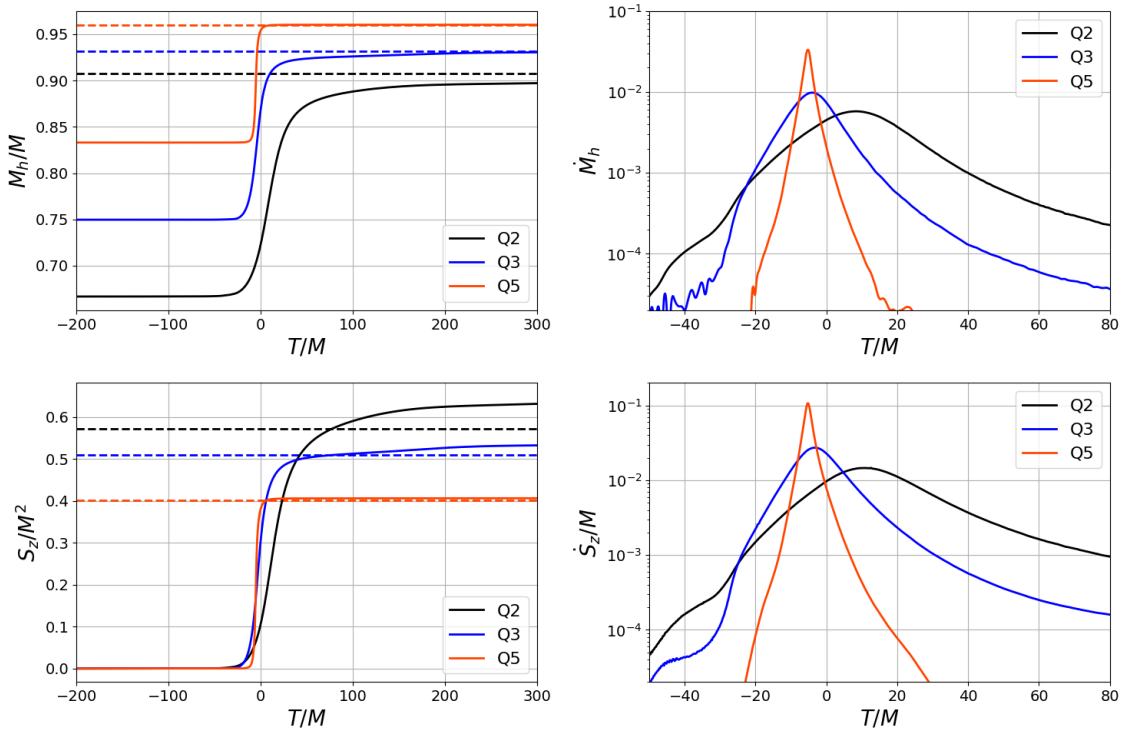

FIGURE 3.7: Change in black hole mass and spin near the merger. Panels on the left show the change in irreducible mass and z-component of spin from the initial value while panels on the right show their rates. Time is centered at the peak of ψ_4 in retarded frame

Rest Mass Outside the Horizon - From the rest mass density contour plots in figures 3.4 and 3.6, we saw that tidal disruption of the star can lead to the formation of an accretion disk for low mass ratio binaries. However, formation and evolution of these disks can vary significantly across the mass ratio. To understand their evolution, we evolved the remnant around $500M$ after the merger for each mixed binary system and tracked the mass of matter outside the horizon using `VolumeIntegrals` thorn as explained in 2.6.

Figure 3.8 shows a comparison of fractional mass outside BH horizon for mass ratio $q = 2, 3, 5$. The mass outside the black hole is extremely small in all three cases and decreases as the black hole mass is increased. For mass ratio $q = 2$, 90% of stellar mass falls

into the black hole within first $100M$ of the merger which is followed by a slow accretion process. As the disk evolves, matter continues to accrete on the black hole leaving behind $0.052\mathcal{M}_o$ or $0.078M_\odot$ of matter outside the horizon after $500M$ of merger. The corresponding value predicted by SH-P1 is roughly $0.06M_o$.

Mass ratio $q = 3$ follows similar trail as $q = 2$ case, although the dynamics of disk evolution varies between the two. During the first $100M$ of evolution, black hole has already consumed 94% of stellar material and we are left with extremely low density accretion disk which is continuously getting devoured by the black hole. By the end of the merger, the rest mass of remaining material outside the black hole is reduced to 3.1% of $\mathcal{M}_o$. SH-P1 predicts these values to be 4.7% of $\mathcal{M}_o$ while ES-P2 predicts 3.9% of $\mathcal{M}_o$.

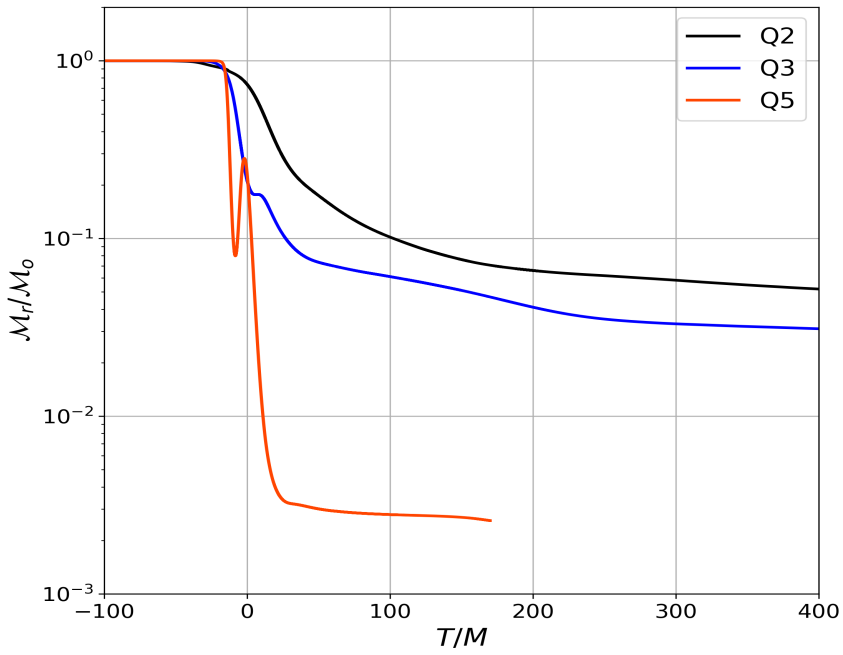

FIGURE 3.8: Rest mass outside the black hole scaled with initial rest mass of star.

Dynamics of $q = 5$ is significantly different with only partial disruption of star towards

the end of inspiral. As a result, 99% of star is already devoured by the black hole in first $20M$ of merger, barely leaving any material to form a disk. The remaining material either falls into the black hole or escapes as a dynamical ejecta with no accretion disk at the end of the merger. The sudden increase followed by a sharp fall in the mass of disk outside at $t = 0$ is due to the use of fixed radius spheres as an approximation for horizon. At the time of merger, horizon radius is still smaller than $1.5M$ and hence, some matter is able to flow out which leads to sudden increase in the mass. The mass of matter outside the black hole in this case is about $0.0025\mathcal{M}_0$ or $3.4 \times 10^{-3} M_\odot$. The mass found by SH-P1 in this case is $4 \times 10^{-4} \mathcal{M}_o$ and by ES-P2 is $8 \times 10^{-3} \mathcal{M}_o$.

Due to higher atmospheric densities, lower finite differencing order, and approximation on the horizon radius, our results are typically lower than SH-P1 or ES-P2. We note that the errors between SH-P1 and ES-P2 is also quite large for the highest mass ratio case. For better results, we need more accurate methods to compute the mass of matter.

3.3.3. GRAVITATIONAL WAVES -

While most of the above comparisons are based on the local measurements of the system, in reality, such measurements are not directly possible. Fortunately, the dynamics of these system leave their imprint on the spacetime perturbations which can be observed in our detectors as gravitational wave signatures.

In figure 3.9, we show the real part of (2,2) mode of Ψ_4 for mixed binaries and vacuum binaries. The solid lines show NSBH signals while dashed lines correspond to BBH. Plots in the inset show the overlap between the two signals during the inspiral phase. We observe that the merger times are smaller for NSBH systems compared to BBH while the gravitational waves are emitted for longer duration for the higher mass ratio case. This can be explained using post-Newtonian theory according to which the orbital decay acceleration depends on the tidal deformability of the system and hence, will decay faster for mixed binary systems due to non-zero tidal deformability [186]. As a result, NSBH systems

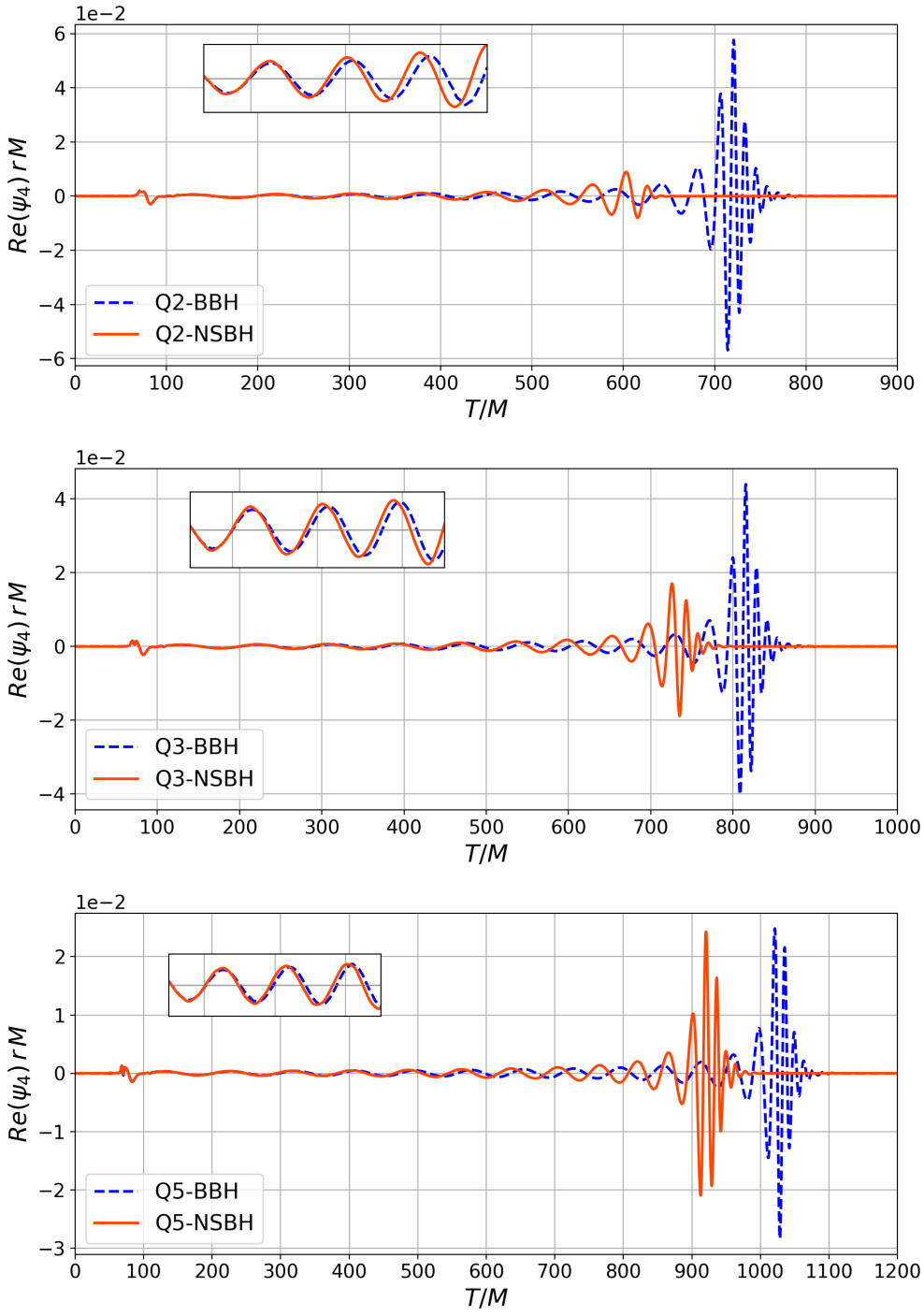

FIGURE 3.9: Comparison of (2,2) mode $Re(\Psi_4)$ between BBH and NSBH systems across the mass ratio. Panels from top to bottom correspond to mass ratio 2, 3, and 5 case. Figure in the inset show the initial few cycles. From the inset figures, we find larger match between NSBH and BBH waveforms for $q = 5$ compared to $q = 2$

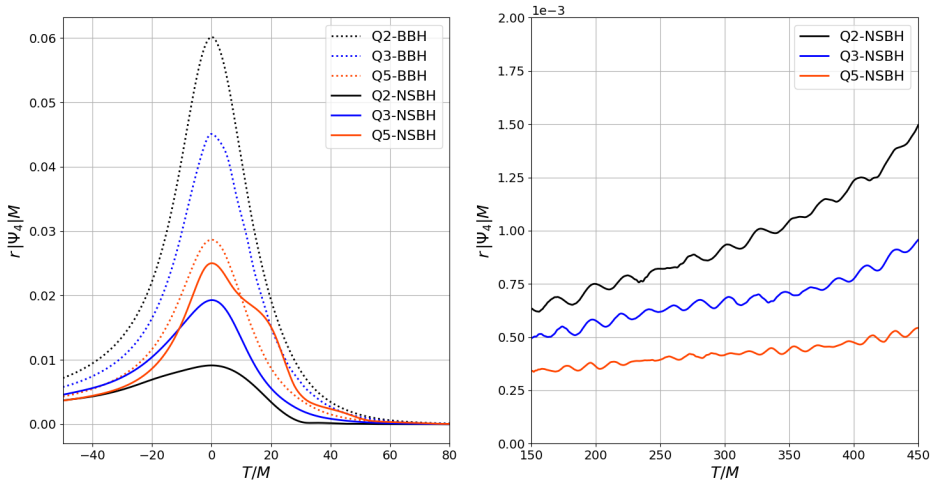

FIGURE 3.10: Comparison of $|\Psi_4|$ between BBH and NSBH systems across the mass ratio. While the amplitude of BBH systems decrease with increasing mass ratio, reverse trend is observed for mixed binary.

will emit gravitational waves at a faster rate leading to early mergers. As the mass ratio increases, the two systems behave more alike with better overlaps. The left panel of figure 3.10 shows the Ψ_4 amplitude of (2,2) mode during the late inspiral to ringdown phase. The amplitude for BBH systems is the highest for $q = 2$ binary and tends to decrease as the mass ratio increase. This is consistent with post-Newtonian theory according to which the luminosity of the gravitational wave depends on the mass ratio as $q^2/(1+q)^4$. In contrast, the growth of the amplitude shows an inverse trend in NSBH systems as a function of mass ratio. For low mass ratio mixed binaries, the neutron star is completely disrupted before the merger which reduces the net quadrupole moment of the system. As the mass ratio increases, a bulk of the stellar mass falls into the black hole at the merger over a narrow region of horizon surface, generating stronger deformations. This increases the quadrupole moment of the system leading to larger amplitudes of Ψ_4.

The continuous perturbations of the horizon structure in low mass ratio mixed binaries

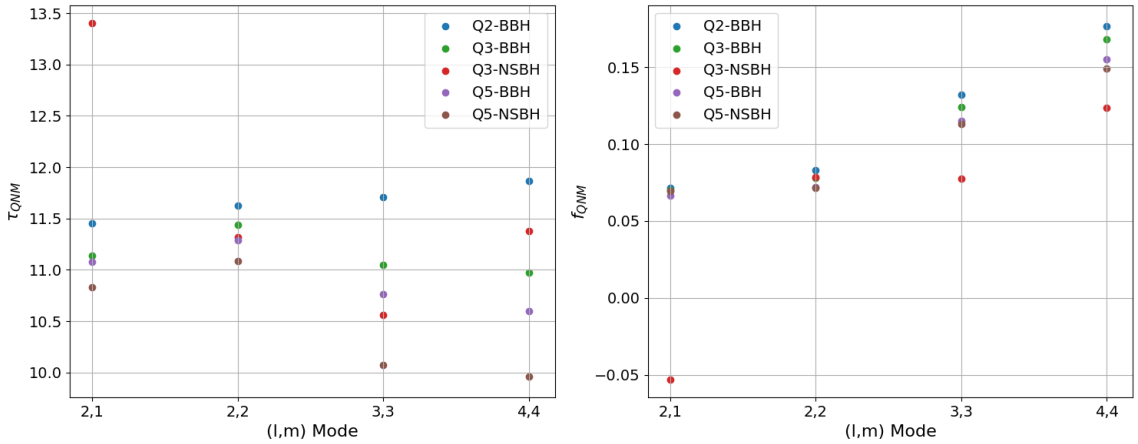

FIGURE 3.11: Damping Time Scale and QNM frequency

affect the ringdown signals. Uniform influx of material from the disrupted star weakly excite a combination of quasinormal modes barely providing the black hole time to relax. To understand the effects of tidal disruption on the ringdown phase, we look at the first three dominant modes - (2,1), (2,2), and (3,3) after merger. Ringdown signals can be modelled as

$$A_0 e^{-t/\tau_{lm}} \sin(\omega_{lm}^{\text{qnm}} t + \phi_0) \tag{3.5}$$

where τ_{lm} is the damping time scale for (l, m) mode and $\omega_{lm}^{\text{qnm}} = 2\pi f_{lm}^{\text{qnm}}$, f_{lm}^{qnm} is the quasinormal frequency. Figure 3.12 shows the post merger signals of NSBH for the three modes in amplitude (left panels) and phase (right panels). The linear fits, shown in sold lines, are obtained from the ringdown studies of Kerr black hole [187]. As seen from the amplitude and phase plots, the fits in the sold lines do not align well with the data (dashed lines) for $q = 2$ mixed binary system. Thus, ringdown signatures are absent in this case due to unsettled black hole horizon. For $q = 3$, while the most dominant mode is decaying exponentially in amplitude, other modes show significant deviations from this behavior. Mass ratio 5 has a better behavior with ringdown signals present in all the modes. The oscillations in the amplitude is a systematic effect in this case due to the COM offset and

not due to matter accretion. These observations lead to two important inferences - first, the ringdown signatures are affected by the initial configuration due to the differences in the remnant state. And second, higher modes play an important role to differentiate NSBH from BBH systems even for high mass ratio binaries. It should be noted that most higher modes are strongly impacted by numerical noise which makes it difficult to distinguish between numerical artifacts vs perturbation effects. In table 3.3, we report the values of $f_{lm}^{\rm qnm}$ and τ_{lm} for $(2,2)$ mode while figure 3.11 show the variation in damping time scales and quasinormal frequencies across the modes. The values agree quite well with those predicted by SH-P1. Note of caution - these values are based on the accuracy of linear fits which are not a good representation of data for low mass ratio mixed binaries.

Strain - Following SH-P1, we define the Fourier spectrum of gravitational waves for $l = |m| = 2$ mode as

$$\tilde{h}(f) = \sqrt{\frac{|\tilde{h}_+(f)|^2 + |\tilde{h}_\times(f)|^2}{2}} \tag{3.6}$$

where $\tilde{h}_+(f)$ and $\tilde{h}_\times(f)$ are the Fourier transforms of plus and cross polarization of strain as defined in equation 2.69. Figure 3.13 shows the Fourier spectrum for the BBH and NSBH cases for all three mass ratios computed at a distance of $100Mpc$. The strain is extrapolated to infinity. The solid line represents the mixed binary waveforms while the dotted line is the binary black hole. The two systems align well with each other during the early inspiral at lower frequencies. However, as the system approaches closer to the merger, the deviations in the spectrum start growing. In particular, the systems with tidal disruption (mass ratio $q = 2, 3$) see a continuous decline in Fourier spectrum with an exponential decay after the cut-off frequency. The behavior changes for the mass ratio $q = 5$ case where instead of monotonic decay, the spectrum grows similar to BBH after the mass shedding frequency followed by an exponential decrease. The cut off frequency in this case is quite close to the quasinormal frequency as also seen in SH-P1 which explains the absence of

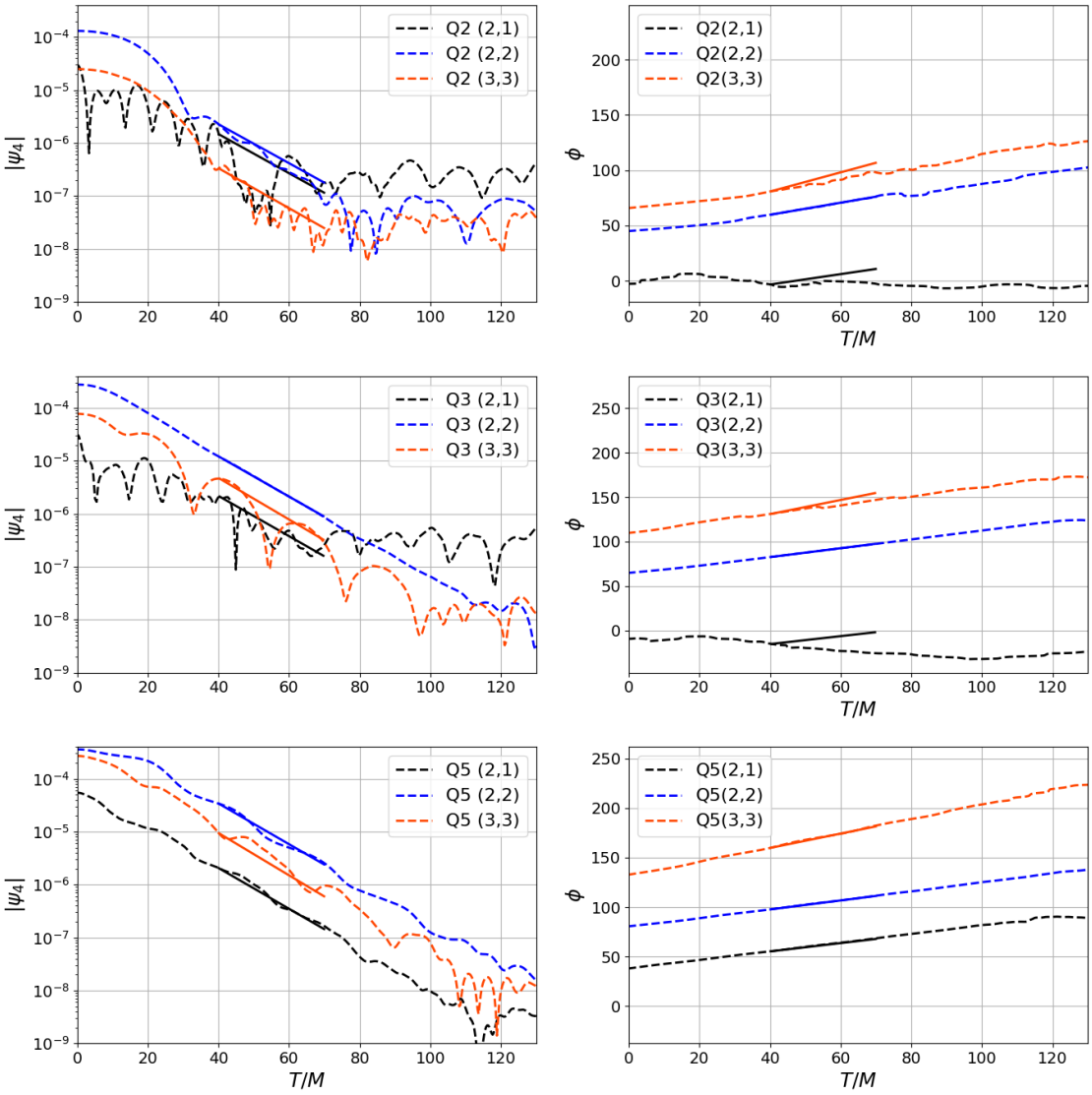

FIGURE 3.12: Postmerger signal analysis - ψ_4 amplitude and phase for post merger signal. The first column represents the log of the amplitude and second column shows the phase. Rows from top to bottom look at (2,1), (2,2), (3,3) and (4,4) modes. Solid lines represents the linear fit used to compute the time decay factor and ringdown frequency.

strong stellar disruption in this case.

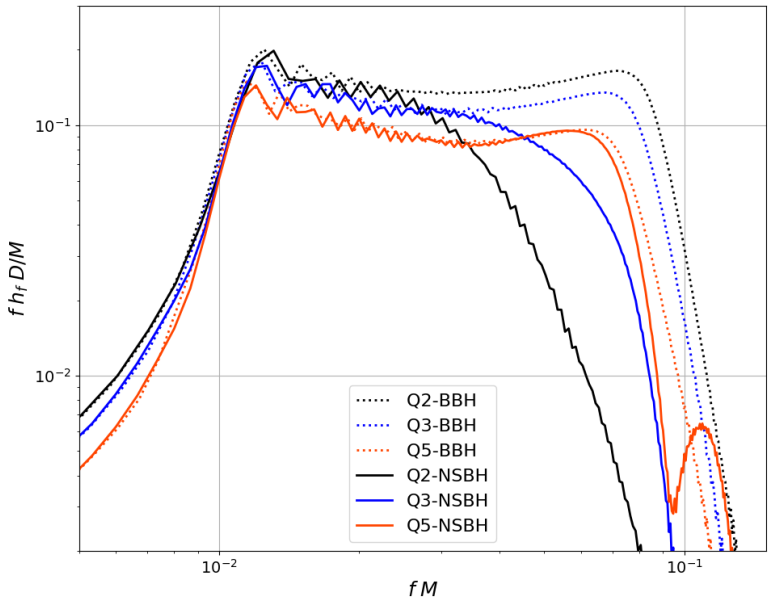

FIGURE 3.13: Fourier Spectrum of Strain. The solid lines correspond to the NSBH signals and dotted lines represent the BBH case. Each source is places at a distance of $100MPc$ in face on orientation. Results are presented in geometric units for ease of comparison with SH-P1.

To compare the NSBH waveforms with corresponding BBH cases, we compute the match between their waveforms including all the modes up to $l = 8$. The total mass for BBH and NSBH systems with mass ratio q is $(1+q) \times \mathcal{M}_S$ (where $\mathcal{M}_S = 1.35M_\odot$ is the mass of neutron star) and source is placed at a distance of $100MPc$. The match is performed using the pyCBC infrastructure [188] where match between two waveforms is defined as [189] -

$$M(\boldsymbol{\theta_1}, \boldsymbol{\theta_2}) = \max_{\phi_c, t_c} \left\langle u_{BBH}(\boldsymbol{\theta_1}),\ u_{NSBH}(\boldsymbol{\theta_2}) e^{\iota(2\pi f t_c - \phi_c)} \right\rangle \tag{3.7}$$

where u_{BBH} and u_{NSBH} are the normalized NR waveform templates for the two systems and $\boldsymbol{\theta}_i$ are the vector of intrinsic parameters. t_c and ϕ_c are coalescence time and phase. The

inner product between any two waveforms u_1, u_2 is defined as

$$< u_1, u_2 > \equiv 4Re \int_0^\infty \frac{\tilde{u}_1^*(f)\tilde{u}_2(f)}{S_h(f)} df \tag{3.8}$$

where $S_h(f)$ is the power spectral noise density. Table 3.4 lists the values of mismatch for the two systems, which is defined as $1 - M(\boldsymbol{\theta_1}, \boldsymbol{\theta_2})$. The mismatch is computed at three different inclinations of 0, $\pi/6$ and $\pi/3$ and two different detectors, Advanced LIGO and Einstein Telescope (ET). The variations in the inclination allow us to study the impact of higher order modes and the choice of two different detectors is based on the differences in their noise sensitivity curve. Due to the low total mass of these systems, the mergers will typically occur at high frequencies which may fall outside the bandwidth of LIGO. Einstein Telescope would allow us to observe even the post-merger/ringdown signal in these cases due to better noise sensitivities at higher frequencies.

Across the detectors, the mismatch is smaller for ET compared to LIGO due to its smaller noise. For $i = 0$, the mismatch is highest for mass ratio 2 and declines with increase in the mass ratio. This is consistent with the previous analysis of the (2,2) mode which is the dominant mode at this inclination. At non-zero inclinations, the contributions from subdominant modes become important and the differences in higher multipole moments of the two systems will be mainly reflected in these modes. For $i = \pi/6$, the mismatch value decreases for $q = 2$ in comparison with its face on configuration ($i = 0$) value due to weaker higher order modes in both BBH and NSBH. In contrast, larger mismatch is observed for $q = 3$ and $q = 5$ case at higher inclinations due to the contributions from higher order modes. The mismatch in mass ratio 5 decreases from 99.54% at face on orientation to 96% at $i = \pi/6$. Things get more interesting for $i = \pi/3$ at which point the contributions of higher modes increase significantly, which leads to a complete change from the previous trend. The mismatch is smallest for $q = 2$ and increases with mass ratio reaching 10% mismatch for $q = 3$ and 12% for $q = 5$. This shows the importance of higher

TABLE 3.4: Mismatch Comparison - This table compares the mismatch between BBH and NSBH waveforms with mass ratio q for three different inclination angle i and for two different detectors. Each waveform includes higher modes till $l = 8$ and is computed using FFI method, standardized with mean centering and extrapolated to infinity.

q	**Detector**	$i = 0$	$i = \pi/6$	$i = pi/3$
2	LIGO	0.085	0.076	0.074
2	ET	0.077	0.069	0.067
3	LIGO	0.061	0.073	0.098
3	ET	0.046	0.058	0.081
5	LIGO	0.005	0.04	0.119
5	ET	0.003	0.035	0.107

modes in the study of mixed binaries at high mass ratio.

3.3.4. SYSTEMATIC ERRORS

Eccentricity - The apparent differences between BBH and NSBH show the failure of PN approximation at this separation. This is reflected as early oscillations in the orbital separation plots 3.3 at the beginning of the simulations. Using equation 19 from [190], we find that eccentricities are of the order $10^{-3} - 10^{-2}$ for both BBH and NSBH cases. Table 3.2 lists the values of eccentricity, number of orbits, and time of merger for each simulation case. We note that similar eccentricities were also reported in ST-P1.

Junk Radiation - Due to the close resemblance with Bowen-York approach [110], out initial data shares its flaws with a few additional complications. The prior assumptions of conformal flatness makes the system initially unstable and results in a burst of junk radiation in the beginning of simulation. As shown in reference [158] for BBH case, some of this radiation is absorbed by the black hole which alters its mass and spin. The effect of junk radiation on the neutron star is less understood and requires further investigation.

Density Oscillations - The imperfections in the initial data have more adverse effects on the neutron star and can artificially excite its quasinormal modes. Due to the assumptions of conformal flatness, neglect of tidal effects, violations of continuity equation and/or artificial boost, the star suffers an initial perturbation which results in oscillations in the stellar density and stellar radius throughout the inspiral. The amplitude of oscillations increases with mass ratio changing the densities from $18\% - 30\%$ of the original values. This has been a known problem with TOV stars [162], binary neutron stars [191] and mixed binaries [100, 192]. However, the star itself remains stable with negligible loss of mass of the order of $10^{-4}M$. The density of the lost mass is smaller than $10^{-7}/M^2$. As such, the oscillations are not expected to affect the accretion disk mass except for very high mass ratio cases where the mass and density of the material have comparable values.

The pulsations in the star also affect the gravitational waves as reflected in the oscillations in the amplitude of (2,2) mode shown in the right panel of figure 3.10. To understand the effects of the wobbling star, we look at the Fourier spectrum of its central density and (2,2) mode of Ψ_4 frequencies, $\omega_{\Psi_4} = \frac{1}{2\pi}\frac{d\, arg(\phi^{22})}{dt}$, where $\phi^{2,2}$ is the phase of ψ_4. The frequency evolutions of Ψ_4 are extremely noisy due to lower finite difference order, imperfect boundary conditions, mode mixing and other numerical errors. The emission of junk radiation further adds to the noise before the system settles into a stable evolution. Hence, to counter these effects we look at a brief window of $200M$ in the inspiral band after junk radiation has passed. At this point, the star is still further away from black hole which tends to decrease the effects of tidal forces on the star leading to relatively stable oscillations. We then use polynomial fitting to isolate the effects of frequency evolution of the binary from the oscillations and look at the relative oscillation amplitude $\left|(\omega_{\Psi_4} - \omega^{fit}_{\Psi_4})/\omega^{fit}_{\Psi_4}\right|$. To remove the side effects of numerical noise, we apply low pass filters removing frequencies $> 6kHz$. From figure 3.14, the Fourier analysis of density oscillations reveal the oscillation frequency in range $1250 - 1320$ Hz which resembles closely to the fundamental f-mode. The results from ω_{Ψ_4} are also of similar order although they are less reliable due to more

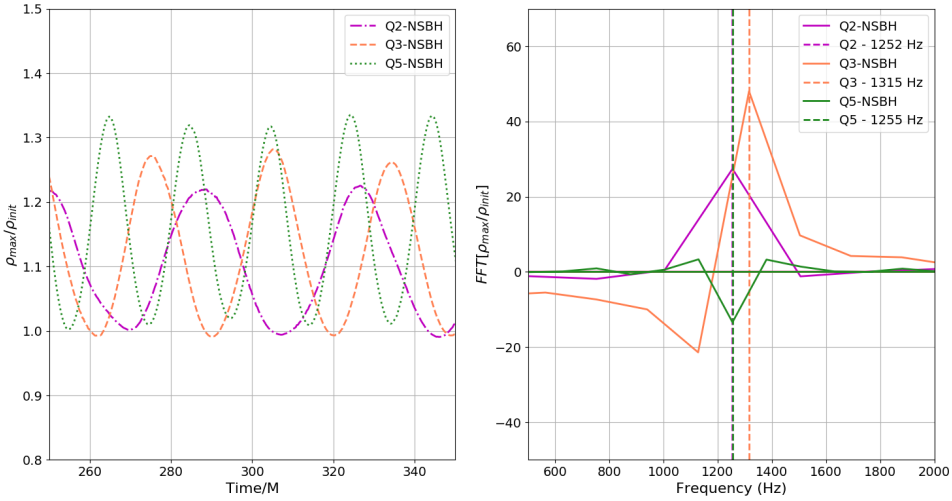

FIGURE 3.14: Density oscillations in neutron star - Panel on the left shows the relative oscillations in the central density of the star as a function of mass ratio. Panel on the right shows its Fourier transform.

noisy data. The gravitational wave signals from such stars are extremely weak in comparison to a mixed binary and their effects are visible only at very high frequencies ($> 1000Hz$). As a result, impact of such oscillations on the gravitational wave signatures of the mixed binary cannot be detected with present detectors and can safely be ignored. We note that due to limited cycles in the inspiral band, the true oscillations from the tidal effects are difficult to isolate from the numerical artifacts in the present work. A more thorough analysis to understand the cause(s) of density oscillations would require longer simulations with a significantly larger number of inspiral cycles, looking at the density profiles at different radii and performing a mode by mode comparison with Ψ_4. This will be left for the future work.

COM Offset - One major issue with our current simulations is the offset in the center of mass (COM) location. Artificial COM offsets can arise from improper choice of gauge conditions or problems with the initial data. As can be seen in 3.2, such offsets can be

significantly large for mixed binary systems and tend to increase with mass ratio. This can be problematic for systems with higher degree of asymmetry. A common known issue due to COM offset is mode mixing reflected as oscillations in amplitudes of higher order modes. To extract Ψ_4 into spin weighted spherical harmonic functions, we set up fixed spherical detectors centered at the origin of the coordinate system assuming it coincides with the center of mass. Offset of source from the origin leads to differences in arrival times of gravitational waves at distinct regions of the detector. Treating these differences as translations in time [193, 194], it can be shown that the waveform $h(t)$ under translation $\overrightarrow{\alpha}_T$ and boost $\overrightarrow{\beta}_T$ transforms as

$$h(t) \rightarrow h(t + (\overrightarrow{\alpha}_T + \overrightarrow{\beta}_T t).\hat{r}) + \mathcal{O}\left(|\overrightarrow{\beta}_T|\right) + \mathcal{O}\left(|\overrightarrow{\alpha}_T + \overrightarrow{\beta}_T t|^2 \partial_t^2 h\right) \tag{3.9}$$

Boyle et al. [193] studied the effects of the space and time translations, and boosts on gravitational wave strain and showed that such transformations introduce angular dependence in the coefficients of spherical harmonic functions which leads to coupling between various l, m modes. The effect of mode mixing on the gravitational waveform is shown in figure 3.15 as oscillations in the amplitude of different modes. The first panel on the left shows the oscillations in subdominant modes of NSBH while the second panel compares two BBH $q = 5$ simulations with zero and non-zero COM offset.

There are a few different ways to resolve this. The most ideal way will be to improve the initial data and find an optimal gauge condition which prevents the epicyclic motion of center of mass. Although non-trivial to find, such gauge conditions can reduce mode mixing and other artifacts which occurs as a result of COM motion. To fix the current waveforms affected by the offset, we can pursue the approach developed in [193, 194] for binary black hole problems. They compute the effects of time and boost translations on waveform using 3.9 and adjust the waveforms by corresponding factors. This is currently an ongoing work.

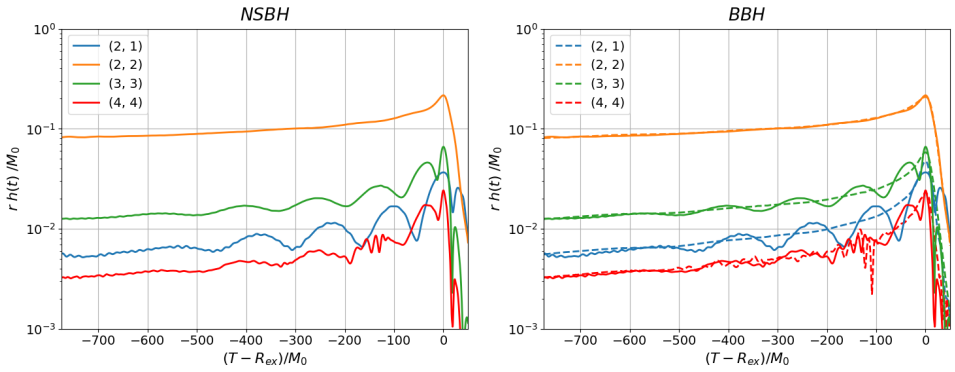

FIGURE 3.15: Amplitude oscillations due to COM offsets. Panel on left shows dominant and subdominant modes for NSBH $q = 5$ while panel on right shows the same for BBH $q = 5$ cases. Solid lines represent COM offset of $1M$ while dashes lines correspond to $0M$ offset.

CHAPTER 4

JUNK RADIATION

4.1. INTRODUCTION:

One of the problems common to compact binary simulations is junk radiation. This is artificial radiation present in the system due to the inherent assumptions in the initial data. As discussed in chapter 2, the initial data problem is not exactly solvable due to higher degrees of freedom than the constraints. To tackle this, we rely on the CTT method which uses York-Lichnerowicz approach [195, 196] to fix the unknowns in metric and extrinsic curvature by assuming conformal flatness, maximal slicing and vanishing transverse curvature components. While the assumption of conformal flatness provides an easy and clear route to design the initial data, it does not correctly reflect the true state of the system. This can be seen from the solutions of single boosted or rotating star or black hole which are not conformally flat. As an example, let's consider the Kerr spacetime whose metric in the Kerr-Schild form can be written as [197] -

$$g_{ab} = \eta_{ab} + 2Hl_a l_b \tag{4.1}$$

Here, l_a is a null vector with respect to g_{ab} and η_{ab} and H is a function of mass, spin and coordinates. The presence of additional mixed terms on the RHS prevents a conformally flat solution of Kerr. For a very large separation where tidal interactions are negligible, each black hole in a compact binary can be approximated as a rotating and/or boosted black hole and hence, modelling this spacetime with conformally flat initial data will lead

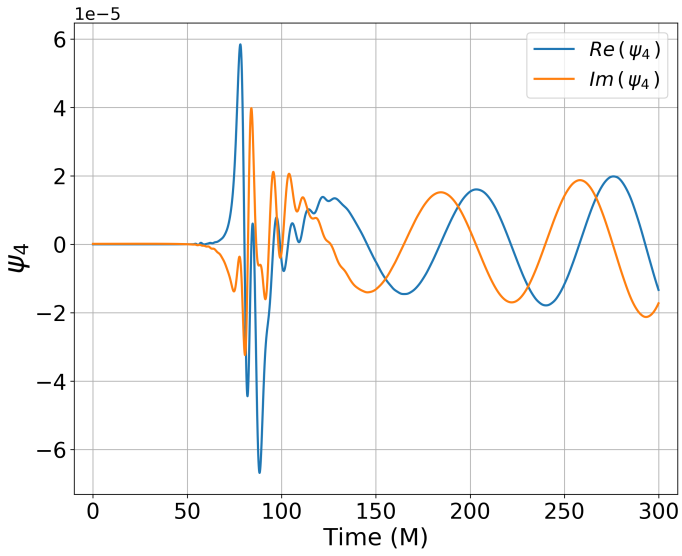

FIGURE 4.1: Here, we show the (2,2) mode of ψ_4 for a precessing BBH waveform. The noise in the first $140M$ of the waveform is due to the junk radiation.

to systematic errors resulting in a burst of spurious radiation.

This burst can affect the source objects and the corresponding gravitational wave signatures. Figure 4.1 show the (2,2) mode of Weyl scalar Ψ_4 for binary black hole case. The presence of the burst contaminates the initial gravitational wave signal and hence, needs to be discarded. The artificial radiation can also perturb or be absorbed by the black hole or neutron star which would affect the source parameters altering the state of the system from the desired configuration. This begs the question - how small or drastic these changes can be? In this work, we focus on measuring the effects of junk radiation on binary black holes using the Georgia Tech BBH simulation catalog [177]. We develop a new method to provide adjustments in the initial desired configuration by accounting the effects of junk radiation. Such a change would leave the system with the intended parameters after the burst. The effect of junk radiation on mixed binaries will be left for future work.

Reference and Contribution: This work is part of the study [158] led by Kenny Higginbotham. In this chapter, I present my contribution to this work and some of the results

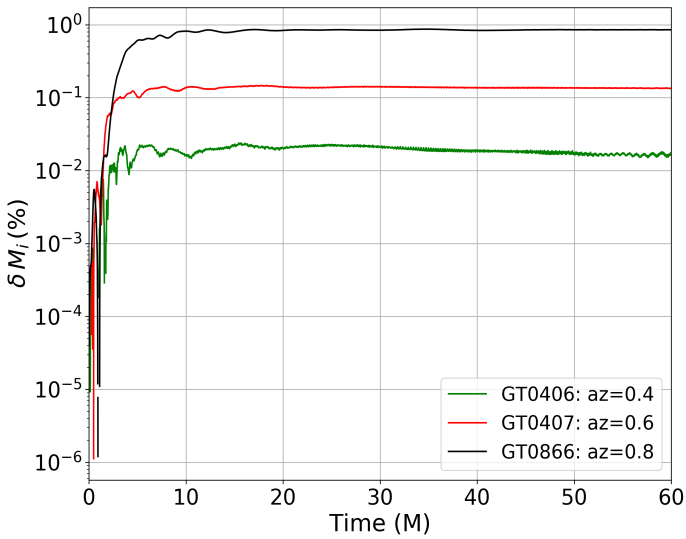

FIGURE 4.2: Percent error in the irreducible mass of the black holes for simulations GT0406, GT0407 and GT0866 due to absorption of junk radiation.

obtained from my analysis.

4.2. BBH WAVEFORM ANALYSIS:

The physical characteristics of each black hole are determined by their mass and spin (momenta controls the eccentricity of the binary) which are hence relevant even from an observational perspective. As numerical relativity models are used in designing analytical and phenomenological waveforms, it is important to account for the errors in these parameters. Hence, we first analyze the effect of junk radiation on these parameters. Figure 4.2 shows the percent error in initial irreducible mass for three GT simulations - GT0406, GT0407 and GT0866. There is a clear increase in the mass of initial binary during the first $20M$ of evolution which shows the junk radiation is absorbed by the black hole. Similar results were found for the spins.

Given the behavior of a black hole as an isolated horizon during the inspiral [145] and short timescales of changes in its mass and spin, we hypothesize that the interaction

of black hole with junk radiation in a binary is completely local and independent of its companion. Hence, it should be possible to measure the resulting changes in BH mass and spins by studying isolated black holes. To investigate this, we perform numerical simulations for single isolated black holes constructed using the same initial data method. To cover the spectrum of BBH configurations, the initial dimensionless spin magnitude, $a = S/M_h^2$, of single black hole ranges from 0 to 0.8 while the speed $v = P/M_h$ covers the range of $0 - 0.3$. Here, S is the dimensional spin magnitude of the black hole, M_h is the Christodoulou mass, and P is the magnitude of linear momentum. The spin of the black hole was chosen to be in z-directions while the velocity was in y-direction to mimic the non-precessing BBH confgurations. Our results indicate a similar increase in mass and spin in first $20M$ of evolution of a single black hole which serves as a good evidence for our hypothesis.

We can now use the single black hole results to construct fits of mass and spin percent errors as a function of initial speed and initial spin of the black hole. From our initial hypothesis, it should then be possible to estimate the changes in mass and spin of the black holes in BBH systems using these fitting formula.

Plots (A) and (B) in figure 4.3 show the fits as grey surfaces for percentage errors in the irreducible mass and dimensionless spin of the single black hole as a function of initial speed and initial dimensionless spin. Blue dots represent the values from the simulation. Here we have used fifth-order polynomial fits for both mass and spin which can be written as

$$
\begin{aligned}
F &= c_{00} + c_{10}a + c_{20}a^2 + c_{30}a^3 + c_{40}a^4 + c_{50}a^5 \\
&+ c_{01}v + c_{02}v^2 + c_{03}v^3 + c_{04}v^4 + c_{05}v^5 \\
&+ c_{11}av + c_{12}av^2 + c_{13}av^3 + c_{14}av^4 \\
&+ c_{21}a^2v + c_{31}a^3v + c_{41}a^4v \\
&+ c_{22}a^2v^2 + c_{23}a^2v^3 + c_{32}a^3v^2 \qquad (4.2)
\end{aligned}
$$

The coefficients for each case are given in table 4.1. The residuals of the fit are a factor of 100 smaller than the mass and spin errors as shown in subplots (C) and (D) of the same figure.

Few interesting relationships can be seen from these fits. First, the percent changes in irreducible mass are primarily affected by initial black hole spin and have a very weak dependence on the initial speed. The interaction with junk radiation always leads to an increase in the mass and the relative change depends on the initial spin of the black hole. In contrast, the changes in spin show a negative correlation with initial spin and a positive relationship with the initial speed of the hole which suggests that junk radiation can decrease the angular momentum of highly spinning black holes. On the other hand, the angular momentum is increased for black holes with high boost. One can thus find a family of cases for which these effects cancel out and there will be no net change in the spin. These cases are denoted by the black line in Fig. 4.3b. We note that no significant change in the orientation of the spin was observed, which suggests that only magnitude of the spin is affected by the junk radiation.

To test our initial hypothesis, we now compare these fits with the changes in irreducible mass and spin values of each black hole in BBH simulations. From our catalog, due to the limitation of available mass and spin data, we look at 67 precessing and 40 aligned spin

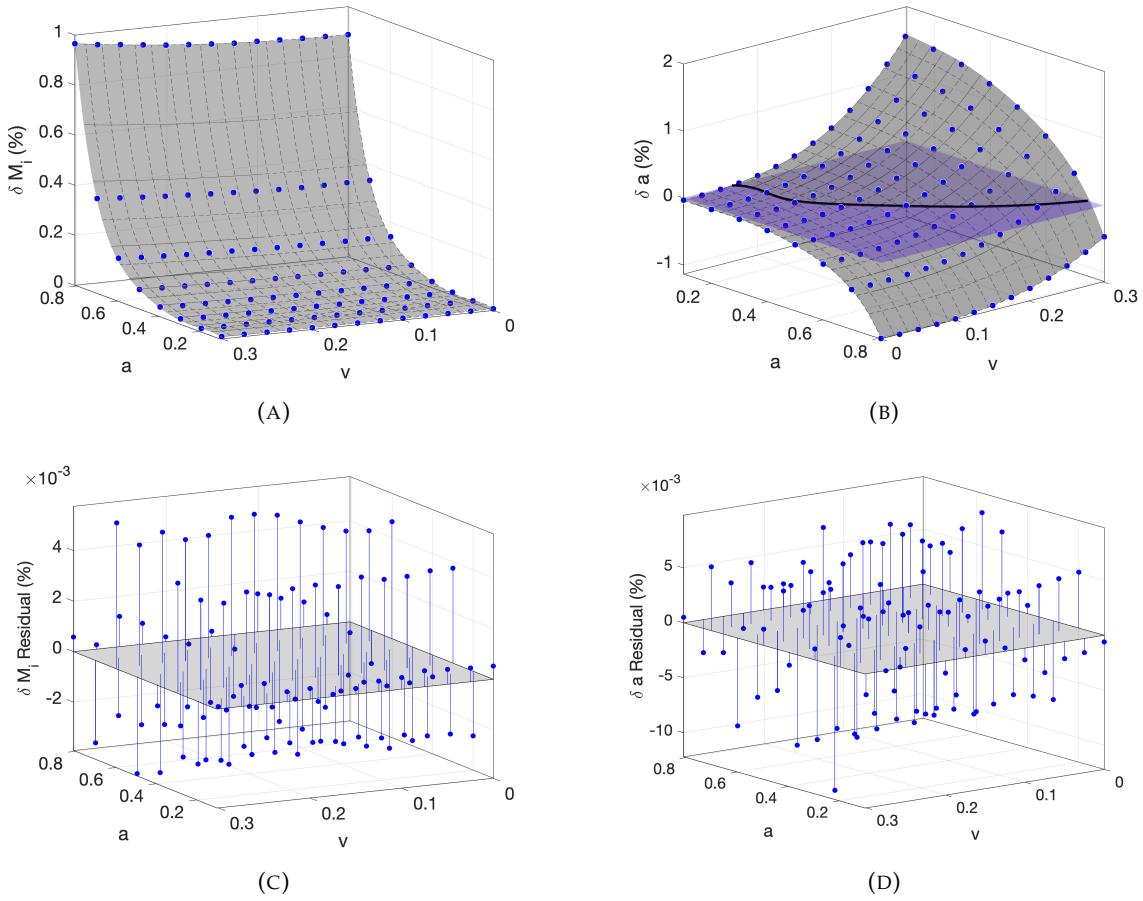

FIGURE 4.3: Percent change in irreducible mass (A) and spin (B) in the single black hole simulations (blue dots). Two-parameter fits to the data as a function of speed and dimensionless spin given by Eq. (4.2) are shown as grey surfaces. Residual of each fits are shown in (C) and (D).

systems. Figure 4.4 shows a comparison of single black hole fits of percent change in irreducible mass (subplot (A)) and spins (B) with BBH simulations. The grey surfaces show the fits from single black hole simulations, the red dots correspond to aligned spins and turquoise dots correspond to precessing simulations. The residuals (differences between predicted and true values) are shown in (c) for irreducible mass and (d) for spins. The higher residuals in this case compared to BBH show the imperfections in our model and suggest that the interactions between the binaries cannot be completely ignored. For the

TABLE 4.1: Fitting coefficients for δM_i and δa in Eq. 4.2.

c_{ij}	δM_i	δa	c_{ij}	δM_i	δa
c_{00}	-0.09935	0.1294	c_{40}	-65.83	79.59
c_{10}	2.148	-3.169	c_{31}	-4.27	13.47
c_{01}	0.05612	-0.0977	c_{22}	-1.565	-5.56
c_{20}	-14.92	21.01	c_{13}	3.918	-13.17
c_{11}	-0.4674	1.118	c_{04}	-21.74	288.9
c_{02}	-0.6845	7.696	c_{50}	36.64	-40.72
c_{30}	46.3	-61.24	c_{41}	2.524	-7.763
c_{21}	2.386	-7.675	c_{32}	2.931	2.056
c_{12}	-0.2141	2.781	c_{23}	-0.7278	-35.24
c_{03}	5.791	-15.01	c_{14}	-5.623	12.7
			c_{05}	29.78	-413.8

irreducible mass, however, these interactions are still weak for both aligned and precessing which is reflected by low residuals of order O(10^{-2}). The spin residuals are of the order O(10^{-1}) for $v \leq 0.24$ but increase in magnitude to O(1). From subplots of spin fits (B) and residuals (D), it can be seen that the single black hole fits overestimate the changes in spin magnitudes of black holes with higher initial velocity. This can be explained in the following way - black hole initial momentum increases with the orbital frequency and hence, will have higher speed for smaller separations. As a reference, the speed of black holes, $v > 0.24$ for separations smaller than $10M$. At such small separations, the interactions between two black holes will be non-negligible and hence, cannot be completely ignored. However, for separations larger than $10M$, our initial hypothesis holds well and hence, the single black hole fits can be used for BBH case which is reflected by low residuals in irreducible mass and spin percent changes.

4.3. MODIFICATIONS IN INITIAL DATA:

Given the majority of NR simulations fall under the regime where our hypothesis holds well (i.e., most simulations have an initial separation $> 10M$), we can use the fits of irreducible mass and spins from a single black hole to account for the effects of junk radiation

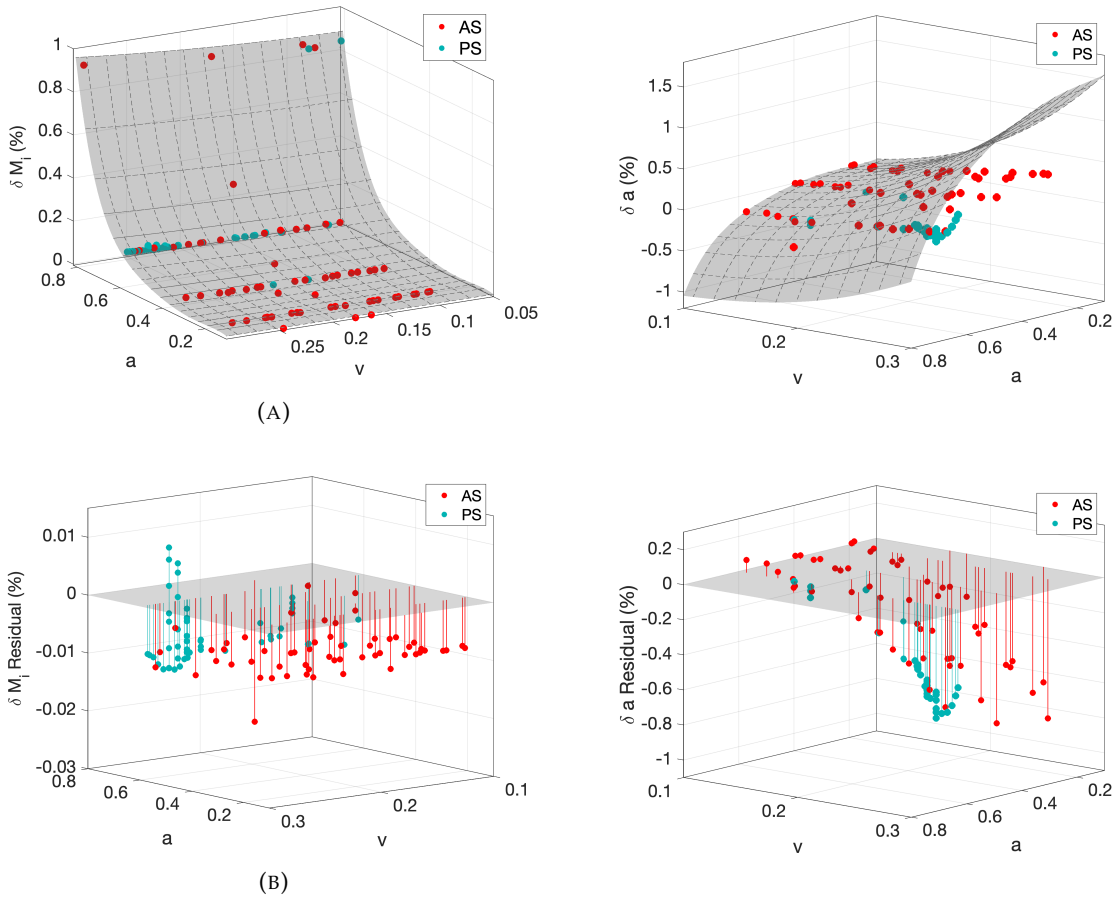

FIGURE 4.4: Comparison of SBH irreducible mass error fits (a) and spin error fits (b) with data from BBH simulations. The red dots correspond to aligned spins and turquoise dots correspond to precessing simulations. The errors between predicted and true values are shown in (c) and (d).

in BBH case. Here, we present a simple model to alter the initial mass and spin values of black holes in a binary such that after the dissipation of junk radiation, the system relaxes to the desired configuration. Let $\mathcal{M}_i^{1,2}$ and $a^{1,2}$ be the desired irreducible masses and spins of the black holes we wish to simulate. Let $\bar{\mathcal{M}}_i^{1,2}$ and $\bar{a}^{1,2}$ represent the altered initial masses and spins. Our goal is to find $\bar{\mathcal{M}}_i^{1,2}$ and $\bar{a}^{1,2}$ such that after the end of junk radiation phase, the mass and spins of black holes are $\mathcal{M}_i^{1,2}$ and $a^{1,2}$. This can be achieved by solving

TABLE 4.2: Mass and spin of BH at the initial time and after the junk radiation has dissipated.

Type	$t = 0$			$t > t_{\rm sp}$		
	M_h/M	M_i/M	a	M_h/M	M_i/M	a
raw	0.4994	0.4736	0.6013	0.5004	0.4744	0.6032
adj	0.4985	0.4729	0.6000	0.4994	0.4736	0.6018
raw	0.4972	0.4430	0.8090	0.5001	0.4471	0.8013
adj	0.4939	0.4387	0.8161	0.4971	0.4431	0.8079

the following equations -

$$M_i^{1,2} = [1 + \delta \bar{M}_i^{1,2}(\bar{a}^{1,2}, v^{1,2})]\, \bar{M}_i^{1,2} \tag{4.3}$$

$$a^{1,2} = [1 + \delta \bar{a}^{1,2}(\bar{a}^{1,2}, v^{1,2})]\, \bar{a}^{1,2} \tag{4.4}$$

Here, $v^{1,2} = P^{1,2}/\mathcal{M}_h^{1,2}$ are the initial speeds of each black hole, and $\delta\bar{M}_i^{1,2}$ and $\delta\bar{a}_i^{1,2}$ represent the fractional (not percentage) changes in irreducible mass and spins of the black holes which can be computed from the fits. The above equations can easily be solved with Newton's method or other root finding algorithms.

Let's consider a few examples where the effects of junk radiation can be relevant. We consider equal mass high spinning BBH configurations with spins of 0.6 and 0.8 for which the expected changes in black holes' masses and spins are significant. Table 4.2 presents the raw and adjusted values for Christodoulou mass, irreducible mass and dimensionless spin at the initial time and after the passing of junk radiation, t_{sp}. Here, 'raw' type refers to the desired initial configuration and 'adj' type refers to the modified values using equations 4.3. Notice that the mass and spin values for $t > t_{sp}$ in adjusted case match to a good accuracy with corresponding raw values at $t = 0$. This shows that our method works as intended. The modified values are used with post Newtonian method to recompute the momenta for the new adjusted configurations.

Figure 4.5 presents the comparisons of the (2,2) mode of Weyl Scalar for the four cases listed in table 4.2. The plots in the top and bottom panels correspond to $a \approx 0.6$ and $a \approx 0.8$

cases. The dashed blue lines denote the waveform corresponding to the raw initial data, while the solid orange lines correspond to the adjusted configuration. We see that even though the signal overlaps well in the early inspiral, the differences in the signals and merger time for the raw and adjusted configurations increase with the initial spin of the binary. The resulting differences in the initial momentum explain the differences between the merger times of the raw and adjusted configurations.

Thus, we find that the effects of junk radiation can alter the initial masses and spins of the binary and its gravitational wave signatures. For initial separations $D_{NR} > 10$, such effects can be assumed to be local to black hole and tidal interactions can be safely ignored. Using the method developed in this work, it is possible to modify the initial configuration to account for the effects of junk radiation. It is expected that these methods can also be applied to the black hole in a mixed binary system. Due to the lack of NSBH simulations, the effects of junk radiation on a neutron star are more harder to analyse and account and hence, they will be left as part of future studies.

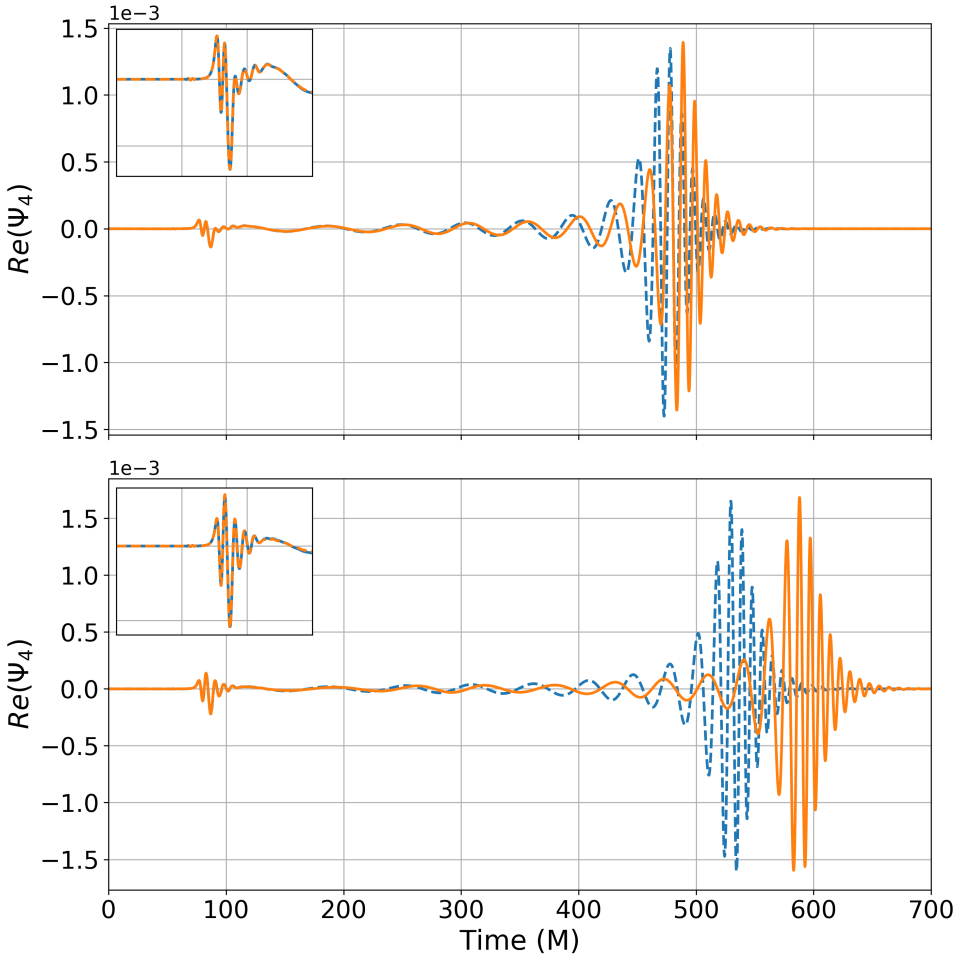

FIGURE 4.5: Top panel shows the (2,2) mode of Ψ_4 for equal mass, aligned spin BBH with $a \approx 0.6$ and the bottom panel shows the same but for $a \approx 0.8$. Blue dashed lines represents the *raw* simulation and orange solid waveform depicts the adjusted simulation. Inset zooms into the junk radiation part of the signal.

CHAPTER 5

MIXED BINARY SIMULATIONS- COMPACTNESS STUDY

In chapter 3, we investigated the dynamics of mixed binary mergers for various mass ratios and found a close resemblance between the gravitational wave signatures of these systems and black hole binaries for higher mass ratio cases. The primary reason of similarity is due to the nondisruption of the star almost until the merger which leads to stronger excitation of multipole moments of remnant black hole. From equation 3.3, an alternate way to control the stellar disruption is by varying its size. In this chapter, we focus our attention on the variation in the compactness of the neutron star and its effects on the gravitational wave signatures. Compactness of a neutron star is directly related to the equation of state model and hence, the ability to determine this property can help to constraint the existing models of the equation of state. However, unlike black holes, the size of neutron stars is limited by the observational constraints. As a result, the effects of variations in compactness are less pronounced. In this work, we will analyze the dynamics of NSBH mergers for four different configurations where stellar compactness plays an important role in remnant formation. Section 5.1, we provide the details of the four initial configurations, followed by a brief description of modifications to the grid structure. We then look at the dynamics of merger and analyze the source properties. At the end, we inspect the gravitational wave signatures to find features which can help us distinguish between stars of different compactness.

TABLE 5.1: Initial configuration of mixed binary in polytropic units. q refers to the mass ratio, C is the compactness of the isolated TOV, $\overline{D}$ is the initial coordinate separation, $\overline{\mathcal{M}}_h$ is Christodoulou mass of the black hole, $\overline{\mathcal{M}}_A$ is the ADM mass of the isolated TOV, $\overline{\mathcal{M}}_o$ is the rest mass of the isolated TOV, $\overline{\rho}_{max}$ refers to the central density of the star in binary at the initial time and $M\Omega$ is the initial orbital frequency (from PN)

Models	q	C	$\overline{D}$	$\overline{\mathcal{M}}_h$	$\overline{\mathcal{M}_A}$	$\overline{\mathcal{M}}_o$	$\overline{\rho}_{max}$	$M\Omega_0$
$NSBH-C0.12$	3	0.123	4.32	0.36	0.124	0.132	0.095	0.032
$NSBH-C0.15$	3	0.154	5.022	0.418	0.144	0.155	0.139	0.032
$NSBH-C0.18$	3	0.18	5.472	0.456	0.156	0.171	0.193	0.032
$NSBH-C0.20$	3	0.20	5.688	0.474	0.162	0.177	0.252	0.032

5.1. INITIAL CONFIGURATIONS

From the Newtonian expressions for mass shedding and ISCO frequency, Taniguchi et al. [80] obtained the mass ratio-compactness relationship (Figure 5.1) which differentiates between tidal disruption versus non-disruption cases. Using this as the base model, we consider four non-spinning configurations of mixed binary with mass ratio $q = 3$ where the system transitions from complete disruption to non disruption state. Compactness of neutron star for resulting configuration varies from 0.12 to 0.2, as shown in figure 5.1. The choice of parameters is to explore the degree of tidal disruption (for $q = 3$) and its effects on source properties and gravitational wave signatures. To construct the initial data, we begin by choosing the desired mass of TOV is $\mathcal{M}_S = 1.35M_\odot$. The baryonic mass, $\mathcal{M}_o$, now varies from $1.43M_\odot$ to $1.47M_\odot$ as a function of its compactness. In Schwarzschild coordinates, the radius of the star in the isolated state ranges from 10km to 17km. We continue to model TOV using a polytropic equation of state with $\Gamma = 2$ and the polytropic constant K_{poly} can be determined from values of black hole mass in physical and polytropic units related by $\overline{\mathcal{M}}_h = \mathcal{M}_h/\sqrt{K}$ where the mass of the black hole in physical units can be computed as $\mathcal{M}_h = q * \mathcal{M}_S$. Initially, the binary is separated at a distance of $9M$ where $M = \mathcal{M}_S * (1+q)$. Table 5.1 provides a more detailed summary of the initial configuration. The name of the models represents the system type and the compactness of the star (C).

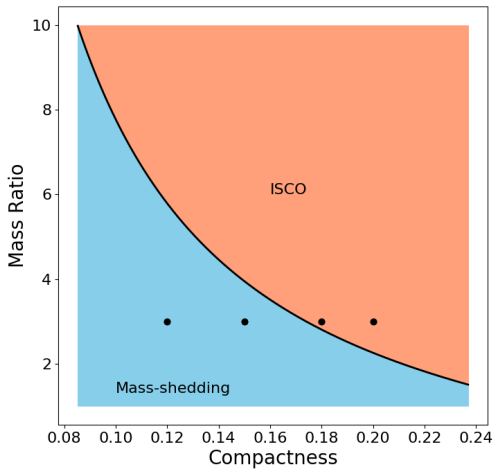

FIGURE 5.1: Critical curve based on the Newtonian relationship between mass ratio and compactness [78, Equation 104] which isolates binaries reaching ISCO versus others suffering tidal disruption

The initial data setup follows the same method as described in the previous chapter. We start with the point particle assumption and solve PN equations to compute the momentum of each particle in the binary. To obtain the initial state of the neutron star, we set up a static TOV with polytropic equation of state and an initial guess density which is iteratively evolved to find the configuration with desired masses. Placed at the distance of $9M$ with momentum computed by post-Newtonian approach, we now solve for the ADM and hydro variables for this system of a black hole and a neutron star using the method illustrated in [143]. This is followed by the spacetime and hydrodynamics evolution and computation of gravitational waves using the machinery described in chapter 2 and section 3.1.

Grid Setup: The grid setup follows the method illustrated in section 3.1 but with slight alterations. To ensure uniformity across the runs and avoid any artifacts due to low resolution,

we implement following three conditions -

- Neutron star is resolved with at least 50 points along the radius or minimum of $230m$ of resolution
- Black hole radius is covered with at least 25 points.
- Gravitational wavelength is resolved with at least 50 points.

These conditions are based on the analysis from previous work by other groups (check [78] for summary). To meet these conditions, we start with $8-9$ levels of refinement on the star. Star is covered by 100^3 points except in the case of NSBH-C0.12 where we increase number of points across the surface to 130^3 due to its larger size. The side length of grid level embedding the star is chosen as $2.4R_{Iso}$ (isotropic radius of the star) to reduce the errors from stellar oscillations. Additional levels are added on the black hole to ensure proper resolution of the horizon surface. The size of refinement levels is increased by a factor of 2 except the one at the beginning of gravitational wave detectors where expansion factor of four is used to have optimal resolution on the outer grids covering the detectors. For extracting Ψ_4, we place ten spherical detectors at a distance of $50M$ to $140M$ while the largest refinement has the size of $> 250M$. The larger size of the outer domain decreases the effects of boundary reflections while ensuring proper extraction of gravitational waves in the wavezone.

5.2. RESULTS

5.2.1. ORBITAL DYNAMICS

The effects of compactness of the neutron star on NSBH dynamics are more subtle than variations in the mass ratio. From Newtonian analysis (equation 3.3), the tidal radius shows an inverse relationship with the compactness. Thus, reducing the compactness of

the neutron star can lead to larger tidal radius compared to ISCO, increasing the possibility of tidal disruption. However, due to the observational constraints on the radius of the neutron star, the compactness cannot vary to a large extent, keeping the relationship between tidal and ISCO radius unchanged for $q > 5$ in the absence of spins. Here, we explore four different configurations for mass ratio $q = 3$ where such a switch in the inequality is possible within the observational radius of the neutron star.

In figure 5.2, we look at the rest mass density contours of the given configurations. Rows from top to bottom represent the different stages of density evolution for each configuration arranged in increasing order of compactness. The axes show x and y coordinates in units of total mass M and color bar represents the rest mass density in the same unit system. The white circle represents approximate black hole boundary and the red circle corresponds to the ISCO radius [1]. The tidal radius for models NSBH-C0.12 and NSBH-C0.15 is much larger than ISCO radius, which suggests possible disruption scenarios. During the early inspiral, the star remains fairly stable without significant dissipation of mass irrespective of the compactness. While oscillations in the star due to imperfections in the initial data can lead to changes of up to 35% in its central density, the mass loss remains less than 0.2% of initial stellar rest mass. As the star approaches ISCO, the outer layer of neutron star begins to form a tail of low density matter connecting to the black hole which suggests the beginning of mass shedding. For systems with low compactness, the Roche lobe overflow occurs much before the star reaches ISCO. The star slowly deforms assuming a "tear" shaped structure as the tail grows stronger in density with an increased flux of matter falling on the horizon. As the compactness increases, mass shedding of the neutron star occurs closer to the merger at higher orbital frequencies as seen in the panels of column 1. This is consistent with results from the study of quasiequilibrium states of mixed binaries [80] according to which the mass shedding frequency, Ω_{MS}, is proportional to the

[1] While definition of ISCO radius holds on for quasiequilibrium case, here, we use the ISCO radius of Schwarzschild black hole as an approximation following reference [198].

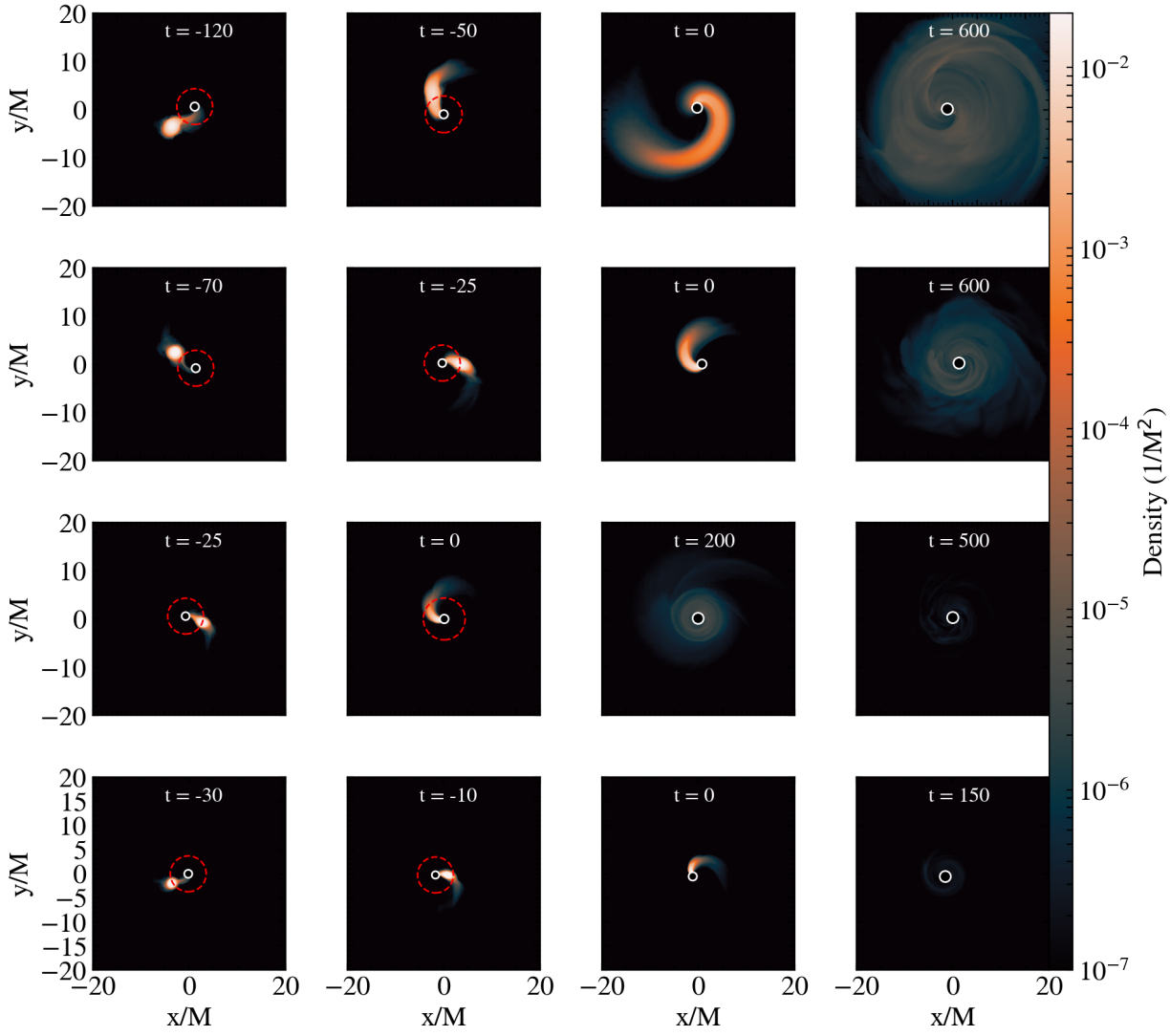

FIGURE 5.2: Rest mass density contour plots in the x-y plane for mass ratio 3 configurations. Rows from top to bottom represents models NSBH-C0.12, NSBH-C0.15, NSBH-C0.18, and NSBH-C0.20 while columns show different stages of evolution marked by time in the figure. Here, $t = 0M$ corresponds to the retarded time of peak radiation. The white circle represents the horizon boundary while the red circle corresponds to the ISCO radius.

compactness via the following relation

$$\Omega_{MS} \propto \left(\frac{\mathcal{M}_A}{{R_S}^3}\right)^{1/2} \left(1+\frac{1}{q}\right)^{1/2} \tag{5.1}$$

The mass transfer is followed by total or partial disruption of the neutron star. For NSBH-C0.12, it begins with complete deformation of the outer surface of the star at ISCO (II panel in the first row). As matter accretes from the stellar core on the black hole, the angular momentum is transported to the left-over material of the star which forms a long spiral arm centered around the black hole (III panel in the first row). The spiral arm expands outward to lengths $\sim 20M$ and circularizes around the black hole (IV panel in the first row). This process lasts for more than $600M$ after the merger as the disk continues to evolve and become more stable by the end of the simulation with densities $\sim 10^{-5}/M^2$. The process of disruption is less violent in NSBH-C0.15 case. Most of the stellar core is already inside ISCO and is engulfed by the black hole before complete disruption of neutron star (II panel in the second row). The partial disruption reduces the angular momentum transport to the outer material affecting the accretion disk formation. The disrupted star forms a smaller spiral arm of lengths $\sim 10M$ (III panel in the second row) and resulting accretion disk has lower densities of $\mathcal{O}(10^{-6})$ and only half the size. In the other two cases, the tidal radius is smaller than the ISCO radius and hence, mass dissipation begins very close to the merger. As a result, most of the material quickly falls into the black hole before the star can face strong disruption effects. Partial disruption of the star in NSBH-C0.18 generates an accretion disk with extremely low density and smaller size, but is eventually engulfed by the black hole by the end of the simulation (Panels III and IV of the third row). No stellar disruption or accretion disk formation is observed for NSBH-C0.20 case (Panel IV in forth row).

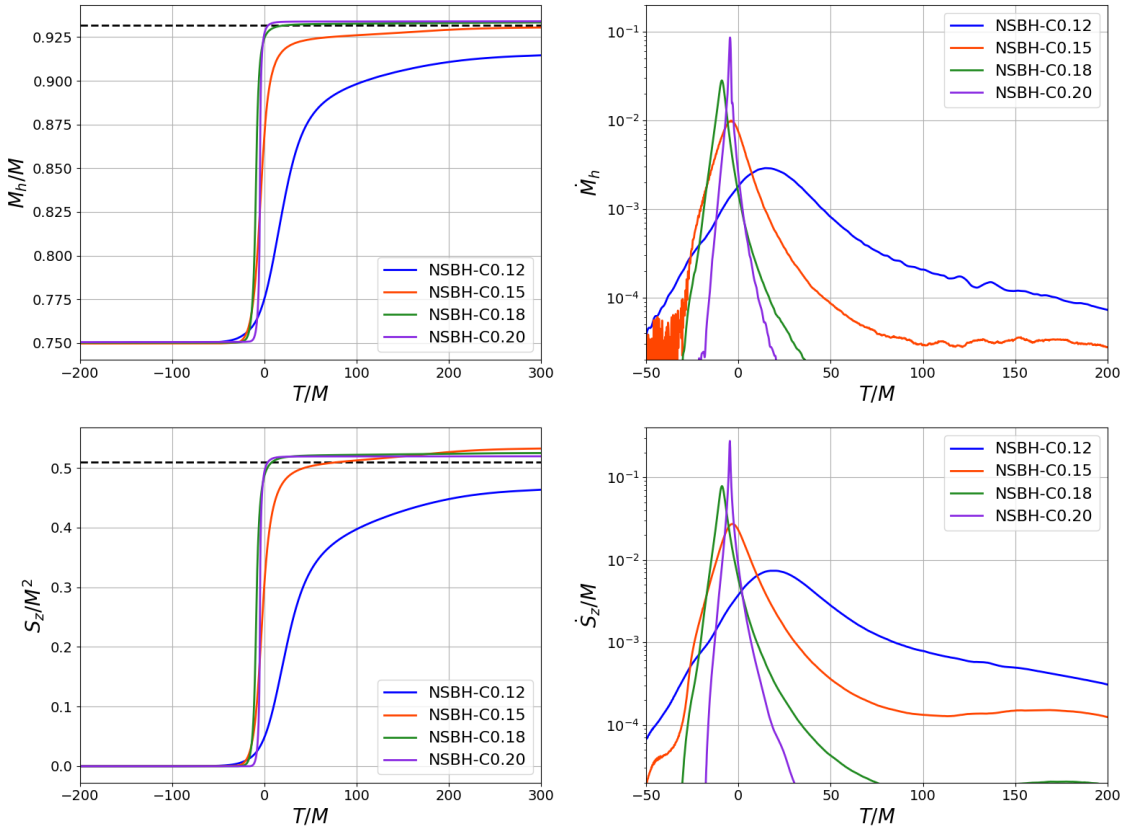

FIGURE 5.3: Panels of the left show the irreducible mass and spin of the black hole as a function of time. Panels on the right show their rates. Time is centered at the peak amplitude of ψ_4 in the retarded frame. The black dashed line represents the final mass and spin of remnant black hole for BBH case.

5.2.2. QUASILOCAL PROPERTIES:

In addition to binary dynamics, the changes in the initial conditions also impact the remnant properties as seen in the previous chapter. Figure 5.3 shows the evolution of mass and spin of the black hole for the four configurations. Panels on the left look at the irreducible mass and spin of the black hole, while panels on the right show their rate of change as a function of time. The dashed lines in black represent the final black hole mass and spin for the corresponding BBH system. From the left panels, we see that mass and spin of the

black hole at the merger increase with the compactness of the star. Remnant black holes of the low compactness configurations have smaller mass and spin values at the time of the merger and grow for an extended period of time due to matter accretion on the black hole horizon. This is shown by the red and blue lines in the figure. Due to strong stellar disruption in NSBH-C0.12, final mass and spin of the remnant black hole remains smaller than BBH as a significant portion of mass (15%) and angular momentum of the neutron star is trapped in the accretion disk instead of black hole. The disk in this case is still unsettled undergoing the process of circularization by the end of the simulation and hence, the final values continue to slowly evolve. In contrast, 95% of stellar material falls into the black hole at the merger in NSBH-C0.15 due to partial disruption of the neutron star resulting in a low mass accretion disk with smaller size. Most of the material in the disk is trapped within ISCO and hence, is eventually engulfed by the black hole which leads to a further increase in its mass and spin values. The behavior of mass and spin growth for NSBH-C0.18 and NSBH-C0.20 is closer to BBH, although, the final mass and spin values in these cases are slightly higher than BBH case.

To understand the higher mass and spin values of NSBH configurations in comparison with BBH, we look at the radiated energy and angular momentum of the system. Figure 5.4 shows the energy dissipated in gravitational waves (left) and the orbital angular momentum of the compact binary system (right) as a function of time. Here, we see that the maximum energy and angular momentum lost in gravitational waves occurs for the BBH case. In contrast, mixed binary system dissipates through two different channels - first via gravitational waves and second via matter outflows in accretion disk and dynamical ejecta. For low compactness cases, stellar disruption leads to a small quadrupole moment and thus weak emission of energy and angular momentum in gravitational waves. As such, most of the energy and angular momentum of the neutron star are trapped in the accretion disk. An increase in stellar compactness reduces the degree of disruption leading to a small or no accretion disk. In these cases, the dissipation of radiated quantities

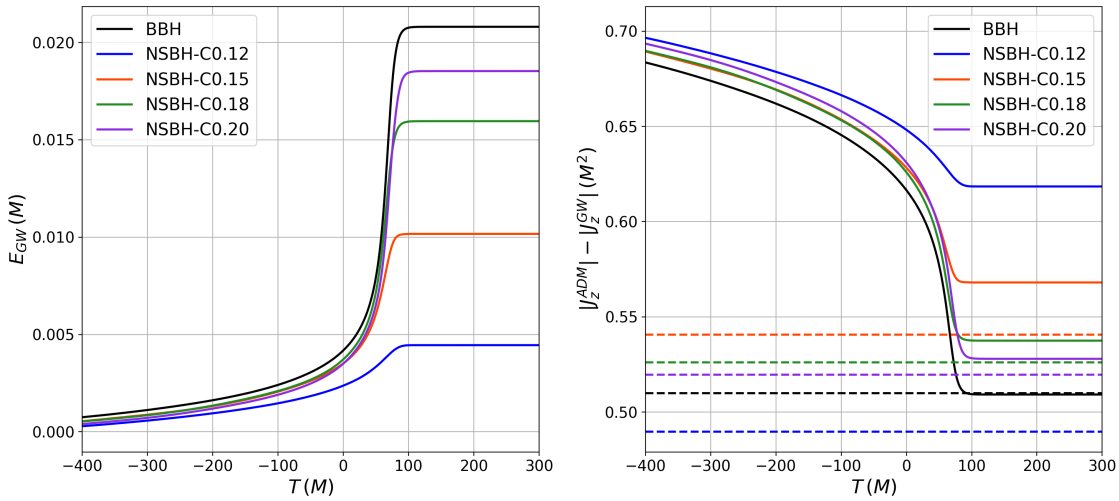

FIGURE 5.4: Panels of the left show the radiated energy in gravitational waves and panel on the right shows the total angular momentum trapped in the system. The dashed lines represents the spin of the final black hole. Time is centered at peak of ψ_4 in the retarded frame.

via gravitational waves increases. However, they never reach the BBH levels. Most of the remaining energy and angular momentum trapped in the matter outflow is eventually converted into the black hole mass and spin via matter accretion after the merger while some are radiated away in gravitationally unbound matter. This explains the gap between the black hole spin and angular momentum of the system in NSBH.

5.2.3. DENSITY OSCILLATION AND COM OFFSETS -

As discussed in section 3.3.4, the imperfections in the initial data introduce artificial excitation of modes in the neutron star leading to oscillations in the central density. Figure 5.5 shows the impact of compactness on the density oscillations. Panel on the left shows the evolution of normalized central density scaled with its initial value and panel on the right shows Fourier transform of this quantity. Two interesting observations can be made here - first, smaller stars (higher compactness) are more stable, while larger stars (lower

TABLE 5.2: Quasilocal Properties Comparison - Here Model represents compact binary configuration, $M_I^{(R)}$ is irreducible mass of remnant black hole, $M_h^{(R)}$ is horizon mass of remnant, $a^{(R)}$ is the dimensionless spin of the remnant, and τ_{22} and $f_{22}^{\rm qnm}$ are the damping time scale and quasinormal frequencies for (2,2) mode based on the accuracy of linear fits. Values are recorded 400M after merger

Model	$M_I^{(R)}$	$M_h^{(R)}$	$a^{(R)}$	τ_{22}	$f_{22}^{\rm qnm}$
BBH-q3	0.9319	0.9712	0.5405	11.6244	0.0831
NSBH-C0.12	0.9165	0.9518	0.5198	9.4548	0.0883
NSBH-C0.15	0.9308	0.9740	0.5629	11.4404	0.0779
NSBH-C0.18	0.9334	0.9749	0.5527	11.3218	0.0783
NSBH-C0.20	0.9341	0.9746	0.5469	11.2875	0.0719

compactness) can have oscillations in the density reaching amplitudes of $\sim 16\%$ about the mean value in some cases. Such oscillations appear close to the fundamental mode frequency as seen from the peak in Fourier spectra. Second, the amplitude of oscillations is not constant and the change itself shows an oscillating trend which suggests excitation of two different modes. This is most apparent in NSBH-C0.20 case. These secondary oscillations are weaker in comparison with the fundamental mode for large stars but become proportionate for more compact stars. We also compute the center of mass offset for each case as they can significantly impact the gravitational waveforms. The values are listed in table 5.3 for each case. We find that while the offset increases in the y-direction with compactness, no clear trend is observed in the x direction. The offsets are also significantly larger than BBH and hence, will be the dominant source of error leading to mode mixing in gravitational waves.

5.2.4. GRAVITATIONAL WAVES

We now look at the gravitational wave signatures. Panels in figure 5.6, show a comparison of real part of ψ_4 (including all the modes) at inclination $\iota = 0$ between BBH and NSBH configuration. Panels from top to bottom are arranged in order of increasing compactness

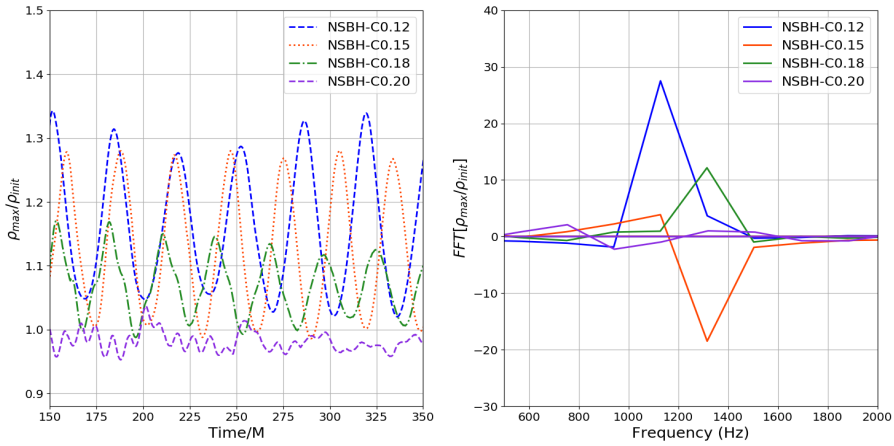

FIGURE 5.5: Central Density Oscillations - Left panel shows oscillations in the central density for each compactness and right panel shows FFT of central density. Here, density is normalized with its initial value.

TABLE 5.3: Merger Statistics Comparison - Here q is the mass ratio, System represents type of compact binary, N is number of orbits, e is eccentricity, T_{Merger} is the time of merger (retarded time corresponding to peak of Ψ_4), Δ_{Merger} is black hole offset from origin at T_{Merger}, M_{ADM} is the ADM mass and J_{ADM} is the ADM angular momentum.

Model	N	$e \times 10^{-3}$	T_{Merger}	Δ_{Merger}	M_{ADM}	J_{ADM}
BBH-q3	6.11	3.85	743	0.0579	0.9917	0.7023
NSBH-C0.12	3.86	1.45	572	0.831	0.9925	0.7023
NSBH-C0.15	5.09	16.6	662	0.782	0.9927	0.7023
NSBH-C0.18	5.33	8.97	658	0.0704	0.9934	0.7023
NSBH-C0.20	4.99	13.1	612	1.16	0.9918	0.7023

and inset zooms on the waveform during inspiral regime between 150M to 450M, after passing of junk radiation. Here, we look at the recomposed ψ_4 including modes from $\ell = 2 : 8$. The merger times for NSBH configurations are typically found to be smaller than BBH case which is also evident from table 5.3. This is expected as stellar deformation leads to an additional correction term in the gravitational potential which has an effect of accelerating the mergers by larger dissipation of gravitational waves [78]. Comparison of merger time across compactness shows more interesting feature - the merger time is

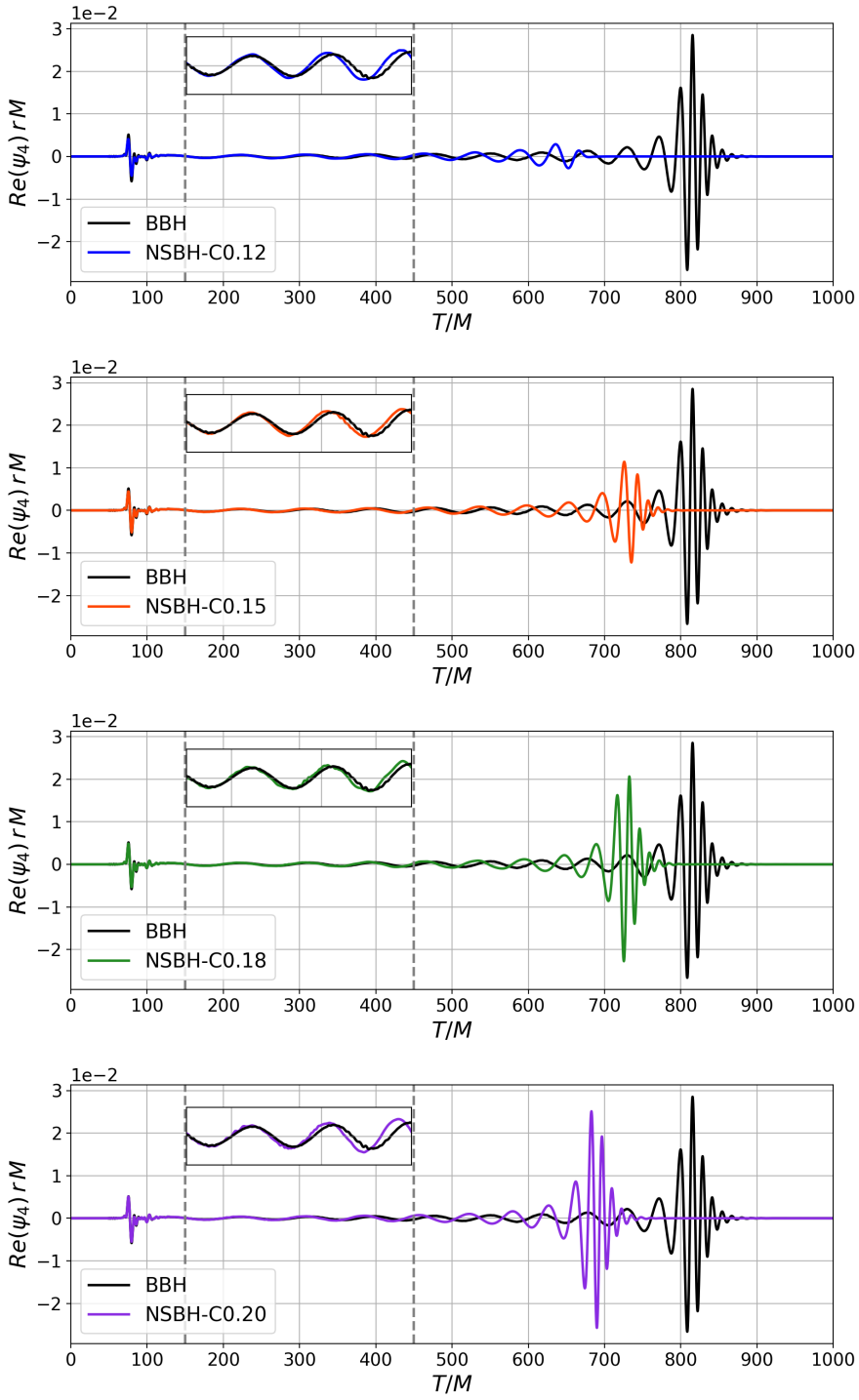

FIGURE 5.6: $Re(\Psi_4)$ Comparison between BBH and NSBH configurations. x axis represents time in units of total mass and y-axis shows the real part of recomposed psi_4 at inclination $\iota = 0$ times the extraction radius, r. Panels from top to bottom represents compactness cases in increasing order. Inset zooms on the initial cycles after junk from $150 - 450M$.

not monotonic functions of compactness but instead peaks at a compactness value and decreases on either side. Similar result was also found for mass ratio 2 case in [85]. This is quite nonintuitive given with increasing compactness, the neutron star behavior would be expected to be closer to a black hole. From the inset we see that for all configurations, BBH and NSBH signals align well until 300 M following which we start to see deviations between the two signals. The degree of deviation differs across the compactness but can also be attributed to other factors like eccentricity or COM offset.

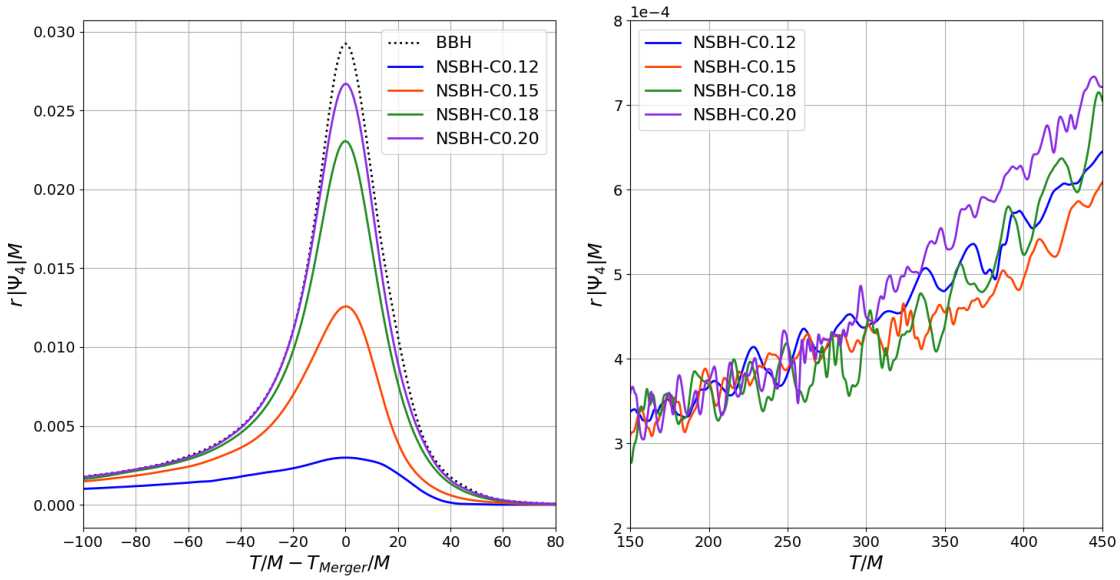

FIGURE 5.7: Ψ_4 Amplitude Comparison between BBH and NSBH configurations. Here, amplitude is computed by combining all configurations for face on case (i.e. inclination $\iota = 0$). Panel on the left shows the ψ_4 amplitude and panel on the right looks at the amplitude oscillations.

Another key difference between the gravitational wave signatures of the two systems are the amplitudes. Figure 5.7 compares the amplitude of ψ_4 for each configuration. x axis shows the time centered at the peak amplitude and y axis shows ψ_4 amplitude for face-on configuration. The amplitude of gravitational waves increases monotonically with compactness of the star but remains smaller than BBH. This is consistent with our observations

of radiated energy and angular momentum. To avoid the impact of mode mixing arising from COM offset, here we have considered all modes in our calculation of amplitude as before [2]. Panel on the right shows the amplitude during the initial time. Due to same mass ratio, all the waveforms almost overlap during the initial cycles and fluctuations are the effect of density oscillations in the star. It can again be seen that maximum oscillations occur for the least compactness system and the oscillations reduce with increasing compactness.

In the previous chapter, we found that the effect of initial configuration in NSBH is reflected in the post merger signal. Given the compactness variation affects the remnant formation in a similar way as mass ratio, it will be interesting to see if such results are observed in this case. Figure 5.8 shows the post-merger signal for the four configurations in each row. Panels on the left and right show the amplitude and phase of (2,1), (2,2), (3,2) and (3,3) modes of ψ_4. The solid line corresponds to the ringdown fits from the perturbation theory which reflect the quasinormal modes of a perturbed rotating black hole. For NSBH-C0.12, due to the presence of accreting matter, the black hole is continuously perturbed leading to the absence of ringdown signature in all the modes similar to mass ratio $q = 2$ case in the previous chapter. This is evident from the disagreement between the fits and the data. For NSBH-C0.15, the ringdown is reflected in the dominant (2,2) and subdominant (3,3) modes, but the fits don't align well for (2,1) and (3,2) modes. The oscillations in the (3,3) mode are distinct signatures of mode mixing. With increasing compactness, clean ringdown signature is observed for NSBH-C0.18 in all modes except (3,3) which is reflected in the mismatch between the fits in both amplitude and phase. In contrast, clean ringdown is observed in NSBH-C0.20 for all modes. Oscillations in the amplitude are due to large COM offset. Observe that the effect of COM offset does not impact the phase and the fits align well with the data.

[2]We note that even in this case, due to COM offset, (2,2) and other modes are found to be impacted by mode mixing which is especially large for system with highest compactness.

Based on the above results, we can draw few interesting conclusions - first, the post-merger signal in a mixed binary system depends on the initial configuration of the binary including stellar compactness and mass ratio. Second, ringdown may be present in certain modes and absent from others depending on the degree of matter accretion and hence, higher modes can be crucial to distinguish between BBH and NSBH systems and systems of different stellar compactness. This can be essential in scenarios where the accretion disk is extremely weak or absent in the final state resulting in the absence of electromagnetic signatures. For example, NSBH-C0.18 and NSBH-C0.20 both lack accretion disk in the final state but have differences in the postmerger signal, especially in the (3,2) mode. It will be interesting to investigate how the degree of accretion is reflected in black hole multipole moments and if it is possible to exploit this connection to identify a relationship between neutron star compactness and ringdown frequencies and damping times.

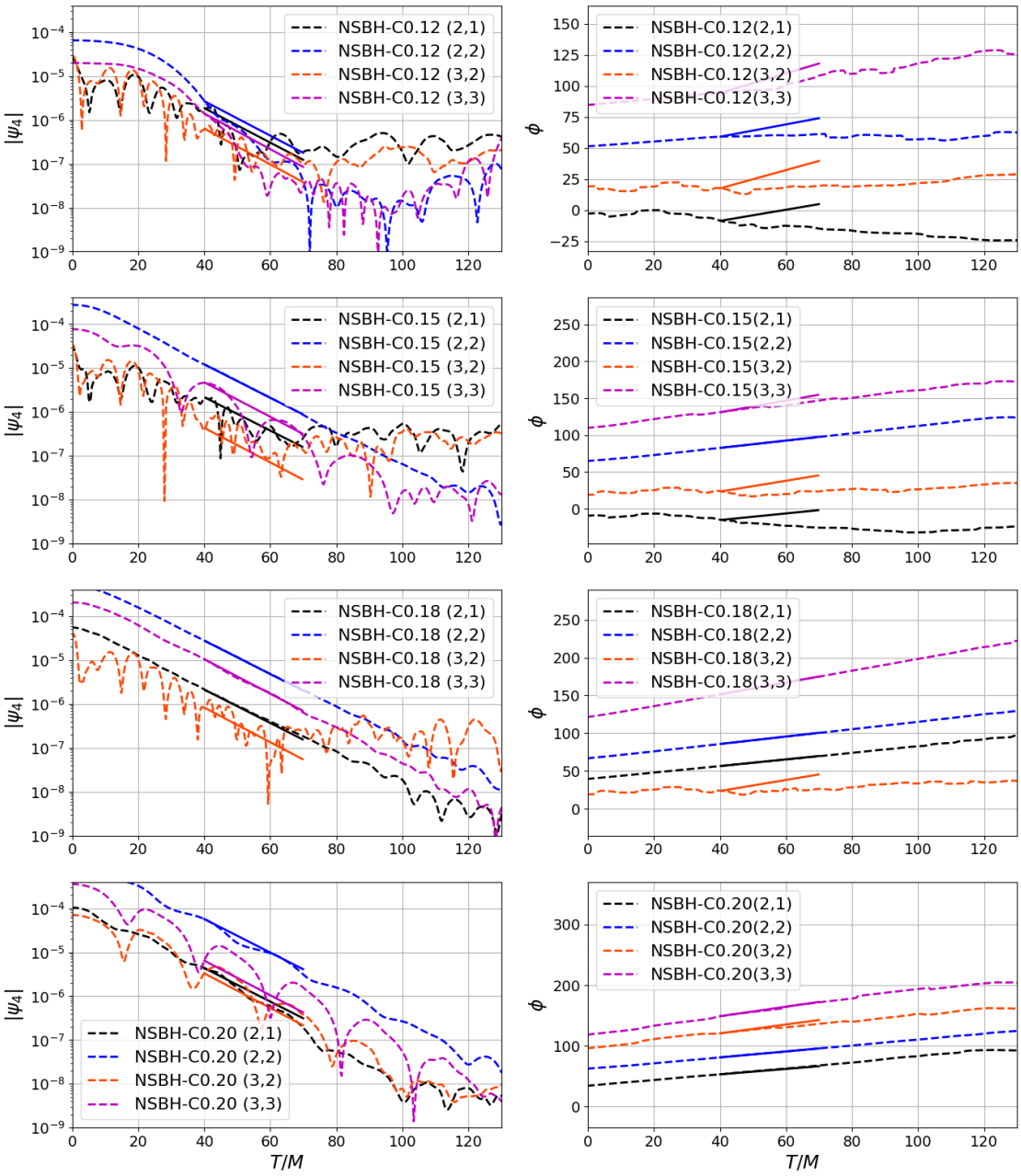

FIGURE 5.8: Post Merger Signals - Panels on left and right show the amplitude and phase of ψ_4 for (2,1), (2,2) and (3,3) modes. x axis represents time centered at peak of amplitude and each row corresponds to $q = 3$ compactness configuration. Solid lines show the QNM fits from perturbation theory [187] while dashed lines show the true data values.

CHAPTER 6

CONCLUSION

6.1. SUMMARY

In this work, we study the mergers of black holes and neutron stars using the tools of numerical relativity. We first explored the initial data formulation and numerical relativity infrastructure required for performing these simulations. We discussed some of the problems with existing code structure, the features of the new initial data pipeline, and the advantages and problems of this initial data method.

Using Maya code with the new initial data pipeline, we performed simulations of neutron star black hole mergers. Our results showed well behaved constraints and convergent results. Comparisons with previously published works showed good agreement in orbital dynamics, remnant properties and gravitational wave signatures. We also investigated the dependence of merger dynamics on the initial configuration and compared our results with binary black hole simulations. In chapter three, we considered three non-spinning mixed binaries with mass ratio $2, 3$ and 5. For mass ratio $q = 2$ systems, we noticed an early disruption of the star before the merger which resulted in the formation of an accretion disk and prolonged growth of the remnant black hole. Due to the continuous perturbation of the final black hole, gravitational waves from this system lacked a clean ringdown. For the same compactness, the dynamics of $q = 3$ system was quite similar, though the disruption occurred closer to ISCO which led to a very low mass accretion

disk. Here, the accreting matter only excites certain (combination of) modes which is reflected in the presence of ringdown signatures in the dominant and some higher order modes inspite of the perturbation. For mass ratio $q = 5$, tidal disruption occurs inside ISCO which barely leaves any matter to form an accretion disk. As a result, the dynamics mimic a binary black hole system and any differences in gravitational wave signatures can only be seen in higher order modes. In such situations, the orientation of the source would be extremely relevant. In chapter five, we continued the investigation of the initial data by studying the effects of stellar compactness on the merger dynamics and gravitational wave signals for mass ratio 3. Although the compactness of a neutron star is constrained by observations, depending on the mass ratio and black hole spin, it can have a considerable impact on the remnant formation ranging from massive disk to a silent black hole. We found that with the increase of neutron star compactness, the degree of tidal disruption is reduced leading to a stronger emission of gravitational waves. The system appears closer to a BBH as reflected in the remnant growth and gravitational wave signatures, although differences were found between BBH and NSBH even for the most compact configuration. Post merger signals showed that stellar compactness also impacts the ringdown in higher order modes and thus, they can be used to decipher the compactness and constrain the equation of state of the neutron star.

We also find some irregularities in the simulation results arising from systematic errors. We investigate the cause and possible effects of these errors in our analysis. Density oscillations in the neutron star were found to cause oscillations in the gravitational wave amplitude. However, such oscillations occur at the fundamental frequency of neutron stars and would not be observable by current detectors. The center of mass offset was shown to have the most dominant effect leading to mode mixing and is currently under investigation. Finally, we analyse the conformal flatness assumption. Using single black hole simulations, we quantified its impact on the black hole mass and spin. We finally constructed fitting formula which would allow us to compute the required modifications in

the initial data to account for the effect of junk radiation. With this, we conclude this work.

6.2. Ongoing and Future Works

The end of one journey is the beginning of the next. Over the past few years, working on various problems has helped us to come up with various new interesting ideas, some to tackle the existing problems in the world of numerical relativity while others more driven towards understanding the dynamics of astrophysical systems through the means of simulations and gravitational wave observations. Let's talk about some of them in the context of neutron star black hole mergers including our current ongoing projects. We first briefly review the problems and propose possible solutions related to the infrastructure and initial data formalism issues seen in chapters II and III and then focus on the astrophysical aspects.

6.2.1. Initial Data

1. Equation of State - The current model inherently assumes gamma-law equation of state which is hidden in the choice of conformal transformations of hydro variables (2.30, 2.31). Gamma law models are optimal for situations where fluid has low density and high temperatures, none of which holds inside a neutron star. Hence, to improve the current model, we need to generalize our initial data method to accommodate realistic equations of state.

2. Conformal Flatness Assumption - Built using the Bowen York approach, our model will also suffer from the same problems as its predecessor to formulate initial data configuration for high-spinning black holes with spins $a > 0.93$ [199, 200]. Conformal flatness also leads to a burst of junk radiation which can impact black holes and neutron star configurations as discussed in chapter 4. One way to tackle this issue is to shift from the conformally flat metric model to conformally Kerr metric which

is more realistic assumption for a rotating black hole. First developed in [201] for binary black hole systems, this approach was shown to overcome the challenges of Bowen-York initial data providing a new way to model binary black holes with extreme spins and significantly low junk radiation [202]. The idea here is to derive the initial guess of conformal metric and trace of curvature using Lorentz boosted Kerr metric or its superposition for binary system. This method can be extended to our case by using superposed solutions of Kerr metric with TOV or rotating star solution to obtain the initial guess of conformal metric and trace of extrinsic curvature.

3. Center of Mass offset - As seen from the analysis in Chapters 3 , we observe significant center of mass offsets for mixed binary simulations primary reason of which is attributed to the problems in the initial data and gauge conditions [194]. The wobbling and drifting of center of mass leads to shift of black hole from the center of detectors (spheres). As a results, the gravitational wave signatures reach earlier on one part of the sphere than the opposite. This leads to additional gauge induced effects like mode mixing [193]. One way to tackle this issue is by accounting for translations and boost in higher order modes [193, 194, 203]. This is an ongoing work.

4. Eccentricity - To reduce the eccentricity of the system, we currently model these binaries using initial data generated from post-Newtonian (PN) methods. However, as shown in Chapter 3, such initial data techniques do not work efficiently with black hole neutron star binaries at separations where relativistic effects start dominating. Further, point particle approximation starts failing for binaries with higher mass ratio and hence, PN methods are not ideal. One clear side effect of using post-Newtonian based initial data is higher eccentricity. A simple method to fix this can be to increase the initial separation but this would also increase the merger time and hence, can be computationally quite expensive. An alternate way is to use iterative methods to tune the momenta of the binary to reduce the eccentricity using methods developed

in [204, 205]. However, recent works of Kyutoku et al. [204] showed that methods developed for eccentricity reduction for BBH systems do not work efficiently for mixed binaries and hence, this problem requires further investigation.

5. Density and Radial Oscillations - Another problem encountered with current simulations are the oscillations in the central density and radius of the star which affect the gravitational wave strain. As these oscillations occur approximately at the fundamental frequencies of neutron star which are much higher than the merger frequencies of mixed binary waveform, they would not be detected by current instruments. However, they can be a source of systematic error for other studies or future detectors. The primary cause of these oscillations arises from two assumptions in our initial data - first the star is assumed as spherically symmetric and second, a static star is artificially boosted. One possible way to reduce the density oscillations is by increasing the separation between the black hole and the neutron star. For larger separations, the impact of tidal forces on star will be low which will reduce the distortions in stellar structure. Hence, the deviations from spherical shape will be small reducing the oscillations in the star.

To understand the problem with equation of state, let us review the conformal transformations of the fluid variables. In the original method proposed in [143], the density and pressure were related to their conformal variables in the following way -

$$\tilde{\rho} = \rho\psi^8 \tag{6.1}$$

$$\tilde{P} = P\psi^8 \tag{6.2}$$

By doing so, we incorrectly assume that the density and pressure are linearly related and thus, share the same conformal transformations, which is only true in case of Gamma Law equation of state. To fix this issue, we must ensure that the equation of state relationship

remains intact from physical to conformal space. Towards this, we propose a modified approach to the initial data. Let us assume the following conformal transformations for hydro variables -

$$\tilde{\rho}_H = \rho_H \tag{6.3}$$

$$\tilde{S}^i = S^i \psi^{10} \tag{6.4}$$

$$\tilde{u}^a = u^a \psi^{10} \tag{6.5}$$

$$\tilde{\alpha} = \alpha \psi^{-10} \tag{6.6}$$

$$\beta^i = 0 \tag{6.7}$$

The transformations for spacetime variables are given as in section 2.3.1. As we conformally transform only a constant time hypersurface, it is possible to choose distinct transformation laws for $g_{tt} = \alpha^2$ and $g_{ij} = \gamma_{ij}$. From these transformations, it can be easily seen that $W = \alpha u^t = \tilde{\alpha}\tilde{u}^t = \tilde{W}$. Note that inner products do not remain preserved under the above transformations and hence, $W = \sqrt{1 + \gamma_{ij} u^i u^j}$ in the physical space and $\tilde{W} = \sqrt{1 + \psi^{-16} \tilde{\gamma}_{ij} \tilde{u}^i \tilde{u}^j}$ in the conformal space. As a first check, let us look at the transformations of density and pressure.

$$S^i = (\rho + P) W u^i \tag{6.8}$$

$$= (\rho + P) \tilde{W} \tilde{u}^i \psi^{-10} \tag{6.9}$$

$$= (\tilde{\rho} + \tilde{P}) \tilde{W} \tilde{u}^i \psi^{-10} \equiv \tilde{S}^i \psi^{-10} \tag{6.10}$$

From the equality of the second and third steps, it can be seen that $\tilde{\rho} = \rho$ and $\tilde{P} = P$. As the density and pressure remain conformally invariant under the new transformations, any equation of state relations defined in the physical space would also hold well in the conformal space.

Let us now look at the constraint equations under the new transformations. As we

continue with CTT formulation, the LHS of both the equations remain unchanged. The new equations are then given as

$$8\tilde{D}^2\psi + \psi^{-7}\tilde{A}_{ij}\tilde{A}^{ij} = -16\pi\psi^5\tilde{\rho}_H \tag{6.11}$$

$$(\tilde{\nabla}_L\mathcal{W})^i = 8\pi\tilde{S}^i \tag{6.12}$$

Note that the only major change occurs in the RHS of Hamiltonian Constraint. As the momentum constraint remains unchanged, we can now follow the same method as described in [143]. Let's focus on the non-spinning case for which the momentum density in physical and conformal space can be modelled as

$$\tilde{S}^i = \tilde{P}^i\tilde{\sigma}(r) \tag{6.13}$$

$$S^i = \tilde{P}^i\tilde{\sigma}(r) \tag{6.14}$$

To determine the model parameter, $\tilde{P}^i$, we can look at the ADM momentum measurable by an observer at infinity (and hence, can be approximated by post-Newtonian theories). The ADM momentum is defined as

$$P^i_{ADM} = \frac{1}{8\pi}\int_{\partial\Sigma_\infty} dS_j \left(K^{ij} - \gamma^{ij}K\right) \tag{6.15}$$

One can alternately look at the ADM momenta in the conformal space. As the physical space is asymptotically flat, $\psi \to 1$ as $r \to \infty$ and hence, the ADM momentum will remain

the same in both the spaces. Transforming the RHS integral to conformal space, we get

$$P^i_{ADM} = \frac{1}{8\pi}\int_{\partial\Sigma_\infty} dS_j \left(\tilde{K}^{ij} - \tilde{\gamma}^{ij}\tilde{K}\right) \tag{6.16}$$

$$= \frac{1}{8\pi}\int_{\Sigma_\infty} dV\sqrt{\eta}\tilde{D}_j \left(\tilde{K}^{ij} - \tilde{\gamma}^{ij}\tilde{K}\right) \tag{6.17}$$

$$= \frac{1}{8\pi}\int_{\Sigma_\infty} dV\sqrt{\eta}\tilde{D}_j\tilde{A}^{ij} \tag{6.18}$$

$$= \int_{\Sigma_\infty} dV\tilde{S}^i \tag{6.19}$$

$$= \int_{\Sigma_\infty} dV\tilde{P}^i\tilde{\sigma}(r) \tag{6.20}$$

$$\Rightarrow P^i_{ADM} = \tilde{P}^i\int_{\Sigma_\infty} dV\sigma(r) \tag{6.21}$$

We can now set $P^i_{ADM} = \tilde{P}^i$ by imposing the following normalization condition

$$\int_{\Sigma_\infty} dV\sigma(r) = 1 \tag{6.22}$$

The reason to shift to conformal space can be understood using the following intuition - unlike physical space, the conformal space has zero intrinsic curvature ($\tilde{\gamma}_{ij} = \eta_{ij}$) and hence, the parallel transport of vectors along the null geodesics would not change the vector's magnitude or orientation. Hence, the ADM momentum in the source frame and one at infinity can be be related. As the condition of normalization remains same, repeating the steps from [143] we will end up with the same solution for traceless extrinsic curvature.

To determine $\tilde{\sigma}(r)$, we use the definition of conformal momentum density -

$$\tilde{S}^i \equiv (\tilde{\rho} + \tilde{P})\tilde{W}\tilde{u}^i = \tilde{P}\tilde{\sigma}(r) \tag{6.23}$$

Setting

$$\tilde{\sigma}(r) = \frac{\tilde{\rho} + \tilde{P}}{\tilde{\kappa}} \tag{6.24}$$

We get

$$\tilde{P}^i = \tilde{\kappa}\tilde{W}\tilde{u}^i \tag{6.25}$$

Here, $\tilde{\kappa} = 4\pi \int_0^\infty drr^2(\tilde{\rho} + \tilde{P})$ which is obtained from the normalization condition 6.22. The Lorentz Factor $\tilde{W}^i = W^i$ where

$$W^i = \left[\frac{1}{2} \pm \sqrt{1 + \frac{4\gamma_{ij}S^iS^j}{(\rho + P)^2}}\right]^{1/2} \tag{6.26}$$

While this method requires testing and comparison with the original simulations, using this method would hopefully fix the problems with polytropic equations of state and allow us to extend our model to any realistic equation of state.

6.2.2. EVOLUTION CODE -

In addition to the above problems, the coding infrastructure can also be upgraded. Running spacetime and hydro evolutions simultaneously are expensive and hence, we optimized our code and shifted to fourth order finite differencing. Further, our current hydrodynamics code is limited to the fourth-order scheme. Using lower order methods would incur larger numerical errors which can affect the analysis for future gravitational wave detectors. Hence, we need faster evolution codes which can support higher order differencing schemes, especially in hydrodynamics.

Lastly, in our analysis we looked at various sources of systematic errors in the waveforms arising from center of mass offsets and density oscillations which currently dominate the random errors. But, a more thorough error analysis in the waveform templates is required once the systematic errors can be controlled. In particular, the higher order modes during the post-merger phase are more significantly impacted by numerical noise and hence, any studies analysing the post-merger signals would need to account for these errors.

6.3. ASTROPHYSICS

The mergers of mixed binary systems are highly dynamical with several interesting processes occurring within extremely short durations of time. For low mass ratio systems, as the star gets closer to the black hole, the tidal forces induce mass shedding and distort the stellar structure. Once the outer crust of the star is disrupted leaving the inner core exposed, the strong flow of material is observed from the stellar core to the black hole leading to complete stellar disruption. During this process, the angular momentum transports to the leftover material which circularizes around the black hole forming an accretion disk. For nonspinning systems with higher mass ratios or more compact stars, the star already enters the ISCO before it can be disrupted. As a result of this, most of the star gets engulfed by the black hole leaving only traces of stellar material outside the black hole which is not sufficient to form a strong disk.

While the general process is well understood, the details of each step are still one of the hot topics of research. Various works have examined the relationship between initial parameters like black hole and neutron star spins, magnetic fields and equation of state, and the formation of accretion disks and jets (check [78, 206] reviews and references therein). Some groups have also analysed the possible electromagnetic signatures and underlying physical processes occurring at relativistic scales [74]. As a lot of these studies have been discussed in the introduction, we refer the interested readers to chapter 1 for a more detailed summary of the current research in this field.

Here, we would like to focus on some of the direct applications/extensions of our current study and other research ideas which arose from this work. The first direct extension of this work will be for spinning black holes and neutron stars with magnetic fields. From previous studies [58, 59, 94–100], it has been shown that the stellar disruption process is highly sensitive to black hole spin. In the presence of highly spinning black holes, it is possible to observe stellar disruptions even for mass ratio as large as $q \sim 10$. Relatively

less studied are the effects of neutron star spins which also are extremely interesting. Due to spin support, rotating stars are more immune to tidal effects of the star making them gravitationally less bound [207]. Further, the spin of neutron stars can also affect the ISCO radius [208]. Ruiz et al. [192] analyzed a few configurations of polytropic spinning neutron stars with mass ratio 3 and 5 showed that neutron star spins can affect the accretion disk mass, dynamical ejecta, relativistic jets and induce dephasing in gravitational wave signatures. However, at present, very few studies have been conducted in this region of parameter space and while the general understanding of the effects of BH spin on NSBH mergers exist, detailed explorations are required to understand the effects of neutron star spin on the dynamics of BHNS mergers and their gravitational wave signatures. Comparisons of BHNS with spinning neutron stars and similar BBH or DNS can be extremely relevant to obtain the identifying marks in gravitational wave signatures and accurately determine the source of the signal in the absence of electromagnetic signals and for systems in mass gap regions such as [17, 18].

Another interesting parameter space to explore would be of eccentric mixed binaries which can arise from dynamical processes in dense stellar clusters [209]. Most studies of NSBH mergers have focused into quasi-circular regime while only a few studies [100, 207, 209] have investigated hyperbolic encounters. The gravitational wave signatures of eccentric mixed binaries can vary significantly and eccentricity can also impact the properties of accretion disk, mass of dynamical ejecta and orbital dynamics of the system [209]. It will be interesting to explore how changes in mass ratio, equation of state and spins of binaries affect the dynamics of eccentric systems.

It will also be ideal to create a catalog of NSBH waveforms which can be used for developing new gravitational waveforms. The parameter space of NSBH is larger than a BBH system and hence, it requires more number of simulations to accurately model and test the waveform approximants. At present, only a few groups have successfully managed to perform numerical simulations of NSBH systems most of which are not publicly

available. Further, with recent detections of NSBH like candidates, the need to improve NSBH approximants has become more urgent. Hence, it will be ideal to create an open source gravitational wave bank of NSBH simulations which can be accessible to the research community. NSBH models can also be extremely useful to model higher mass ratio systems due to smaller relative differences in the size, in comparison to the black hole. For very high mass ratio systems, neutron stars are predicted to not disrupt and hence, there will not be any differences between a BBH and NSBH signature. For such high mass ratio, one can use NSBH models to tune and test BBH models.

Lastly, although theoretical models help us understand the nature of the system and make important predictions, it is important to test if such predictions can be tested with current and future detectors. As a part of ongoing work, we are currently testing the effectiveness of approximate waveform models used for parameter estimation to distinguish between NSBH and BBH signals by performing parameter estimation studies on NSBH software injections. We inject mixed binary signals with varying mass ratio and compactness for different inclinations and SNR and recover the parameters using BBH, tidal, and NSBH waveform models. This study will help us reveal the regions of parameter space where it is possible to distinguish mixed binaries from binary black hole systems. Apart from waveform models, as seen in chapter 3, this can also depend on the initial parameters of the binary, the SNR, and inclination of received signal. It will also help us to independently analyse the performance of the current NSBH waveform approximants in the late inspiral, merger and post merger regions where tidal effects are most dominant.

REFERENCES

[1] B. P. Abbott et al. "Observation of Gravitational Waves from a Binary Black Hole Merger". In: *Phys. Rev. Lett.* 116.6 (2016), p. 061102. DOI: 10.1103/PhysRevLett.116.061102. arXiv: 1602.03837 [gr-qc].

[2] J. Aasi et al. "Advanced LIGO". In: *Class. Quant. Grav.* 32 (2015), p. 074001. DOI: 10.1088/0264-9381/32/7/074001. arXiv: 1411.4547 [gr-qc].

[3] F. Acernese et al. "Advanced Virgo: a second-generation interferometric gravitational wave detector". In: *Class. Quant. Grav.* 32.2 (2015), p. 024001. DOI: 10.1088/0264-9381/32/2/024001. arXiv: 1408.3978 [gr-qc].

[4] T. Akutsu et al. "KAGRA: 2.5 Generation Interferometric Gravitational Wave Detector". In: *Nature Astron.* 3.1 (2019), pp. 35–40. DOI: 10.1038/s41550-018-0658-y. arXiv: 1811.08079 [gr-qc].

[5] Aaron Buikema et al. "Sensitivity and performance of the Advanced LIGO detectors in the third observing run". In: *Phys. Rev. D* 102.6 (2020), p. 062003. DOI: 10.1103/PhysRevD.102.062003. arXiv: 2008.01301 [astro-ph.IM].

[6] B. P. Abbott et al. "Prospects for Observing and Localizing Gravitational-Wave Transients with Advanced LIGO, Advanced Virgo and KAGRA". In: *Living Rev. Rel.* 21.1 (2018), p. 3. DOI: 10.1007/s41114-018-0012-9. arXiv: 1304.0670 [gr-qc].

[7] B. P. Abbott et al. "GW150914: The Advanced LIGO Detectors in the Era of First Discoveries". In: *Phys. Rev. Lett.* 116.13 (2016), p. 131103. DOI: 10.1103/PhysRevLett.116.131103. arXiv: 1602.03838 [gr-qc].

[8] B. P. Abbott et al. "GW151226: Observation of Gravitational Waves from a 22-Solar-Mass Binary Black Hole Coalescence". In: *Phys. Rev. Lett.* 116.24 (2016), p. 241103. DOI: 10.1103/PhysRevLett.116.241103. arXiv: 1606.04855 [gr-qc].

[9] B. . P. . Abbott et al. "GW170608: Observation of a 19-solar-mass Binary Black Hole Coalescence". In: *Astrophys. J.* 851.2 (2017), p. L35. DOI: 10.3847/2041-8213/aa9f0c. arXiv: 1711.05578 [astro-ph.HE].

[10] B. P. Abbott et al. "GW170814: A Three-Detector Observation of Gravitational Waves from a Binary Black Hole Coalescence". In: *Phys. Rev. Lett.* 119.14 (2017), p. 141101. DOI: 10.1103/PhysRevLett.119.141101. arXiv: 1709.09660 [gr-qc].

[11] B. P. Abbott et al. "GW170817: Observation of Gravitational Waves from a Binary Neutron Star Inspiral". In: *Phys. Rev. Lett.* 119.16 (2017), p. 161101. DOI: 10.1103/PhysRevLett.119.161101. arXiv: 1710.05832 [gr-qc].

[12] Benjamin P. Abbott et al. "GW170104: Observation of a 50-Solar-Mass Binary Black Hole Coalescence at Redshift 0.2". In: *Phys. Rev. Lett.* 118.22 (2017). [Erratum: Phys.Rev.Lett. 121, 129901 (2018)], p. 221101. DOI: 10.1103/PhysRevLett.118.221101. arXiv: 1706.01812 [gr-qc].

[13] B. P. Abbott et al. "GWTC-1: A Gravitational-Wave Transient Catalog of Compact Binary Mergers Observed by LIGO and Virgo during the First and Second Observing Runs". In: *Phys. Rev. X* 9.3 (2019), p. 031040. DOI: 10.1103/PhysRevX.9.031040. arXiv: 1811.12907 [astro-ph.HE].

[14] B. P. Abbott et al. "GW190425: Observation of a Compact Binary Coalescence with Total Mass $\sim 3.4 M_{\odot}$". In: *Astrophys. J. Lett.* 892.1 (2020), p. L3. DOI: 10.3847/2041-8213/ab75f5. arXiv: 2001.01761 [astro-ph.HE].

[15] R. Abbott et al. "GW190412: Observation of a Binary-Black-Hole Coalescence with Asymmetric Masses". In: *Phys. Rev. D* 102.4 (2020), p. 043015. DOI: 10.1103/PhysRevD.102.043015. arXiv: 2004.08342 [astro-ph.HE].

[16] R. Abbott et al. "GW190521: A Binary Black Hole Merger with a Total Mass of $150 M_{\odot}$". In: *Phys. Rev. Lett.* 125.10 (2020), p. 101102. DOI: 10.1103/PhysRevLett.125.101102. arXiv: 2009.01075 [gr-qc].

[17] R. Abbott et al. “GW190814: Gravitational Waves from the Coalescence of a 23 Solar Mass Black Hole with a 2.6 Solar Mass Compact Object”. In: *Astrophys. J. Lett.* 896.2 (2020), p. L44. DOI: 10.3847/2041-8213/ab960f. arXiv: 2006.12611 [astro-ph.HE].

[18] R. Abbott et al. “GWTC-2: Compact Binary Coalescences Observed by LIGO and Virgo During the First Half of the Third Observing Run”. In: (Oct. 2020). arXiv: 2010.14527 [gr-qc].

[19] Benjamin P Abbott et al. “Exploring the Sensitivity of Next Generation Gravitational Wave Detectors”. In: *Class. Quant. Grav.* 34.4 (2017), p. 044001. DOI: 10.1088/1361-6382/aa51f4. arXiv: 1607.08697 [astro-ph.IM].

[20] M. Punturo et al. “The Einstein Telescope: A third-generation gravitational wave observatory”. In: *Class. Quant. Grav.* 27 (2010). Ed. by Fulvio Ricci, p. 194002. DOI: 10.1088/0264-9381/27/19/194002.

[21] Pau Amaro-Seoane et al. “Laser Interferometer Space Antenna”. In: (Feb. 2017). arXiv: 1702.00786 [astro-ph.IM].

[22] B. P. Abbott et al. “Properties of the Binary Black Hole Merger GW150914”. In: *Phys. Rev. Lett.* 116.24 (2016), p. 241102. DOI: 10.1103/PhysRevLett.116.241102. arXiv: 1602.03840 [gr-qc].

[23] B. P. Abbott et al. “Binary Black Hole Population Properties Inferred from the First and Second Observing Runs of Advanced LIGO and Advanced Virgo”. In: *Astrophys. J. Lett.* 882.2 (2019), p. L24. DOI: 10.3847/2041-8213/ab3800. arXiv: 1811.12940 [astro-ph.HE].

[24] B. P. Abbott et al. “Properties of the binary neutron star merger GW170817”. In: *Phys. Rev. X* 9.1 (2019), p. 011001. DOI: 10.1103/PhysRevX.9.011001. arXiv: 1805.11579 [gr-qc].

[25] R. Abbott et al. “Population Properties of Compact Objects from the Second LIGO-Virgo Gravitational-Wave Transient Catalog”. In: (Oct. 2020). arXiv: 2010.14533 [astro-ph.HE].

[26] R. Abbott et al. “Properties and Astrophysical Implications of the 150 $M_{\odot}$ Binary Black Hole Merger GW190521”. In: *Astrophys. J. Lett.* 900.1 (2020), p. L13. DOI: 10.3847/2041-8213/aba493. arXiv: 2009.01190 [astro-ph.HE].

[27] William A. Fowler and F. Hoyle. “Neutrino Processes and Pair Formation in Massive Stars and Supernovae.” In: 9 (Dec. 1964), p. 201. DOI: 10.1086/190103.

[28] Z. Barkat, G. Rakavy, and N. Sack. “Dynamics of Supernova Explosion Resulting from Pair Formation”. In: 18.10 (Mar. 1967), pp. 379–381. DOI: 10.1103/PhysRevLett.18.379.

[29] G. Rakavy and G. Shaviv. “Instabilities in Highly Evolved Stellar Models”. In: 148 (June 1967), p. 803. DOI: 10.1086/149204.

[30] B. P. Abbott et al. “Tests of general relativity with GW150914”. In: *Phys. Rev. Lett.* 116.22 (2016). [Erratum: Phys.Rev.Lett. 121, 129902 (2018)], p. 221101. DOI: 10.1103/PhysRevLett.116.221101. arXiv: 1602.03841 [gr-qc].

[31] B. P. Abbott et al. “Tests of General Relativity with GW170817”. In: *Phys. Rev. Lett.* 123.1 (2019), p. 011102. DOI: 10.1103/PhysRevLett.123.011102. arXiv: 1811.00364 [gr-qc].

[32] B. P. Abbott et al. “Tests of General Relativity with the Binary Black Hole Signals from the LIGO-Virgo Catalog GWTC-1”. In: *Phys. Rev. D* 100.10 (2019), p. 104036. DOI: 10.1103/PhysRevD.100.104036. arXiv: 1903.04467 [gr-qc].

[33] R. Abbott et al. “Tests of General Relativity with Binary Black Holes from the second LIGO-Virgo Gravitational-Wave Transient Catalog”. In: (Oct. 2020). arXiv: 2010.14529 [gr-qc].

[34] B. P. Abbott et al. "A gravitational-wave standard siren measurement of the Hubble constant". In: *Nature* 551.7678 (2017), pp. 85–88. DOI: 10.1038/nature24471. arXiv: 1710.05835 [astro-ph.CO].

[35] B. P. Abbott et al. "A gravitational-wave measurement of the Hubble constant following the second observing run of Advanced LIGO and Virgo". In: (Aug. 2019). arXiv: 1908.06060 [astro-ph.CO].

[36] M. Soares-Santos et al. "First Measurement of the Hubble Constant from a Dark Standard Siren using the Dark Energy Survey Galaxies and the LIGO/Virgo Binary–Black-hole Merger GW170814". In: *Astrophys. J. Lett.* 876.1 (2019), p. L7. DOI: 10.3847/2041-8213/ab14f1. arXiv: 1901.01540 [astro-ph.CO].

[37] Charles D. Bailyn et al. "The Mass distribution of stellar black holes". In: *Astrophys. J.* 499 (1998), p. 367. DOI: 10.1086/305614. arXiv: astro-ph/9708032.

[38] Feryal Özel et al. "The Black Hole Mass Distribution in the Galaxy". In: 725.2 (Dec. 2010), pp. 1918–1927. DOI: 10.1088/0004-637X/725/2/1918. arXiv: 1006.2834 [astro-ph.GA].

[39] Will M. Farr et al. "The Mass Distribution of Stellar-mass Black Holes". In: 741.2, 103 (Nov. 2011), p. 103. DOI: 10.1088/0004-637X/741/2/103. arXiv: 1011.1459 [astro-ph.GA].

[40] Feryal Özel and Paulo Freire. "Masses, Radii, and the Equation of State of Neutron Stars". In: *Ann. Rev. Astron. Astrophys.* 54 (2016), pp. 401–440. DOI: 10.1146/annurev-astro-081915-023322. arXiv: 1603.02698 [astro-ph.HE].

[41] Shilpa Kastha et al. "Testing the multipole structure of compact binaries using gravitational wave observations". In: *Phys. Rev. D* 98.12 (2018), p. 124033. DOI: 10.1103/PhysRevD.98.124033. arXiv: 1809.10465 [gr-qc].

[42] Shilpa Kastha et al. "Testing the multipole structure and conservative dynamics of compact binaries using gravitational wave observations: The spinning case". In: *Phys. Rev. D* 100.4 (2019), p. 044007. DOI: 10.1103/PhysRevD.100.044007. arXiv: 1905.07277 [gr-qc].

[43] Siddharth Dhanpal et al. "A no-hair test for binary black holes". In: *Phys. Rev. D* 99.10 (2019), p. 104056. DOI: 10.1103/PhysRevD.99.104056. arXiv: 1804.03297 [gr-qc].

[44] Tousif Islam et al. "Testing the no-hair nature of binary black holes using the consistency of multipolar gravitational radiation". In: *Phys. Rev. D* 101.2 (2020), p. 024032. DOI: 10.1103/PhysRevD.101.024032. arXiv: 1910.14259 [gr-qc].

[45] Markus Heusler. *Black Hole Uniqueness Theorems*. Cambridge Lecture Notes in Physics. Cambridge University Press, 1996. DOI: 10.1017/CBO9780511661396.

[46] B. Carter. "Axisymmetric Black Hole Has Only Two Degrees of Freedom". In: *Phys. Rev. Lett.* 26 (1971), pp. 331–333. DOI: 10.1103/PhysRevLett.26.331.

[47] Solomon Endlich et al. "An effective formalism for testing extensions to General Relativity with gravitational waves". In: *JHEP* 09 (2017), p. 122. DOI: 10.1007/JHEP09(2017)122. arXiv: 1704.01590 [gr-qc].

[48] Eugeny Babichev and Richard Brito. "Black holes in massive gravity". In: *Class. Quant. Grav.* 32 (2015), p. 154001. DOI: 10.1088/0264-9381/32/15/154001. arXiv: 1503.07529 [gr-qc].

[49] Carlos Herdeiro, Eugen Radu, and Helgi Rúnarsson. "Kerr black holes with Proca hair". In: *Class. Quant. Grav.* 33.15 (2016), p. 154001. DOI: 10.1088/0264-9381/33/15/154001. arXiv: 1603.02687 [gr-qc].

[50] Eugeny Babichev, Christos Charmousis, and Antoine Lehébel. "Black holes and stars in Horndeski theory". In: *Class. Quant. Grav.* 33.15 (2016), p. 154002. DOI: 10.1088/0264-9381/33/15/154002. arXiv: 1604.06402 [gr-qc].

[51] Burkhard Kleihaus, Jutta Kunz, and Francisco Navarro-Lerida. "Rotating black holes with non-Abelian hair". In: *Class. Quant. Grav.* 33.23 (2016), p. 234002. DOI: 10.1088/0264-9381/33/23/234002. arXiv: 1609.07357 [hep-th].

[52] Robert Benkel, Thomas P. Sotiriou, and Helvi Witek. "Black hole hair formation in shift-symmetric generalised scalar-tensor gravity". In: *Class. Quant. Grav.* 34.6 (2017), p. 064001. DOI: 10.1088/1361-6382/aa5ce7. arXiv: 1610.09168 [gr-qc].

[53] Andrea Maselli, Leonardo Gualtieri, and Valeria Ferrari. "Constraining the equation of state of nuclear matter with gravitational wave observations: Tidal deformability and tidal disruption". In: *Phys. Rev. D* 88.10 (2013), p. 104040. DOI: 10.1103/PhysRevD.88.104040. arXiv: 1310.5381 [gr-qc].

[54] Prayush Kumar, Michael Pürrer, and Harald P. Pfeiffer. "Measuring neutron star tidal deformability with Advanced LIGO: a Bayesian analysis of neutron star - black hole binary observations". In: *Phys. Rev. D* 95.4 (2017), p. 044039. DOI: 10.1103/PhysRevD.95.044039. arXiv: 1610.06155 [gr-qc].

[55] V. Ferrari, L. Gualtieri, and F. Pannarale. "Neutron star tidal disruption in mixed binaries: the imprint of the equation of state". In: *Phys. Rev. D* 81 (2010), p. 064026. DOI: 10.1103/PhysRevD.81.064026. arXiv: 0912.3692 [gr-qc].

[56] Matthew D. Duez et al. "Equation of state effects in black hole-neutron star mergers". In: *Class. Quant. Grav.* 27 (2010). Ed. by Christian D. Ott, C. J. Pethick, and Luciano Rezzolla, p. 114106. DOI: 10.1088/0264-9381/27/11/114106. arXiv: 0912.3528 [astro-ph.HE].

[57] Koutarou Kyutoku, Masaru Shibata, and Keisuke Taniguchi. "Gravitational waves from nonspinning black hole-neutron star binaries: dependence on equations of state". In: *Phys. Rev. D* 82 (2010). [Erratum: Phys.Rev.D 84, 049902 (2011)], p. 044049. DOI: 10.1103/PhysRevD.82.044049. arXiv: 1008.1460 [astro-ph.HE].

[58] Koutarou Kyutoku et al. "Gravitational waves from spinning black hole-neutron star binaries: dependence on black hole spins and on neutron star equations of state". In: *Phys. Rev. D* 84 (2011), p. 064018. DOI: 10.1103/PhysRevD.84.064018. arXiv: 1108.1189 [astro-ph.HE].

[59] Kyohei Kawaguchi et al. "Black hole-neutron star binary merger: Dependence on black hole spin orientation and equation of state". In: *Phys. Rev. D* 92.2 (2015), p. 024014. DOI: 10.1103/PhysRevD.92.024014. arXiv: 1506.05473 [astro-ph.HE].

[60] Benjamin D. Lackey et al. "Extracting equation of state parameters from black hole-neutron star mergers. I. Nonspinning black holes". In: *Phys. Rev. D* 85 (2012), p. 044061. DOI: 10.1103/PhysRevD.85.044061. arXiv: 1109.3402 [astro-ph.HE].

[61] Benjamin D. Lackey et al. "Extracting equation of state parameters from black hole-neutron star mergers: aligned-spin black holes and a preliminary waveform model". In: *Phys. Rev. D* 89.4 (2014), p. 043009. DOI: 10.1103/PhysRevD.89.043009. arXiv: 1303.6298 [gr-qc].

[62] M. B. Davies et al. "Merging Neutron Stars. I. Initial Results for Coalescence of Noncorotating Systems". In: 431 (Aug. 1994), p. 742. DOI: 10.1086/174525. arXiv: astro-ph/9401032 [astro-ph].

[63] M. Ruffert et al. "Coalescing neutron stars - a step towards physical models. II. Neutrino emission, neutron tori, and gamma-ray bursts." In: 319 (Mar. 1997), pp. 122–153. arXiv: astro-ph/9606181 [astro-ph].

[64] J. M. Lattimer and D. N. Schramm. "Black-Hole-Neutron-Star Collisions". In: 192 (Sept. 1974), p. L145. DOI: 10.1086/181612.

[65] David Eichler et al. “Nucleosynthesis, Neutrino Bursts and Gamma-Rays from Coalescing Neutron Stars”. In: *Nature* 340 (1989), pp. 126–128. DOI: 10.1038/340126a0.

[66] F. K. Thielemann et al. “Neutron Star Mergers and Nucleosynthesis of Heavy Elements”. In: *Ann. Rev. Nucl. Part. Sci.* 67 (2017), pp. 253–274. DOI: 10.1146/annurev-nucl-101916-123246. arXiv: 1710.02142 [astro-ph.HE].

[67] Y. Z. Qian and S. E. Woosley. “Nucleosynthesis in neutrino driven winds: 1. The Physical conditions”. In: *Astrophys. J.* 471 (1996), pp. 331–351. DOI: 10.1086/177973. arXiv: astro-ph/9611094.

[68] B. D. Metzger et al. “Electromagnetic counterparts of compact object mergers powered by the radioactive decay of r-process nuclei”. In: 406.4 (Aug. 2010), pp. 2650–2662. DOI: 10.1111/j.1365-2966.2010.16864.x. arXiv: 1001.5029 [astro-ph.HE].

[69] Rodrigo Fernández and Brian D. Metzger. “Electromagnetic Signatures of Neutron Star Mergers in the Advanced LIGO Era”. In: *Ann. Rev. Nucl. Part. Sci.* 66 (2016), pp. 23–45. DOI: 10.1146/annurev-nucl-102115-044819. arXiv: 1512.05435 [astro-ph.HE].

[70] R. D. Blandford and R. L. Znajek. “Electromagnetic extraction of energy from Kerr black holes.” In: 179 (May 1977), pp. 433–456. DOI: 10.1093/mnras/179.3.433.

[71] Vasileios Paschalidis, Milton Ruiz, and Stuart L. Shapiro. “Relativistic Simulations of Black Hole–neutron Star Coalescence: the jet Emerges”. In: *Astrophys. J. Lett.* 806.1 (2015), p. L14. DOI: 10.1088/2041-8205/806/1/L14. arXiv: 1410.7392 [astro-ph.HE].

[72] M. Brett Deaton et al. “Black Hole-Neutron Star Mergers with a Hot Nuclear Equation of State: Outflow and Neutrino-Cooled Disk for a Low-Mass, High-Spin Case”. In: *Astrophys. J.* 776 (2013), p. 47. DOI: 10.1088/0004-637X/776/1/47. arXiv: 1304.3384 [astro-ph.HE].

[73] Ehud Nakar and Tsvi Piran. "Radio Remnants of Compact Binary Mergers - the Electromagnetic Signal that will follow the Gravitational Waves". In: *Nature* 478 (2011), pp. 82–84. DOI: 10.1038/nature10365. arXiv: 1102.1020 [astro-ph.HE].

[74] Masaru Shibata and Kenta Hotokezaka. "Merger and Mass Ejection of Neutron-Star Binaries". In: *Ann. Rev. Nucl. Part. Sci.* 69 (2019), pp. 41–64. DOI: 10.1146/annurev-nucl-101918-023625. arXiv: 1908.02350 [astro-ph.HE].

[75] Luc Blanchet. "Gravitational radiation from postNewtonian sources and inspiraling compact binaries". In: *Living Rev. Rel.* 5 (2002), p. 3. DOI: 10.12942/lrr-2002-3. arXiv: gr-qc/0202016.

[76] P. C. Peters and J. Mathews. "Gravitational radiation from point masses in a Keplerian orbit". In: *Phys. Rev.* 131 (1963), pp. 435–439. DOI: 10.1103/PhysRev.131.435.

[77] P. C. Peters. "Gravitational Radiation and the Motion of Two Point Masses". In: *Phys. Rev.* 136 (1964), B1224–B1232. DOI: 10.1103/PhysRev.136.B1224.

[78] Masaru Shibata and Keisuke Taniguchi. "Coalescence of Black Hole-Neutron Star Binaries". In: *Living Rev. Rel.* 14 (2011), p. 6. DOI: 10.12942/lrr-2011-6.

[79] J. M. Lattimer and D. N. Schramm. "Black-Hole-Neutron-Star Collisions". In: 192 (Sept. 1974), p. L145. DOI: 10.1086/181612.

[80] Keisuke Taniguchi et al. "Relativistic black hole-neutron star binaries in quasiequilibrium: Effects of the black hole excision boundary condition". In: *Phys. Rev. D* 77 (2008), p. 044003. DOI: 10.1103/PhysRevD.77.044003. arXiv: 0710.5169 [gr-qc].

[81] V. Ferrari, L. Gualtieri, and F. Pannarale. "A Semi-relativistic Model for Tidal Interactions in BH-NS Coalescing Binaries". In: *Class. Quant. Grav.* 26 (2009), p. 125004. DOI: 10.1088/0264-9381/26/12/125004. arXiv: 0801.2911 [astro-ph].

[82] Leslie G. Fishbone. "The Relativistic Roche Problem. I. Equilibrium Theory for a Body in Equatorial, Circular Orbit around a Kerr Black Hole". In: 185 (Oct. 1973), pp. 43–68. DOI: 10.1086/152395.

[83] Masaki Ishii, Masaru Shibata, and Yasushi Mino. "Black hole tidal problem in the Fermi normal coordinates". In: *Phys. Rev. D* 71 (2005), p. 044017. DOI: 10.1103/PhysRevD.71.044017. arXiv: gr-qc/0501084.

[84] Paul Wiggins and Dong Lai. "Tidal interaction between a fluid star and a Kerr black hole: Relativistic Roche-Riemann model". In: *Astrophys. J.* 532 (2000), p. 530. DOI: 10.1086/308565. arXiv: astro-ph/9907365.

[85] Masaru Shibata et al. "Gravitational waves from black hole-neutron star binaries I: Classification of waveforms". In: *Phys. Rev. D* 79 (2009). [Erratum: Phys.Rev.D 85, 127502 (2012)], p. 044030. DOI: 10.1103/PhysRevD.79.044030. arXiv: 0902.0416 [gr-qc].

[86] Zachariah B. Etienne et al. "Fully General Relativistic Simulations of Black Hole-Neutron Star Mergers". In: *Phys. Rev. D* 77 (2008), p. 084002. DOI: 10.1103/PhysRevD.77.084002. arXiv: 0712.2460 [astro-ph].

[87] Matthew D. Duez et al. "Evolving black hole-neutron star binaries in general relativity using pseudospectral and finite difference methods". In: *Phys. Rev. D* 78 (10 2008), p. 104015. DOI: 10.1103/PhysRevD.78.104015.

[88] Masaru Shibata. "Merger of black hole-neutron star binaries: Nonspinning black hole case". In: *Phys. Rev. D* 74 (12 2006), p. 121503. DOI: 10.1103/PhysRevD.74.121503.

[89] Masaru Shibata and Koji Uryu. "Merger of black hole-neutron star binaries in full general relativity". In: *Class. Quant. Grav.* 24 (12 2007). Ed. by Manuela Campanelli and Luciano Rezzolla, S125–S138. DOI: 10.1088/0264-9381/24/12/S09. arXiv: astro-ph/0611522.

[90] F. Foucart et al. “Numerical simulations of neutron star-black hole binaries in the near-equal-mass regime”. In: *Phys. Rev. D* 99.10 (12 2019), p. 103025. DOI: 10.1103/PhysRevD.99.103025. arXiv: 1903.09166 [astro-ph.HE].

[91] Lawrence E. Kidder. “Coalescing binary systems of compact objects to postNewtonian 5/2 order. 5. Spin effects”. In: *Phys. Rev. D* 52 (12 1995), pp. 821–847. DOI: 10.1103/PhysRevD.52.821. arXiv: gr-qc/9506022.

[92] Manuela Campanelli, C. O. Lousto, and Yosef Zlochower. “Spin-orbit interactions in black-hole binaries”. In: *Phys. Rev. D* 74 (12 2006), p. 084023. DOI: 10.1103/PhysRevD.74.084023. arXiv: astro-ph/0608275.

[93] Lawrence E. Kidder, Clifford M. Will, and Alan G. Wiseman. “Spin effects in the inspiral of coalescing compact binaries”. In: *Phys. Rev. D* 47.10 (12 1993), pp. 4183–4187. DOI: 10.1103/PhysRevD.47.R4183. arXiv: gr-qc/9211025.

[94] Zachariah B. Etienne et al. “General relativistic simulations of black-hole-neutron-star mergers: Effects of black-hole spin”. In: *Phys. Rev. D* 79 (12 2009), p. 044024. DOI: 10.1103/PhysRevD.79.044024. arXiv: 0812.2245 [astro-ph].

[95] Francois Foucart et al. “Black hole-neutron star mergers for 10 solar mass black holes”. In: *Phys. Rev. D* 85 (12 2012), p. 044015. DOI: 10.1103/PhysRevD.85.044015. arXiv: 1111.1677 [gr-qc].

[96] Francois Foucart et al. “Black hole-neutron star mergers: effects of the orientation of the black hole spin”. In: *Phys. Rev. D* 83 (12 2011), p. 024005. DOI: 10.1103/PhysRevD.83.024005. arXiv: 1007.4203 [astro-ph.HE].

[97] Francois Foucart et al. “Black hole-neutron star mergers at realistic mass ratios: Equation of state and spin orientation effects”. In: *Phys. Rev. D* 87 (12 2013), p. 084006. DOI: 10.1103/PhysRevD.87.084006. arXiv: 1212.4810 [gr-qc].

[98] Francois Foucart et al. "Dynamical ejecta from precessing neutron star-black hole mergers with a hot, nuclear-theory based equation of state". In: *Class. Quant. Grav.* 34.4 (12 2017), p. 044002. DOI: 10.1088/1361-6382/aa573b. arXiv: 1611.01159 [astro-ph.HE].

[99] Milton Ruiz, Stuart L. Shapiro, and Antonios Tsokaros. "Jet launching from binary black hole-neutron star mergers: Dependence on black hole spin, binary mass ratio and magnetic field orientation". In: *Phys. Rev. D* 98.12 (12 2018), p. 123017. DOI: 10.1103/PhysRevD.98.123017. arXiv: 1810.08618 [astro-ph.HE].

[100] William E. East, Frans Pretorius, and Branson C. Stephens. "Eccentric black hole-neutron star mergers: effects of black hole spin and equation of state". In: *Phys. Rev. D* 85 (12 2012), p. 124009. DOI: 10.1103/PhysRevD.85.124009. arXiv: 1111.3055 [astro-ph.HE].

[101] Jonathan E. Thompson et al. "Modeling the gravitational wave signature of neutron star black hole coalescences". In: *Phys. Rev. D* 101.12 (12 2020), p. 124059. DOI: 10.1103/PhysRevD.101.124059. arXiv: 2002.08383 [gr-qc].

[102] Andrew Matas et al. "Aligned-spin neutron-star–black-hole waveform model based on the effective-one-body approach and numerical-relativity simulations". In: *Phys. Rev. D* 102.4 (12 2020), p. 043023. DOI: 10.1103/PhysRevD.102.043023. arXiv: 2004.10001 [gr-qc].

[103] Richard L. Arnowitt, Stanley Deser, and Charles W. Misner. "The Dynamics of general relativity". In: *Gen. Rel. Grav.* 40 (12 2008), pp. 1997–2027. DOI: 10.1007/s10714-008-0661-1. arXiv: gr-qc/0405109.

[104] Thomas W. Baumgarte and Stuart L. Shapiro. *Numerical Relativity: Solving Einstein's Equations on the Computer*. Vol. 74. Cambridge University Press, 2010, p. 121503. DOI: 10.1017/CBO9781139193344.

[105] James W. York Jr. "Conformatlly invariant orthogonal decomposition of symmetric tensors on Riemannian manifolds and the initial value problem of general relativity". In: *J. Math. Phys.* 14 (12 1973), pp. 456–464. DOI: 10.1063/1.1666338.

[106] James W. York Jr. "Conformal 'thin sandwich' data for the initial-value problem". In: *Phys. Rev. Lett.* 82 (12 1999), pp. 1350–1353. DOI: 10.1103/PhysRevLett.82.1350. arXiv: gr-qc/9810051.

[107] Harald P. Pfeiffer and James W. York Jr. "Uniqueness and non-uniqueness in the Einstein constraints". In: *Phys. Rev. Lett.* 95 (12 2005), p. 091101. DOI: 10.1103/PhysRevLett.95.091101. arXiv: gr-qc/0504142.

[108] André Lichnerowicz. "L'intégration des équations de la gravitation relativiste et le problème des *n* corps". In: *J. Math. Pures Appl. (9)* 23 (12 1944), pp. 37–63. ISSN: 0021-7824. DOI: 10.1103/PhysRevD.74.121503.

[109] Yvonne Choquet-Bruhat. "The Problem of Constraints in General Relativity: Solution of the Lichnerowicz Equation". In: *Differential Geometry and Relativity: A Volume in Honour of André Lichnerowicz on His 60th Birthday*. Ed. by M. Cahen and M. Flato. Vol. 74. Dordrecht: Springer Netherlands, 1976, pp. 225–235. ISBN: 978-94-010-1508-0. DOI: 10.1007/978-94-010-1508-0_20.

[110] Jeffrey M. Bowen and Jr. York James W. "Time asymmetric initial data for black holes and black hole collisions". In: *Phys. Rev. D* 21 (12 1980), pp. 2047–2056. DOI: 10.1103/PhysRevD.21.2047.

[111] Marcus Ansorg, Bernd Bruegmann, and Wolfgang Tichy. "A Single-domain spectral method for black hole puncture data". In: *Phys. Rev. D* 70 (12 2004), p. 064011. DOI: 10.1103/PhysRevD.70.064011. arXiv: gr-qc/0404056.

[112] Steven Brandt and Bernd Bruegmann. "A Simple construction of initial data for multiple black holes". In: *Phys. Rev. Lett.* 78 (12 1997), pp. 3606–3609. DOI: 10.1103/PhysRevLett.78.3606. arXiv: gr-qc/9703066.

[113] Koutarou Kyutoku, Masaru Shibata, and Keisuke Taniguchi. "Quasiequilibrium states of black hole-neutron star binaries in the moving-puncture framework". In: *Phys. Rev. D* 79 (12 2009), p. 124018. DOI: 10.1103/PhysRevD.79.124018. arXiv: 0906.0889 [gr-qc].

[114] Wolfgang Tichy. "The initial value problem as it relates to numerical relativity". In: *Rept. Prog. Phys.* 80.2 (12 2017), p. 026901. DOI: 10.1088/1361-6633/80/2/026901. arXiv: 1610.03805 [gr-qc].

[115] L. Jens Papenfort et al. "A new public code for initial data of unequal-mass, spinning compact-object binaries". In: *Phys. Rev. D* 74 (12 Mar. 2021), p. 121503. DOI: 10.1103/PhysRevD.74.121503. arXiv: 2103.09911 [gr-qc].

[116] Wolfgang Tichy et al. "Constructing binary neutron star initial data with high spins, high compactnesses, and high mass ratios". In: *Phys. Rev. D* 100.12 (12 2019), p. 124046. DOI: 10.1103/PhysRevD.100.124046. arXiv: 1910.09690 [gr-qc].

[117] Wolfgang Tichy. "A New numerical method to construct binary neutron star initial data". In: *Class. Quant. Grav.* 26 (12 2009), p. 175018. DOI: 10.1088/0264-9381/26/17/175018. arXiv: 0908.0620 [gr-qc].

[118] Niclas Moldenhauer et al. "Initial data for binary neutron stars with adjustable eccentricity". In: *Phys. Rev. D* 90.8 (12 2014), p. 084043. DOI: 10.1103/PhysRevD.90.084043. arXiv: 1408.4136 [gr-qc].

[119] Tim Dietrich, Serguei Ossokine, and Katy Clough. "Full 3D numerical relativity simulations of neutron star–boson star collisions with BAM". In: *Class. Quant. Grav.* 36.2 (12 2019), p. 025002. DOI: 10.1088/1361-6382/aaf43e. arXiv: 1807.06959 [gr-qc].

[120] Antonios Tsokaros, Kōji Uryū, and Luciano Rezzolla. "New code for quasiequilibrium initial data of binary neutron stars: Corotating, irrotational, and slowly spinning systems". In: *Phys. Rev. D* 91.10 (12 2015), p. 104030. DOI: 10.1103/PhysRevD.91.104030. arXiv: 1502.05674 [gr-qc].

[121] Antonios Tsokaros et al. "Initial-data contribution to the error budget of gravitational waves from neutron-star binaries". In: *Phys. Rev. D* 94.4 (12 2016), p. 044049. DOI: 10.1103/PhysRevD.94.044049. arXiv: 1605.07205 [gr-qc].

[122] Antonios Tsokaros et al. "Constant circulation sequences of binary neutron stars and their spin characterization". In: *Phys. Rev. D* 98.12 (12 2018), p. 124019. DOI: 10.1103/PhysRevD.98.124019. arXiv: 1809.08237 [gr-qc].

[123] Francois Foucart et al. "Initial data for black hole-neutron star binaries: A Flexible, high-accuracy spectral method". In: *Phys. Rev. D* 77 (12 2008), p. 124051. DOI: 10.1103/PhysRevD.77.124051. arXiv: 0804.3787 [gr-qc].

[124] Harald Paul Pfeiffer. "Initial data for black hole evolutions". PhD thesis. Cornell U., 2005, p. 121503. DOI: 10.1103/PhysRevD.74.121503. arXiv: gr-qc/0510016.

[125] Nick Tacik et al. "Initial data for black hole–neutron star binaries, with rotating stars". In: *Class. Quant. Grav.* 33.22 (12 2016), p. 225012. DOI: 10.1088/0264-9381/33/22/225012. arXiv: 1607.07962 [gr-qc].

[126] Nick Tacik et al. "Binary Neutron Stars with Arbitrary Spins in Numerical Relativity". In: *Phys. Rev. D* 92.12 (12 2015). [Erratum: Phys.Rev.D 94, 049903 (2016)], p. 124012. DOI: 10.1103/PhysRevD.92.124012. arXiv: 1508.06986 [gr-qc].

[127] Serguei Ossokine et al. "Improvements to the construction of binary black hole initial data". In: *Class. Quant. Grav.* 32 (12 2015), p. 245010. DOI: 10.1088/0264-9381/32/24/245010. arXiv: 1506.01689 [gr-qc].

[128] Keisuke Taniguchi, Eric Gourgoulhon, and Silvano Bonazzola. "Quasiequilibrium sequences of synchronized and irrotational binary neutron stars in general relativity. 2. Newtonian limits". In: *Phys. Rev. D* 64 (12 2001), p. 064012. DOI: 10.1103/PhysRevD.64.064012. arXiv: gr-qc/0103041.

[129] Keisuke Taniguchi and Eric Gourgoulhon. "Equilibrium sequences of synchronized and irrotational binary systems composed of different mass stars in newtonian gravity". In: *Phys. Rev. D* 65 (12 2002), p. 044027. DOI: 10.1103/PhysRevD.65.044027. arXiv: astro-ph/0108086.

[130] Keisuke Taniguchi and Eric Gourgoulhon. "Quasiequilibrium sequences of synchronized and irrotational binary neutron stars in general relativity. 3. Identical and different mass stars with gamma = 2". In: *Phys. Rev. D* 66 (12 2002), p. 104019. DOI: 10.1103/PhysRevD.66.104019. arXiv: gr-qc/0207098.

[131] Philippe Grandclement, Eric Gourgoulhon, and Silvano Bonazzola. "Binary black holes in circular orbits. 2. Numerical methods and first results". In: *Phys. Rev. D* 65 (12 2002), p. 044021. DOI: 10.1103/PhysRevD.65.044021. arXiv: gr-qc/0106016.

[132] Philippe Grandclement. "Accurate and realistic initial data for black hole-neutron star binaries". In: *Phys. Rev. D* 74 (12 2006). [Erratum: Phys.Rev.D 75, 129903 (2007)], p. 124002. DOI: 10.1103/PhysRevD.74.124002. arXiv: gr-qc/0609044.

[133] Eric Gourgoulhon et al. "Quasiequilibrium sequences of synchronized and irrotational binary neutron stars in general relativity: 1. Method and tests". In: *Phys. Rev. D* 63 (12 2001), p. 064029. DOI: 10.1103/PhysRevD.63.064029. arXiv: gr-qc/0007028.

[134] Thomas W. Baumgarte. "Puncture black hole initial data in the conformal thin-sandwich formalism". In: *Classical and Quantum Gravity* 28.21, 215003 (12 Nov. 2011), p. 215003. DOI: 10.1088/0264-9381/28/21/215003. arXiv: 1108.3550 [gr-qc].

[135] Thomas W. Baumgarte and Stuart L. Shapiro. "On the numerical integration of Einstein's field equations". In: *Phys. Rev. D* 59 (12 1999), p. 024007. DOI: 10.1103/PhysRevD.59.024007. arXiv: gr-qc/9810065.

[136] Masaru Shibata and Takashi Nakamura. "Evolution of three-dimensional gravitational waves: Harmonic slicing case". In: *Phys. Rev. D* 52 (12 1995), pp. 5428–5444. DOI: 10.1103/PhysRevD.52.5428.

[137] Takashi Nakamura, Kenichi Oohara, and Yasufumi Kojima. "General Relativistic Collapse to Black Holes and Gravitational Waves from Black Holes". In: *Progress of Theoretical Physics Supplement* 90 (12 Jan. 1987), pp. 1–218. ISSN: 0375-9687. DOI: 10.1143/PTPS.90.1. eprint: https://academic.oup.com/ptps/article-pdf/doi/10.1143/PTPS.90.1/5201911/90-1.pdf.

[138] Sebastiano Bernuzzi and David Hilditch. "Constraint violation in free evolution schemes: Comparing BSSNOK with a conformal decomposition of Z4". In: *Phys. Rev. D* 81 (12 2010), p. 084003. DOI: 10.1103/PhysRevD.81.084003. arXiv: 0912.2920 [gr-qc].

[139] David Hilditch et al. "Compact binary evolutions with the Z4c formulation". In: *Phys. Rev. D* 88 (12 2013), p. 084057. DOI: 10.1103/PhysRevD.88.084057. arXiv: 1212.2901 [gr-qc].

[140] Milton Ruiz, David Hilditch, and Sebastiano Bernuzzi. "Constraint preserving boundary conditions for the Z4c formulation of general relativity". In: *Phys. Rev. D* 83 (12 2011), p. 024025. DOI: 10.1103/PhysRevD.83.024025. arXiv: 1010.0523 [gr-qc].

[141] Andreas Weyhausen, Sebastiano Bernuzzi, and David Hilditch. "Constraint damping for the Z4c formulation of general relativity". In: *Phys. Rev. D* 85 (12 2012), p. 024038. DOI: 10.1103/PhysRevD.85.024038. arXiv: 1107.5539 [gr-qc].

[142] Zhoujian Cao and David Hilditch. “Numerical stability of the Z4c formulation of general relativity”. In: *Phys. Rev. D* 85 (12 2012), p. 124032. DOI: 10.1103/PhysRevD.85.124032. arXiv: 1111.2177 [gr-qc].

[143] Michael Clark and Pablo Laguna. “Bowen-York Type Initial Data for Binaries with Neutron Stars”. In: *Phys. Rev. D* 94.6 (12 2016), p. 064058. DOI: 10.1103/PhysRevD.94.064058. arXiv: 1606.04881 [gr-qc].

[144] Steven R. Brandt et al. *The Einstein Toolkit*. Version The "Turing" release, ET_2020_05. To find out more, visit http://einsteintoolkit.org. May 2020. DOI: 10.5281/zenodo.3866075.

[145] Erik Schnetter, Badri Krishnan, and Florian Beyer. “Introduction to dynamical horizons in numerical relativity”. In: *Phys. Rev. D* 74 (12 2006), p. 024028. DOI: 10.1103/PhysRevD.74.024028. arXiv: gr-qc/0604015.

[146] Daniel Pook-Kolb et al. “Horizons in a binary black hole merger I: Geometry and area increase”. In: *Phys. Rev. D* 74 (12 June 2020), p. 121503. DOI: 10.1103/PhysRevD.74.121503. arXiv: 2006.03939 [gr-qc].

[147] Christopher Evans et al. “Inside the Final Black Hole: Puncture and Trapped Surface Dynamics”. In: *Class. Quant. Grav.* 37.15 (12 2020), 15LT02. DOI: 10.1088/1361-6382/ab9c6b. arXiv: 2004.11979 [gr-qc].

[148] Daniel Pook-Kolb et al. “Self-intersecting marginally outer trapped surfaces”. In: *Phys. Rev. D* 100.8 (12 2019), p. 084044. DOI: 10.1103/PhysRevD.100.084044. arXiv: 1907.00683 [gr-qc].

[149] Daniel Pook-Kolb et al. “Interior of a Binary Black Hole Merger”. In: *Phys. Rev. Lett.* 123.17 (12 2019), p. 171102. DOI: 10.1103/PhysRevLett.123.171102. arXiv: 1903.05626 [gr-qc].

[150] A. Einstein. “Die Grundlage der allgemeinen Relativitätstheorie”. In: *Annalen der Physik* 354.7 (12 1916), pp. 769–822. DOI: https://doi.org/10.1002/andp.19163540702. eprint: https://onlinelibrary.wiley.com/doi/pdf/10.1002/andp.19163540702.

[151] Hans Stephani et al. *Exact solutions of Einstein's field equations*. Vol. 74. Cambridge Monographs on Mathematical Physics. Cambridge: Cambridge Univ. Press, 2003, p. 121503. ISBN: 978-0-521-46702-5, 978-0-511-05917-9. DOI: 10.1017/CBO9780511535185.

[152] Robert A. Eisenstein. “Numerical Relativity and the Discovery of Gravitational Waves”. In: *Annalen Phys.* 531.8 (12 2019), p. 1800348. DOI: 10.1002/andp.201800348. arXiv: 1804.07415 [gr-qc].

[153] Michael Christopher Clark. “Bowen-Type initial data for simulationso of neutron star binary systems”. PhD thesis. Georgia Institute of Technology, May 2016, p. 121503. DOI: 10.1103/PhysRevD.74.121503.

[154] Jeffrey M. Bowen. “General form for the longitudinal momentum of a spherically symmetric source”. In: *General Relativity and Gravitation* 11.3 (12 1979), pp. 227–231. ISSN: 1572-9532. DOI: 10.1007/BF00762132.

[155] Philipp Mösta et al. “GRHydro: A new open source general-relativistic magneto-hydrodynamics code for the Einstein Toolkit”. In: *Class. Quant. Grav.* 31 (12 2014), p. 015005. DOI: 10.1088/0264-9381/31/1/015005. arXiv: 1304.5544 [gr-qc].

[156] Zachariah B. Etienne et al. “IllinoisGRMHD: An Open-Source, User-Friendly GRMHD Code for Dynamical Spacetimes”. In: *Class. Quant. Grav.* 32 (12 2015), p. 175009. DOI: 10.1088/0264-9381/32/17/175009. arXiv: 1501.07276 [astro-ph.HE].

[157] Tom Goodale et al. “The Cactus Framework and Toolkit: Design and Applications”. In: *High Performance Computing for Computational Science — VECPAR 2002*. Ed. by José M. L. M. Palma et al. Vol. 74. Berlin, Heidelberg: Springer Berlin Heidelberg, 2003, pp. 197–227. ISBN: 978-3-540-36569-3. DOI: 10.1103/PhysRevD.74.121503.

[158] Kenny Higginbotham et al. “Coping with spurious radiation in binary black hole simulations”. In: *Phys. Rev. D* 100.8 (12 2019), p. 081501. DOI: 10.1103/PhysRevD.100.081501. arXiv: 1907.00027 [gr-qc].

[159] Manuela Campanelli et al. “Accurate evolutions of orbiting black-hole binaries without excision”. In: *Phys. Rev. Lett.* 96 (12 2006), p. 111101. DOI: 10.1103/PhysRevLett.96.111101. arXiv: gr-qc/0511048.

[160] Miguel Alcubierre et al. “Gauge conditions for long term numerical black hole evolutions without excision”. In: *Phys. Rev. D* 67 (12 2003), p. 084023. DOI: 10.1103/PhysRevD.67.084023. arXiv: gr-qc/0206072.

[161] James R. van Meter et al. “How to move a black hole without excision: Gauge conditions for the numerical evolution of a moving puncture”. In: *Phys. Rev. D* 73 (12 2006), p. 124011. DOI: 10.1103/PhysRevD.73.124011. arXiv: gr-qc/0605030.

[162] Frank Loffler et al. “The Einstein Toolkit: A Community Computational Infrastructure for Relativistic Astrophysics”. In: *Class. Quant. Grav.* 29 (12 2012), p. 115001. DOI: 10.1088/0264-9381/29/11/115001. arXiv: 1111.3344 [gr-qc].

[163] Luca Baiotti et al. “A new three-dimensional general-relativistic hydrodynamics code”. In: *Mem. Soc. Ast. It.* 1 (12 2003), S210. DOI: 10.1103/PhysRevD.74.121503. arXiv: 1004.3849 [gr-qc].

[164] P. Colella and Paul R. Woodward. “The Piecewise Parabolic Method (PPM) for Gas-Dynamical Simulations”. In: *Journal of Computational Physics* 54 (12 Sept. 1984), pp. 174–201. DOI: 10.1016/0021-9991(84)90143-8.

[165] Rosa Donat and Antonio Marquina. “Capturing Shock Reflections: An Improved Flux Formula”. In: *Journal of Computational Physics* 125.1 (12 1996), pp. 42–58. ISSN: 0021-9991. DOI: https://doi.org/10.1006/jcph.1996.0078.

[166] Jonathan Thornburg. "A Fast apparent horizon finder for three-dimensional Cartesian grids in numerical relativity". In: *Class. Quant. Grav.* 21 (12 2004), pp. 743–766. DOI: 10.1088/0264-9381/21/2/026. arXiv: gr-qc/0306056.

[167] Kenta Hotokezaka et al. "Mass ejection from the merger of binary neutron stars". In: 87.2, 024001 (12 Jan. 2013), p. 024001. DOI: 10.1103/PhysRevD.87.024001. arXiv: 1212.0905 [astro-ph.HE].

[168] Koutarou Kyutoku et al. "Dynamical mass ejection from black hole-neutron star binaries". In: *Phys. Rev. D* 92 (12 2015), p. 044028. DOI: 10.1103/PhysRevD.92.044028. arXiv: 1502.05402 [astro-ph.HE].

[169] Olaf Dreyer et al. "Introduction to isolated horizons in numerical relativity". In: *Phys. Rev. D* 67 (12 2003), p. 024018. DOI: 10.1103/PhysRevD.67.024018. arXiv: gr-qc/0206008.

[170] Ezra Newman and Roger Penrose. "An Approach to gravitational radiation by a method of spin coefficients". In: *J. Math. Phys.* 3 (12 1962), pp. 566–578. DOI: 10.1063/1.1724257.

[171] Abhay Ashtekar, Stephen Fairhurst, and Badri Krishnan. "Isolated horizons: Hamiltonian evolution and the first law". In: *Phys. Rev. D* 62 (12 2000), p. 104025. DOI: 10.1103/PhysRevD.62.104025. arXiv: gr-qc/0005083.

[172] Miguel Zilhão and Frank Löffler. "An Introduction to the Einstein Toolkit". In: *Int. J. Mod. Phys. A* 28 (12 2013). Ed. by V. Cardoso et al., p. 1340014. DOI: 10.1142/S0217751X13400149. arXiv: 1305.5299 [gr-qc].

[173] Christian Reisswig and Denis Pollney. "Notes on the integration of numerical relativity waveforms". In: *Class. Quant. Grav.* 28 (12 2011), p. 195015. DOI: 10.1088/0264-9381/28/19/195015. arXiv: 1006.1632 [gr-qc].

[174] Milton Ruiz et al. “Multipole expansions for energy and momenta carried by gravitational waves”. In: *Gen. Rel. Grav.* 40 (12 2008), p. 2467. DOI: 10.1007/s10714-007-0570-8. arXiv: 0707.4654 [gr-qc].

[175] Bhavesh Khamesra, Miguel Gracia-Linares, and Pablo Laguna. “Black Hole - Neutron Star Binary Mergers: The Imprint of Tidal Deformations and Debris”. In: *Phys. Rev. D* 74 (12 Jan. 2021), p. 121503. DOI: 10.1103/PhysRevD.74.121503. arXiv: 2101.10252 [astro-ph.HE].

[176] Christopher Evans, Pablo Laguna, and Michael Eracleous. “Ultra-Close Encounters of Stars With Massive Black Holes: Tidal Disruption Events With Prompt Hyperaccretion”. In: *Astrophys. J. Lett.* 805.2 (12 2015), p. L19. DOI: 10.1088/2041-8205/805/2/L19. arXiv: 1502.05740 [astro-ph.GA].

[177] Karan Jani et al. “Georgia Tech Catalog of Gravitational Waveforms”. In: *Class. Quant. Grav.* 33.20 (12 2016), p. 204001. DOI: 10.1088/0264-9381/33/20/204001. arXiv: 1605.03204 [gr-qc].

[178] Horst R. Beyer and Olivier Sarbach. “On the well posedness of the Baumgarte-Shapiro-Shibata-Nakamura formulation of Einstein’s field equations”. In: *Phys. Rev. D* 70 (12 2004), p. 104004. DOI: 10.1103/PhysRevD.70.104004. arXiv: gr-qc/0406003.

[179] Luca Baiotti et al. “Three-dimensional relativistic simulations of rotating neutron star collapse to a Kerr black hole”. In: *Phys. Rev. D* 71 (12 2005), p. 024035. DOI: 10.1103/PhysRevD.71.024035. arXiv: gr-qc/0403029.

[180] Ian Hawke, Frank Loffler, and Andrea Nerozzi. “Excision methods for high resolution shock capturing schemes applied to general relativistic hydrodynamics”. In: *Phys. Rev. D* 71 (12 2005), p. 104006. DOI: 10.1103/PhysRevD.71.104006. arXiv: gr-qc/0501054.

[181] M. A. Aloy et al. "GENESIS: A High-Resolution Code for Three-dimensional Relativistic Hydrodynamics". In: 122.1 (12 May 1999), pp. 151–166. DOI: 10.1086/313214. arXiv: astro-ph/9903352 [astro-ph].

[182] P. Colella and Paul R. Woodward. "The Piecewise Parabolic Method (PPM) for Gas-Dynamical Simulations". In: *Journal of Computational Physics* 54 (12 Sept. 1984), pp. 174–201. DOI: 10.1016/0021-9991(84)90143-8.

[183] Erik Schnetter, Scott Hawley, and Ian Hawke. *Carpet: Adaptive Mesh Refinement for the Cactus Framework*. Nov. 2016. DOI: 10.1103/PhysRevD.74.121503. ascl: 1611.016.

[184] Ian Hinder et al. "Error-analysis and comparison to analytical models of numerical waveforms produced by the NRAR Collaboration". In: *Class. Quant. Grav.* 31 (12 2014), p. 025012. DOI: 10.1088/0264-9381/31/2/025012. arXiv: 1307.5307 [gr-qc].

[185] Horng Sheng Chia. "Tidal Deformation and Dissipation of Rotating Black Holes". In: *Phys. Rev. D* 74 (12 Oct. 2020), p. 121503. DOI: 10.1103/PhysRevD.74.121503. arXiv: 2010.07300 [gr-qc].

[186] Quentin Henry, Guillaume Faye, and Luc Blanchet. "Tidal effects in the equations of motion of compact binary systems to next-to-next-to-leading post-Newtonian order". In: *Phys. Rev. D* 101.6 (12 2020), p. 064047. DOI: 10.1103/PhysRevD.101.064047. arXiv: 1912.01920 [gr-qc].

[187] Emanuele Berti, Vitor Cardoso, and Clifford M. Will. "On gravitational-wave spectroscopy of massive black holes with the space interferometer LISA". In: *Phys. Rev. D* 73 (12 2006), p. 064030. DOI: 10.1103/PhysRevD.73.064030. arXiv: gr-qc/0512160.

[188] C.M. Biwer et al. "PyCBC Inference: A Python-based parameter estimation toolkit for compact binary coalescence signals". In: *Publ. Astron. Soc. Pac.* 131.996 (12 2019), p. 024503. DOI: 10.1088/1538-3873/aaef0b. arXiv: 1807.10312 [astro-ph.IM].

[189] Benjamin J. Owen and B.S. Sathyaprakash. "Matched filtering of gravitational waves from inspiraling compact binaries: Computational cost and template placement". In: *Phys. Rev. D* 60 (12 1999), p. 022002. DOI: 10.1103/PhysRevD.60.022002. arXiv: gr-qc/9808076.

[190] James Healy et al. "Post-Newtonian Quasicircular Initial Orbits for Numerical Relativity". In: *Class. Quant. Grav.* 34.14 (12 2017), p. 145011. DOI: 10.1088/1361-6382/aa7929. arXiv: 1702.00872 [gr-qc].

[191] Tim Dietrich et al. "High-resolution numerical relativity simulations of spinning binary neutron star mergers". In: *26th Euromicro International Conference on Parallel, Distributed and Network-based Processing*. Vol. 74. American Physical Society, Mar. 2018, p. 121503. DOI: 10.1109/PDP2018.2018.00113. arXiv: 1803.07965 [gr-qc].

[192] Milton Ruiz et al. "Black hole-neutron star coalescence: effects of the neutron star spin on jet launching and dynamical ejecta mass". In: *Phys. Rev. D* 102.12 (12 2020), p. 124077. DOI: 10.1103/PhysRevD.102.124077. arXiv: 2011.08863 [astro-ph.HE].

[193] Michael Boyle. "Transformations of asymptotic gravitational-wave data". In: *Phys. Rev. D* 93.8 (12 2016), p. 084031. DOI: 10.1103/PhysRevD.93.084031. arXiv: 1509.00862 [gr-qc].

[194] Charles J. Woodford, Michael Boyle, and Harald P. Pfeiffer. "Compact Binary Waveform Center-of-Mass Corrections". In: *Phys. Rev. D* 100.12 (12 2019), p. 124010. DOI: 10.1103/PhysRevD.100.124010. arXiv: 1904.04842 [gr-qc].

[195] T. W. Baumgarte and S. L. Shapiro. *Numerical Relativity: Solving Einstein's Equations on the Computer*. Vol. 74. Cambridge University Press, 2010, p. 121503. DOI: 10.1103/PhysRevD.74.121503.

[196] L. L. Smarr, ed. *Sources of gravitational radiation; Proceedings of the Workshop, Seattle, Wash., July 24-August 4, 1978*. Vol. 74. American Physical Society, 1979, p. 121503. DOI: 10.1103/PhysRevD.74.121503.

[197] Saul A. Teukolsky. "The Kerr Metric". In: *Class. Quant. Grav.* 32.12 (12 2015), p. 124006. DOI: 10.1088/0264-9381/32/12/124006. arXiv: 1410.2130 [gr-qc].

[198] Francois Foucart. "Black Hole-Neutron Star Mergers: Disk Mass Predictions". In: *Phys. Rev. D* 86 (12 2012), p. 124007. DOI: 10.1103/PhysRevD.86.124007. arXiv: 1207.6304 [astro-ph.HE].

[199] Gregory B. Cook and James W. York Jr. "Apparent Horizons for Boosted or Spinning Black Holes". In: *Phys. Rev. D* 41 (12 1990), p. 1077. DOI: 10.1103/PhysRevD.41.1077.

[200] Sergio Dain, Carlos O. Lousto, and Ryoji Takahashi. "New conformally flat initial data for spinning black holes". In: *Phys. Rev. D* 65 (12 2002), p. 104038. DOI: 10.1103/PhysRevD.65.104038. arXiv: gr-qc/0201062.

[201] Pedro Marronetti and Richard A. Matzner. "Solving the initial value problem of two black holes". In: *Phys. Rev. Lett.* 85 (12 2000), pp. 5500–5503. DOI: 10.1103/PhysRevLett.85.5500. arXiv: gr-qc/0009044.

[202] Ian Ruchlin et al. "Puncture Initial Data for Black-Hole Binaries with High Spins and High Boosts". In: *Phys. Rev. D* 95.2 (12 2017), p. 024033. DOI: 10.1103/PhysRevD.95.024033. arXiv: 1410.8607 [gr-qc].

[203] Bernard J. Kelly and John G. Baker. "Decoding mode mixing in black-hole merger ringdown". In: *Phys. Rev. D* 87.8 (12 2013), p. 084004. DOI: 10.1103/PhysRevD.87.084004. arXiv: 1212.5553 [gr-qc].

[204] Koutarou Kyutoku et al. "Reducing orbital eccentricity in initial data of black hole–neutron star binaries in the puncture framework". In: *Phys. Rev. D* 103.2 (12 2021), p. 023002. DOI: 10.1103/PhysRevD.103.023002. arXiv: 2009.03896 [gr-qc].

[205] Antoni Ramos-Buades, Sascha Husa, and Geraint Pratten. "Simple procedures to reduce eccentricity of binary black hole simulations". In: *Phys. Rev. D* 99.2 (12 2019), p. 023003. DOI: 10.1103/PhysRevD.99.023003. arXiv: 1810.00036 [gr-qc].

[206] Francois Foucart. "A brief overview of black hole-neutron star mergers". In: *Front. Astron. Space Sci.* 7 (12 2020), p. 46. DOI: 10.3389/fspas.2020.00046. arXiv: 2006.10570 [astro-ph.HE].

[207] William E. East, Vasileios Paschalidis, and Frans Pretorius. "Eccentric mergers of black holes with spinning neutron stars". In: *Astrophys. J. Lett.* 807.1 (12 2015), p. L3. DOI: 10.1088/2041-8205/807/1/L3. arXiv: 1503.07171 [astro-ph.HE].

[208] Enrico Barausse and Alessandra Buonanno. "An Improved effective-one-body Hamiltonian for spinning black-hole binaries". In: *Phys. Rev. D* 81 (12 2010), p. 084024. DOI: 10.1103/PhysRevD.81.084024. arXiv: 0912.3517 [gr-qc].

[209] Branson C. Stephens, William E. East, and Frans Pretorius. "Eccentric Black Hole-Neutron Star Mergers". In: *Astrophys. J. Lett.* 737 (12 2011), p. L5. DOI: 10.1088/2041-8205/737/1/L5. arXiv: 1105.3175 [astro-ph.HE].